

Development of a dust sensor for a satellite formation in low earth orbit

Master Thesis Work of
Mr. Francisco Mansilla

IRS-18-S-115

Supervisors:

Jona Petri

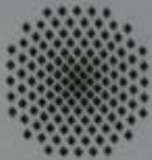
Heiko Strack

Responsible Professor:

Sabine Klinkner

Institut für Raumfahrtssysteme, Universität Stuttgart

December 2018



Master Thesis Work
of Mr. Francisco Mansilla
German thesis title

Development of a dust sensor for a satellite formation in low earth orbit

Motivation:

Together with the TU Berlin, the IRS is planning a mission to detect dust from an low earth orbit and to determine meteor trajectories. Two satellites are necessary to obtain a trajectory of a meteor observed simultaneously by two cameras. Therefore, this mission consist of two satellites flying in a formation. The TU Berlin develops the satellite bus, while the IRS is responsible for the development of the payload. This includes the dust sensor, a camera system for meteor detection and a visual camera for public outreach. Furthermore, the IRS develops the payload on board computer to control the payload and store the data. Another part of the IRS is the downlink of the payload data using the X-Band.

For all payloads several constraints have to be met, this includes constraints of the satellite bus (available space and power, thermal constraints) as well as scientific requirements (e.g. the ability to detect a certain particle size or detect meteors with a low magnitude).

The task of this thesis is to develop a mechanical design for the dust sensor, taking into account the manufacturing process as well as the loads occurring during launch and in the space environment.

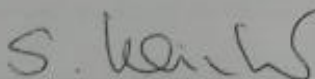
Task description of the Master thesis work:

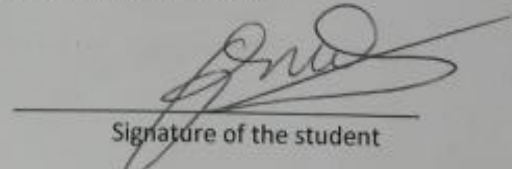
- Literature research and Introduction to dust sensors
- Identification of the scientific and technical requirements for the dust sensor
- Development of a CAD model
- Test and verification of the model with FEM analyses
- Manufacturing of a dust sensor model
- Documentation

Supervisor: Jona Petri
Starting date: 18.06.2018
Submission until: 18.12.2018

Acknowledgement of receipt:

I hereby confirm that I read and understood the task of the master thesis, the juridical regulations as well as the study- and exam regulations.


Prof. Dr.-Ing. Sabine Klinkner
(Responsible Professor)


Signature of the student

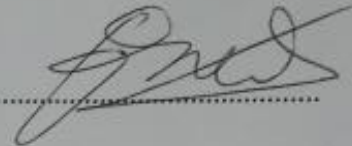
Declaration

I, **Francisco, Mansilla Navarro** hereby certify that I have written this **Master Thesis** independently with the support of the supervisor, and I did not use any resources apart from those specified. The thesis, or substantial components of it, has not been submitted as part of graded course work at this or any other educational institution.

I also declare that during the preparation of this thesis I have followed the appropriate regulations regarding copyright for the use of external content, according to the rules of good scientific and academic practice¹. I have included unambiguous references for any external content (such as images, drawings, text passages etc.), and in cases for which approval is required for the use of this material, I have obtained the approval of the owner for the use of this content in my thesis. I am aware that I am responsible in the case of conscious negligence of these responsibilities.

Stuttgart, 19/12/2018

Place, Date, Signature



I hereby agree that my **Master thesis** with the following title:

Development of a Dust sensor for a satellite formation in low earth orbit

is archived and publicly available in the library of the Institute of Space Systems of the University of Stuttgart **without blocking period** and that the thesis is available on the website of the institute as well as in the online catalogue of the library of the University of Stuttgart. The latter means that bibliographic data of the thesis (title, author, year of publication, etc.) is permanently and worldwide available.

After finishing the work I will, for this purpose, deliver a further copy of the thesis along with the examination copy, as well as a digital version.

I transfer the proprietary of these additional copies to the University of Stuttgart. I concede that the thesis and the results generated within the scope of this work can be used free of cost and of temporal and geographical restrictions for the purpose of research and teaching to the institute of Space Systems. If there exist utilization right agreements related to the thesis from the institute or third parties, then these agreements also apply for the results developed in the scope of this thesis.

Stuttgart, 19/12/2018

Place, Date, Signature



¹ Stated in the DFG recommendations for „Assurance of Good Scientific Practice“ or in the statute of the University of Stuttgart for „Ensuring the Integrity of Scientific Practice and the Handling of Misconduct in Science“

Acknowledgments

First of all, I would like to show my gratitude to the coordinators of this project, Jona Petri and Heiko Strack, for their effort and patience during the last 6 months. Thanks to them, I could progress in the understanding and development of the sensor and delve into the study of such an interesting field.

Besides, I want to thank Jan for his great help in terms of the CAD design, and the problems that I have encountered with the CATIA software, that he helped to solve.

Finally, to all my friends and family, for their support, encouragement and company during all this years, special mention to Pablo, Oliver, Alex, Julia, Andrea and Blanca.

To all that are not here anymore...

Introduction

The following Master Thesis is focused on the study and development of a dust sensor and the accomplishment of the different requirements but also regarding the limitations of the FACIS mission. The main limiting factor is the size of the sensor, which should not exceed the space left for its assembly in previous conceptual designs of the satellite. The size of the sensor was thought to be around $10 \times 10 \times 10 \text{cm}^3$. One of the challenges to face during the development of the sensor will be to find suitable components that can be produced with a good cost to performance ratio. As a second step, the structural design will be focused in a modular laboratory model to have the possibility of testing different components to validate the conceptual design.

On the first hand, the study will be focused on the understanding of the operation of a dust sensor, acquiring knowledge based on other prototypes, so as to set the starting point of the project. Also it will be important to take into account issues such: the use of different materials, the interaction between them, the small available space inside the satellite... but also bearing in mind further limitations that cannot be forgotten, such as sensitivity, wiring or manufacture possibilities. Besides, the conceptual study developed by Dr. Srama will be taken into account.

On the other hand, it is crucial to minimize the costs of the production while comparing different designs and deciding whether to buy or to manufacture certain components given the quotation of different companies. One of the main goals of this Thesis is to achieve a solution to include all the required components by minimizing costs, but at the same time respecting the limitations.

Therefore some studies are made to estimate important parameters such as the field of view of the sensor, the production of some components or the mass resolution optimization. With the combination of the CAD files and all these studies, it will be much easier to compute next design iterations, to do all the experimental analysis.

Finally, future lines of investigation will be proposed to assure an accurate final design.

List of Figures

1.1	CAD distribution of main components of the satellite	10
1.2	Cosmic Dust Size	11
1.3	Atmosphere layers with altitude	12
1.4	Growht of satellites launched to LEO within the last 50 years	13
1.5	Size particles regarding their origin	13
2.1	Signal obtained by a Dust Analyzer. The chemical composition is obtained from the study of the signal.	18
2.2	Schematic Distribution of the payloads in FACIS Satellite.	19
2.3	Grid Configuration in Cassini Dust Analyzer	21
2.4	CDA appearance	21
3.1	Section View of the appearance of the Dust Sensor and its components	24
3.2	Grid Geometry and details of the grid's dimensions	26
3.3	Grid Geometry and details of the acceleration grid	26
3.4	Frame CAD design	28
3.5	On the left a milling tool with the usable length and Diameter of operation. On the right the CAD design for the PVC component.	29
3.6	On the left first configuration. On the middle workshop suggestion. On the righth final L section alluminium supports to be attached to the housing.	30
3.7	On the left and middle, first housing designs. On the right, final laminates conforming the housing.	31
3.8	Time of Flight of an ion to the ion detector depending on the drift area distance $s = 3mm$	32
3.9	Δt between two ions of a $\Delta m/z = 1$	32
3.10	Housing before the changes were made	34
3.11	Final Cylindrical Housing	34
3.12	Components of the cylindrical structure	35
3.13	Model of the applied force in a piezoelectric sensor and analog circuit	37
3.14	Transfer function of the output voltage of the sensor	38
3.15	Piezo disc configurations and CAD design with its housing	39
3.16	Assembly of the frames and attachments	41
3.17	Assembly of the Ion Detector and Sticks	42
3.18	Side View of the housing. The black hole resembles the place where to stick the alluminium element to the initial configuration.	42
3.19	Assembly of the Modular Components	43
3.20	Final Assembly of the sensor and rendered model	44
3.21	Configurations to be made on the laboratory for testing the components	45
3.22	Limitation elements required for the study of the tilted angle.	46
3.23	Particles going through the sensor with angles of incidence	47

4.1	Top View of the incoming particles with a certain α	48
4.2	Detail of the distance x_2	48
4.3	Angles obtained from geometry	49
4.4	Front View of a particle with 0° incidence.	50
4.5	Front View of a particle with an angle of incidence lower than α_1°	51
4.6	Front View of a particle with an angle of incidence equal to α_4°	51
4.7	Calculation of the distance x_3 depending on the angle of incidence.	52
4.8	Example of the probability of detection for different angles of incidence in one plane.	52
4.9	Superposition of angles of incidence that results into a shadow in the plate . . .	53
4.10	Activation of counters depending on the angles of incidence	54
4.11	Visualization of the Field of View of R8811 Hamamatsu Electron Multiplier and 2D Representation	55
4.12	Visualization of the Field of View of Disc Micro Channel Plate and 2D representation	55
4.13	Visualization of the Field of View of two ion detectors. On the left, the R8811 electromultiplier from Hamamatsu. On the right, a circular MCP from Hamamatsu.	56
5.1	Force applied on the piezo sensor. Charge induced and output voltage.	58
5.2	Sensitivity depending on the piezoelectric voltage coefficient. On the left $g_{33} = 53 \cdot 10^{-3}Vm/N$. On the right $g_{33} = 25 \cdot 10^{-3}Vm/N$	58
	59figure.caption.56	
5.4	Sensitivity depending on the density of the particles. On the left $\rho = 3g/cm^3$. On the right $\rho = 8g/cm^3$	60
5.5	Mass and Velocity tresholds to be measured by the sensor.	61
8.1	Future Possible iteration of the CAD design	69

List of Tables

- 1.1 Requirements for Orbital Analysis 10
- 1.2 Results from Orbital Analysis 10
- 1.3 Impact Probability extracted from NASA 2.0 Software 15

- 2.1 The table summarizes parameters for different dust sensors which have been described 21

- 6.1 Table of prices and weight of the components of the project. 63
- 6.2 Potential Ion detectors and characteristics(1). 63
- 6.3 Potential Ion detectors and characteristics(1). 64

Contents

Acknowledgments	2
Introduction	3
1 FACIS Mission and Environment	9
1.1 FACIS Mission	9
1.2 Overview of cosmic dust	11
1.3 Low Earth Orbit	12
1.4 Possibilities of dust detection	14
2 Dust Sensor Definition and Examples	16
2.1 Introduction to dust sensors	16
2.1.1 Dust Trajectory Sensor	17
2.1.2 Dust Analyzer	17
2.2 Main components of FACIS dust sensor	18
2.3 Examples of Dust Sensors	20
2.3.1 Dust Impact Sensor in Pioneer 8	20
2.3.2 ESPART	20
2.3.3 Dust Impact Detection System in Giotto Mission	20
2.3.4 Dust Impact Sensor in Armadillo	20
2.3.5 Stardust Cometary and Interstellar Dust Analyzer (CIDA)	20
2.3.6 Cassini Cosmic Dust Analyzer (CDA)	21
2.3.7 NASA Space Debris Sensor	21
3 CAD Design of the dust sensor	22
3.1 Overview of the FACIS Dust Sensor	23
3.2 Main Components of the design	24
3.2.1 Charge Sensitive Grids	24
3.2.2 Frames of Grids	28
3.2.3 PVC Attachments	28
3.2.4 Support Modular Alluminium Structures	29
3.2.5 Housing Structure for the trajectory sensor area	31
3.2.6 Ion detector	31
3.2.7 Housing of cylindrical part of the sensor	34
3.2.8 Modular alluminium attachment	34
3.2.9 Frames for Acceleration Grid	34
3.2.10 Insulators for the acceleration grid	34
3.2.11 Target Plate and Piezo Sensor	36
3.3 Assembly of the Dust Sensor	41
3.3.1 Changes on assembly: Tilting Grids and Increase Separation	45

3.3.2	Calculation of Velocity and Trajectory of the Particles	46
4	Field of View	48
4.1	Field of View in 3D	53
5	Study of Sensitivity	57
5.1	Sensitivity vs Material Properties	58
5.2	Sensitivity vs Sensor Size	59
5.3	Sensitivity vs Density of Particles	59
5.4	Superposition of Signals	60
6	Total Costs and Selection Criteria	62
7	Conclusions	66
8	Future Lines of Investigation	68
	Bibliography	70
	Appendix A CAD Plans	1
	Appendix B R8811 Specifications	1
	Appendix C PIEZO PROPERTIES	1

1

FACIS Mission and Environment

As an introduction of the behaviour of the satellite in orbit, the tasks that the satellite will carry out during the whole mission are determined. In this chapter will also be explained the environment characteristics in space such as the particles encountered in orbit, the main parameters of the orbit of the satellite, as well as the requirements to be fulfilled, for example the loading that the satellite will undergo during launching. Setting the main characteristics and requirements of the mission is one of the crucial points of the design of the satellite. Knowing the environment in which the satellite will be deployed will help with the decision making, as well with the choice of materials and components.

1.1 FACIS Mission

Formation for Analysis of Cosmic partIcleS

The main aim of the project is the preliminary study of a two microsatellite formation mission for the determination of meteoroid trajectories and dust mass flow measurement. The project is planned as a cooperation between the Institute of Aeronautics and Astronautics (ILR) at the Technische Universitat Berlin and the Institute of Space Systems (IRS) at the University of Stuttgart.¹ There are three payloads designated for the FACIS mission. These payloads are a wide-angle camera for meteoroid trajectory determination, a dust detector measuring dust mass flow and a VIS camera for taking pictures of the Earth's surface and the respective partner satellite.

Both spacecrafts are based on the modular TUBiX20 platform, which was developed by ILR. Each satellite has a mass of approximately 30 kg and carries two scientific payloads. One is a camera designed for the observation of atmospheric meteors². Here, the use of two spacecraft enables stereoscopic observation and thus the determination of the associated meteoroids' trajectories.

¹Phase A study performed by F.Hufgard

²Developed by the IRS

The second payload, which will be developed by IRS, is an in-situ detector for dust particles and micro-meteoroids. It will provide data on the dust particles in the satellites' orbit.

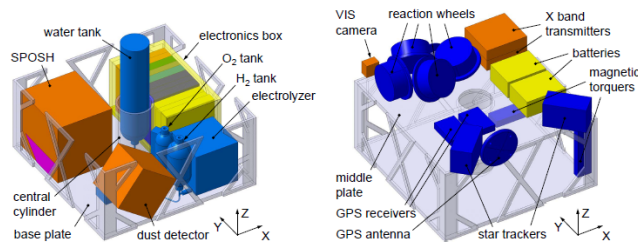


Figure 1.1: CAD distribution of main components of the satellite

The orbital lifetime is limited by the minimal mission duration and the maximal duration until re-entry (after end of life) driven by the European Code of Conduct for Space Debris Mitigation. A Sun synchronous orbit with a Local Time of Descending Node (LTDN) of 9:00-15:00 is chosen due to its similar orbit conditions over the lifetime, its high eclipse times for meteor observation and good launch opportunity availability. The orbital analysis was conducted in a previous project with the software STK of Analytical Graphics, Inc. In the following table we show the main requirements of the orbital analysis.

Table 1.1: Requirements for Orbital Analysis

Requirements for Orbital Analysis	
Minimal Mission Duration	2 years
Maximal duration (Re-entry)	25 years
Local Time Descending Node	9:00 - 15:00
Orbit	Sun Synchronous, Circular

The main goal of the orbital analysis was to determine the orbit range into which the satellites can be launched. Also, the maximal eclipse time for dimensioning the electrical power system was to be computed, which was the case for a 300 km at LTDN 12:00 orbit. Finally, an elevation of the satellite over the horizon of at least 7° (telemetry and telecommand) and 10° (payload data downlink) was assumed for the simulation of the minimal and maximal contact times to the ground station of the communication system. The following table shows the results of the orbital analysis.

Table 1.2: Results from Orbital Analysis

Results Orbital Analysis	
Launch Orbit Range	435 - 565 km
Operational Orbit Range	300 - 565 km
Operational Orbit Periods	5431 - 5758 s
Maximal Eclipse duration	2183 s
Daily telemetry and telecommand	797 - 2232 s
Dayli payload data downlink	666 - 1566 s

1.2 Overview of cosmic dust

Scattered throughout the observable universe is a great diversity of microscopic particles, known collectively as cosmic dust. Cosmic dust is responsible for such phenomena as zodiacal light, comet tails, extinction of light from distant stars, the transfer of heavy elements from supernovae to emerging star systems, and some others. Cosmic dust grains fall into two classifications: interstellar dust and interplanetary dust. [26]

Interstellar dust is generally defined as particulate matter that originates outside of the solar system. Interstellar dust grains are created during a variety of stellar phenomena including supernovae, red giants, and carbon-rich stars. The chemical and isotopic properties of dust grains provide important information about the processes taking place in the environments in which the grains were formed. Because the material making up the Earth and other planets was, at one time, interstellar dust, the chemical and isotopic properties of dust grains provide information about planetary formation processes. Interstellar dust may make up the difference between the observed abundances of elements heavier than helium in the interstellar gas and the assumed cosmic abundances of the elements.

Interstellar dust flows through the solar system with a speed up to 26 km/s. Because cosmic dust grains are electrically charged by photoelectron emission, grains smaller than about $0.1 \mu\text{m}$ are deflected by the sun's magnetic field, and do not frequently penetrate the solar system. In fact, about 30% of the micron-sized dust reaching the Earth is of interstellar origin.

Interplanetary dust is defined as particulate matter originating within the solar system. This includes cometary debris, planetary rings, man-made debris (frequently encountered in Earth orbit), particles created during asteroid and meteor impacts, and various other local sources. Particles in the size range of $10\text{-}100 \mu\text{m}$ account for most of the light scattering in the zodiac. Most interplanetary dust grains eventually assume quasi-stable orbits around the sun, although radiation pressure, charge and magnetic interactions, and gravitational resonances all complicate their trajectories and lifetimes.

The dynamics, distributions, and possible sources of various dust populations within the solar system have been extensively studied. The elemental composition of most solar system dust grains is approximately chondritic, although some may have disproportionate contributions from specific minerals such as magnesium silicates, iron-nickel metal, sulfides, phosphides, or carbonates.

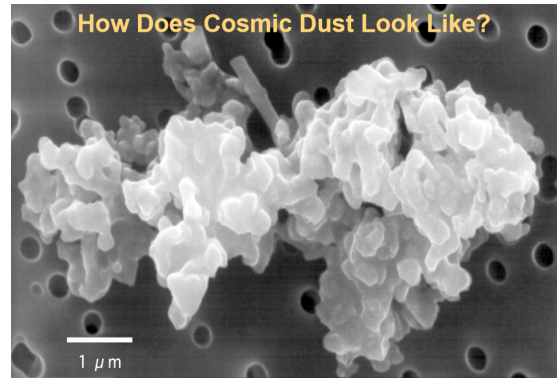


Figure 1.2: Cosmic Dust Size

1.3 Low Earth Orbit

Beginning in the 1950s with the Sputnik, Vostok and Mercury programs, human beings began to "slip the surly bonds of Earth". And for a time, all of our missions were what is known as Low-Earth Orbit (LEO). Over time, with the Apollo missions and deep space missions involving robotic spacecraft (like the Voyager missions), we began to venture beyond, reaching the Moon and other planets of the Solar System.

But by and large, the vast majority of missions to space over the years – be they crewed or uncrewed – have been to Low-Earth Orbit. It is here that the Earth's vast array of communications, navigation and military satellites reside. And it is here that the International Space Station (ISS) conducts its operations, which is also where the majority of crewed missions today go. Technically, objects in low-Earth orbit are at an altitude of between 160 to 2000 km above the Earth's surface.

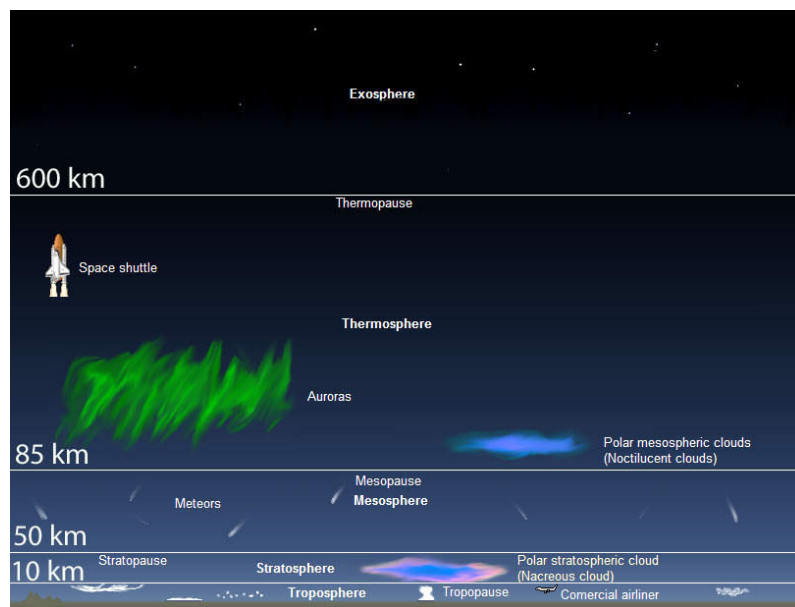


Figure 1.3: Atmosphere layers with altitude

Given the range of the mission, the study of the thermosphere is the one of main interest. Temperatures in the thermosphere can rise as high as $1500\text{ }^{\circ}\text{C}$ ($2700\text{ }^{\circ}\text{F}$), the spacing of the gas molecules means that it would not feel hot to a human who was in direct contact with the air. At altitudes between 160 and 1000 km from the Earth's surface, objects are not subject to the intense radiation of the Van Allen Belts. In short, LEO is the simplest, cheapest and safest location for the deployment of satellites, space stations, and crewed space missions.

The existence of this debris field in LEO has led to growing concern in recent years, since collisions at high-velocities can be catastrophic for space missions. And with every collision, additional debris is created, creating a destructive cycle known as the Kessler Effect. In 2013, NASA estimated that there may be more than more than 100 million smaller than 1 cm.

Depending on the orbital altitude and inclination the Meteoroid and Space debris Terrestrial

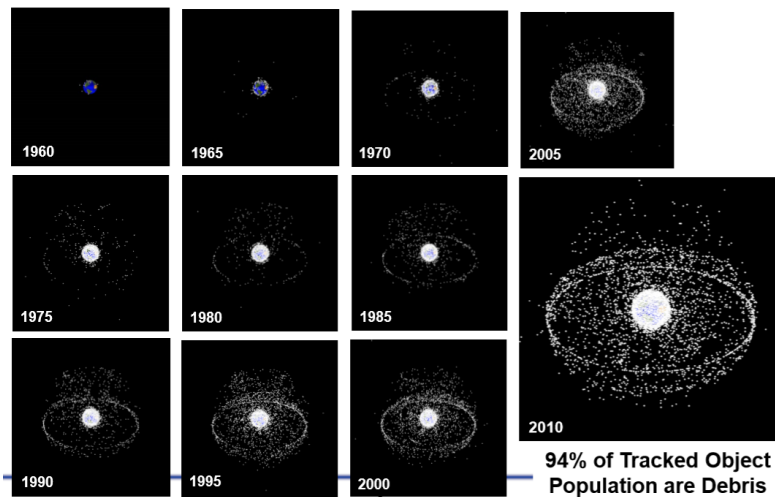


Figure 1.4: Growth of satellites launched to LEO within the last 50 years

Environment Reference model (MASTER 2005) shows that the number of impacts in Low Earth orbit (LEO) ranges from 5000-9000 per m^2 per year. The number of impacts on a satellite or spacecraft can easily exceed the thousands. According to the MASTER 2005 model, the mass of the majority of the particles in Earth orbit are in the range of 1 - 10 μm .

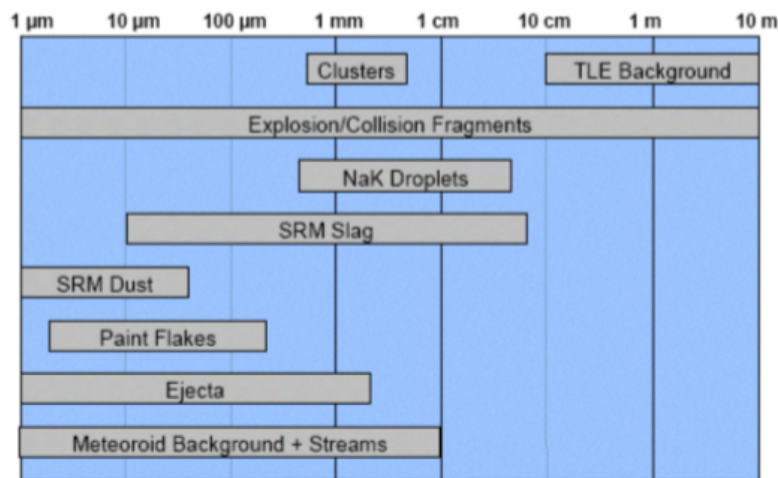


Figure 1.5: Size particles regarding their origin

Objects that are in Low Earth Orbit may then have velocities on the order of 20km/s. At such speeds, impact with a particle even 1 cm or smaller in diameter could seriously damage a satellite. Smaller objects may not threaten the structural integrity of the satellite, but could easily damage valuable equipment, such as camera lenses, that are on board. Thus, a mechanism is needed for the satellite to detect this debris and protect its sensitive equipment when the flux of these particles becomes too large.

1.4 Possibilities of dust detection

In order to obtain an estimation of the number of particles that the satellite will encounter during its mission and the characteristics of them, there is a wide range of options to measure as much as possible. In further chapters it will be explained how this possibility of detection becomes lower due to different limitations.

First of all, one of the main parameters of the sensor is the maximum sensitivity of measurement or in other words, what kind of particles will the sensor be able to measure regarding size, composition, velocity, trajectories, etc.

As an example, the ISS has an orbital velocity that ranges between 7 km/s and 8 km/s, depending on its current position in orbit. The assumption has been made that FACIS satellite will have approximately the same velocity when it is in orbit. This provides an estimate for the maximum impact velocity that the sensor could experience. NASA states that the average impact velocity of debris with the ISS is 10 km/s. So the relative velocity at which the particle will hit the satellite will not go further than 20 km/s. The orbital speed of FACIS satellite can be computed to obtain the accurate relative velocity of the incoming particles. The orbital altitude will be set between 300 and 600 km, therefore the possible velocities would be 7,73 km/s and 7,58 km/s respectively.³

The total kinetic energy of the debris particles, though, can not be calculated unless their masses are known. At the altitude of LEO, nearly all of the objects in orbit are man made. They were left behind by past satellites that either deposited unneeded equipment or simply desintegrated. Since satellites are designed to be lightweight, the most dense material that could likely be found in LEO is steel (approximately 8 g/cm³). [11]

There are also softwares that act as data bases of the space debris and are very useful to have an idea of the current amount of debris and their characteristics. They give as output values relevant information like the number of impacts in a certain orbit, regarding the size of the particles. The main softwares that have been analysed for this thesis are: *SPENVIS*, *ESA Debris Software*, *NASA DAS 2.0 Software*.⁴

In the presented thesis, the NASA DAS 2.1 Software has been used. The first reason is because it uses an easy interface, with a quick introduction of the input parameters. Another reason is because the ESA software only allows to analyse orbits upper than the LEO, and that study is not of our concern.

NASA's DAS 2.0.2 software, provides information about space debris and meteoroids based at various orbital altitudes. The input information required are the orbital parameters as well as the duration of the FACIS mission, and the dimensions of the satellite. With the calculation of the inclination⁵ of the satellite for both altitudes and introducing the average value (97 deg), and setting a value for the RAN of 12 deg⁶ the simulation can be launched. Simulating with this values, the calculation of the rate of collisions depending on the particle sizes are summarized

³ $v^2 = \frac{\mu}{r_k} \rightarrow \mu = 3.986 \cdot 10^{14} \frac{m^3}{s^2}$

⁴All of them are for free use under request.

⁵ $Cos(i) = -(\frac{R_E + H}{12352})$

⁶From the Thesis of Fabian

in the following table. ⁷

Table 1.3: Impact Probability extracted from NASA 2.0 Software

Particle Diameter (m)	Impacts per year	Impacts per day
10^{-3}	0.000381	1.04 E-06
10^{-4}	0.156	4.27 E-04
10^{-5}	13.21	3.62 E-02
10^{-6}	50.67	1.39 E-01
10^{-7}	996.7	2.73
10^{-8}	278563	763.18

As it can be seen, the number of particles to be measured is too small, therefore the sensitivity of the sensor needs to be as high as possible, and its design optimized to assure the maximum number of measurements during the two years mission.

Different dust sensors have been analysed to be used as a guide to create a first approximation to the final design.

⁷The results show the particles that will encounter the satellite, but the dust sensor even less.

2

Dust Sensor Definition and Examples

In this chapter, the operation of a dust sensor is described as well as the main components that includes. Some examples of different prototypes used in sounded missions since 1967 in the space segment will be mentioned. Besides, the main components required to fulfill the objective of the FACIS mission will be also described. The analysis of each component will be made in further sections.

2.1 Introduction to dust sensors

Dust astronomy measures the composition, speed, trajectory, charge, and mass of cosmic dust particles. The particles are of micron and submicron size, contain millions of atoms, and carry a charge created mainly by plasmas and UV radiation. The particles are ejected from comets, asteroids, or moons; are fragments from mutual collisions; or originate from the solar systems environment or from stars. From the particles origins and their compositions, we learn the properties of their diverse birthplaces and their history. Dust astronomy in space uses normally a dust telescope containing one component or a combination of the following components to analyse these dust particles: dust trajectory sensor (DTS); an ion mass analyzer (LAMA), an active dust collector and an electrostatic particle mass analyzer.

The dust sensors can be separated in two main groups depending on the mission of the satellite:

- **Dust Collectors:** This kind of sensors are designed to measure the characteristics of the particles once the satellite has landed after the re-entry. Normally, they consist on a material collector that keeps the track of the incoming particles and are able to determine the composition and trajectory. In the last decades, the use of **Aerogel** [25] has become more popular. When hypervelocity particles are captured in aerogel they produce narrow cone-shaped tracks that are hollow, and can be seen in the highly transparent aerogel by using a stereomicroscope. This cone is largest at the point of entry, and the particle is held intact at the point of the cone. This provides a method for determining which direction the dust came from, and is the basis of the approach of using single slabs of aerogel to collect both cometary and interstellar dust from both sides.

- **In-situ sensors:** Many satellites utilize these sensors for missions that will not require the re-entry to Earth. The study and optimization of them have increased exponentially in order to achieve a wider range of measurements as well as more accurate results.

2.1.1 Dust Trajectory Sensor

The dust trajectory sensor(DTS) is an array of wires, or wired grids that sense charges induced by the charged particle as it moves through the DTS. It is a non-destructive sensor. Normally it has grounded shield grids at the entrance and exit of the DTS to prevent external fields from influencing the DTS and to shield from other charged particles, e.g. protons from the sun.

DTS employs wire arrays in series. A particle traveling between two wires induces charge pulses, depending on the distances to the wires, although nowadays the employment of solid grids is becoming more usual. The transit time between planes determines the velocity, and with the geometry of the grids, the angle of incidence of the particles can be measured as well. The sensor wires each connect to charge-sensitive amplifiers and a transient recorder. The transient recorder samples, digitizes, and buffers the signals over the maximum transit time.¹

Because the velocities of cosmic dust particles expected in the LEO vary from 1 to 20 km/s, the pulse widths of the induced charges vary by a decade, requiring wide-band amplifiers and producing excess noise at a given speed. The low speed particles exhibit excess high frequency noise and the high speed particles exhibit excess low frequency noise. It is very important to do a good filtering of the signals to obtain an accurate result. This filter provides a trigger signal for the readout of the transient recorder.

Logarithmic amplifiers are not fast enough and do not have sufficient dynamic range for the time of flight measurements.

2.1.2 Dust Analyzer

As an example, the dust analyzer from the Cassini mission is described here [2]. The DA measures the electric charge carried by dust particles, the impact direction, the impact speed, mass and chemical composition.

An electrically charged particle flying through the two inclined entrance grids at the front of the DA will induce charge signals on the grids. This induced charge is directly proportional to the charge of the particle and allows therefore a direct determination of its electric charge. The inclined grid geometry leads to asymmetric signal shapes allowing the measurement of the particle direction in one plane. The particle impacts a target which generates charged and uncharged fractures (ejecta), atoms and ions. The electrons of this plasma are collected by the target, and the positive ions are accelerated towards the ion detector by an electric field.

The chemical properties of the particles are analysed once they arrive the ion detector. The interpretation of the signal obtained in the ion detector will be possible by understanding the mass spectrometry theory, although it is not the main purpose of this master thesis.

To have a first approach to the mass spectrometry, the picture ?? shows the signal obtained by a dust analyzer and how the peak ratios of the signal as well as the separation between

¹The mathematical procedure to compute the velocities and trajectories is explained in 3.3.2

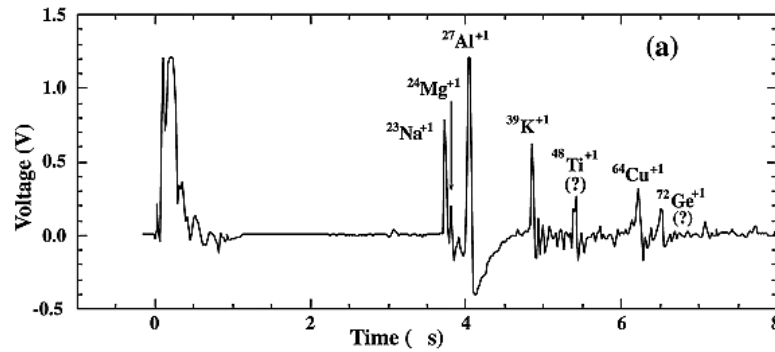


Figure 2.1: Signal obtained by a Dust Analyzer. The chemical composition is obtained from the study of the signal.

them lead to the determination of the chemical composition of the ionised particle. From other experiments, it was determined that the peak height for an element is difficult to relate to the abundance of that element in the material, due in large part to different ionization efficiencies of various elements. Not all the elements will show up in a spectrum. For example, nickel and iron are easy to ionize, as these have lower ionization potentials. Sulfur and oxygen are more difficult to find as both have high ionization potential and greater electron affinity. Atoms from these elements may form negative ions which are collected by the target plate along with the electrons. This implies that a single spectrum recorded by the CDA instrument is able to identify many of the elements like Fe, Ni, Ca, Al, Mg, Na, K but may not be able to detect S and silicate group elements Si and O.

One important point to take into consideration is the recording time of the signal, that normally is the time of flight of the heaviest ion. In case the CDA instrument is impacted by two (or more) dust particles in quick succession within ns², the recorded spectrum would be a superposition of two (or more) spectra. Care will be needed to interpret such spectra.

2.2 Main components of FACIS dust sensor

The conceptional design for the dust detector was developed by Ralf Srama. The design was adjusted to the limitations encountered during the integration of the components, but here an outlook of this initial conceptual design it is given. A dust particle, which is usually positively-charged, enters the dust detector on the front side. Beneath the opening, a shield grid is attached to prevent electrons and negatively charged ions with energies below 1 keV from entering the dust detector and thus reduce noise.

With respect to the detected particle's trajectory, there are three detection grids located behind the shield grid. The entering particle's field, which is caused by its positive charge, induces a negative charge onto the detection grids. This signal is amplified and transformed into a voltage by a charged sensitive amplifier to eventually yield the measurement signal. The signals resemble a triangle, where the respective moments of the peak voltages equal the moment the particle passes a detection grid.

²See study made in 3.2.6

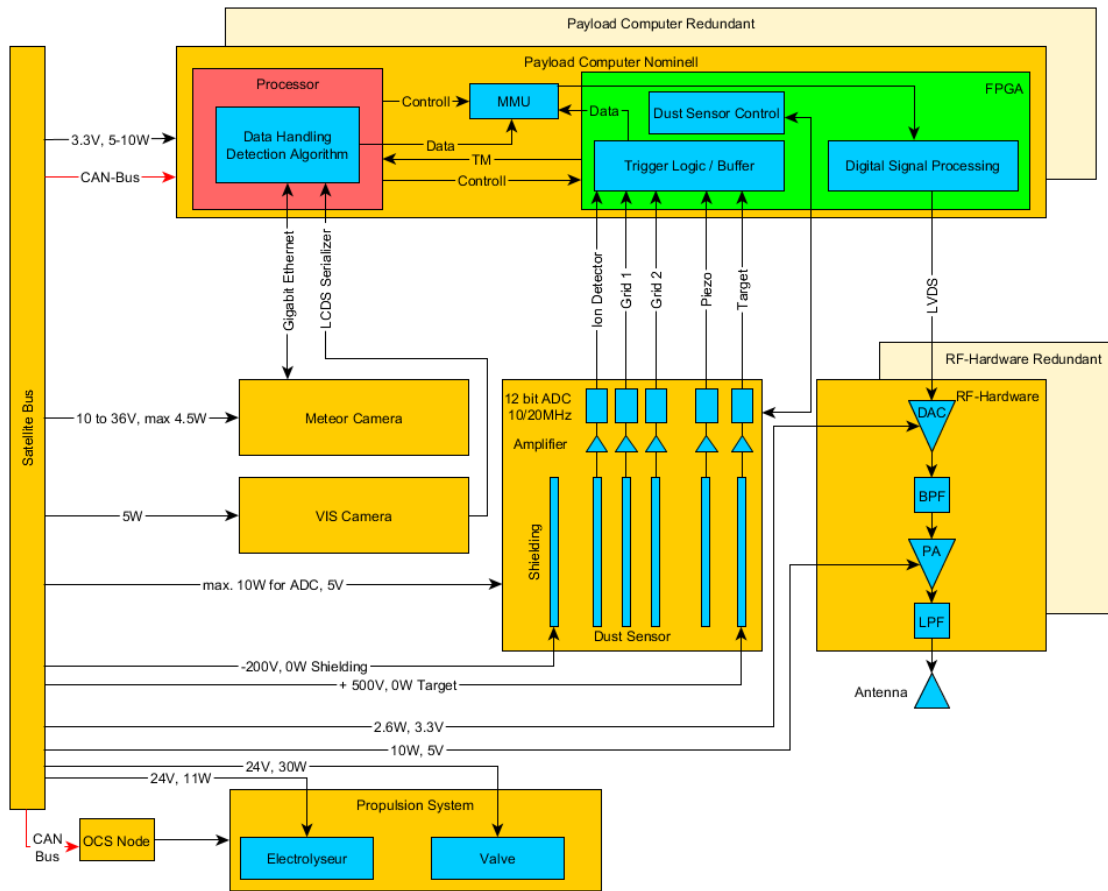


Figure 2.2: Schematic Distribution of the payloads in FACIS Satellite.

Given a known grid distance, the particle's velocity can be calculated from the delay of the individual peaks. Furthermore, the particle's mass can be determined from the signal's amplitude³, as there is a direct correlation between its mass and its charge. The signal shape also gives insight into the trajectory, although it can be determined tilting the grids. After passing the detection grids, the particle will ultimately impact into one of four Piezo detectors at the bottom side of the instrument. From the measurement signal, the particle mass, charge, velocity and trajectory can be determined, which allows for verification of the detection grid measurements. It was estimated by Srama that the instrument's mass will amount to 1 kg and it will measure $10 \times 10 \times 10 \text{ cm}^3$. The power consumption will come to 5 W and the instrument will produce 9 MB daily data when assuming one impact event per minute. The details of the components are shown in the chapter 5.4 as well as in the 8

$$^3 m = \frac{4\pi\rho}{3} \cdot \left(\frac{Q}{4\pi\epsilon_0\Phi}\right)^3.$$

2.3 Examples of Dust Sensors

During the last decades, the number of satellites sent into the LEO has increased considerably. Therefore, in this section will be studied some of the dust sensors already used in past missions. Dust sensors can be based on different operating principles depending on the parameters that have to be sensed. Sometimes the main goal of the sensor is to measure a single parameter like the mass of the particles, but sometimes there is a combination of components that will lead to the measurement of several characteristics of the incoming particles. Some examples of dust sensors are mentioned in the following.

2.3.1 Dust Impact Sensor in Pioneer 8

One of the seven experiments on board the Pioneer 8 satellite is a cosmic dust experiment, starting with a new generation of cosmic dust sensors, whose main objectives were: To measure the cosmic-dust flux density in the solar system, the distribution of cosmic dust concentrations (if any) in the earth's orbit, the radiant flux density and speed of particles in meteor streams, and to perform an in-flight control experiment on the reliability of the microphone as a cosmic dust sensor

2.3.2 ESPART

The ESPART dust sensor is made to analyse the size and mass of suspended dust particles under the influence of an oscillating electrostatic or acoustic field, which provokes the movement of the particle. Combining Stokes laws and LDV operating principles, the size of dust particles can be calculated.

2.3.3 Dust Impact Detection System in Giotto Mission

One of the first dust instruments using piezo based detectors was on board the Giotto spacecraft as part of the Dust Impact Detection System (DIDSY), designed to explore Halley's comet. One of the main scientific aim was to measure the mass distribution of the cometary dust efflux along the spacecraft trajectory.

2.3.4 Dust Impact Sensor in Armadillo

The detector has a mass of less than 500g and a size of about 80 mm - 80 mm - 40 mm which is less than half a cubesat unit. The signal which was used to detect an impact on one of the piezo sensor element depends on the velocity and the mass of the impacting particle. The size of detectable particles are in the range of 1 μm to 1 mm at a velocity of up to 10 km/s . The maximum measureable impact energy are approximately 1 J as impacts of higher energy probably destroy the piezo elements. The Piezo Dust Detector was selected as a potential payload for the ARMADILLO (Attitude Related Maneuvers And Debris Instrument in Low Orbit) mission.

2.3.5 Stardust Cometary and Interstellar Dust Analyzer (CIDA)

CIDA is a space qualified time-of-flight mass-spectrometer. Each impacting particle provides a TOF spectrum which can be transformed into a mass spectrum once at least two peaks are found to which well known mass numbers can be assigned. For CIDA a single stage ion reflector was chosen, followed by an open electron multiplier, also sensitive to ions, of 30 mm diameter sensitive surface area.

Table 2.1: The table summarizes parameters for different dust sensors which have been described

Mission	Efficient Area (cm ²)	Mass Resolution (Deltam/m)	Weight (Kg)	Power(W)
CIDA	110	250	50	
DIDSY	5	100	-	-
ARMADILLO	0.256	3.277 mJ	-	3
LAMA	1000	>120	40-70	1.28
CASSINI	100	20-50	16.36	15

2.3.6 Cassini Cosmic Dust Analyzer (CDA)

The Cassini mission, an international cooperation venture, was launched in October 1997. One of the objectives of this mission was to characterize the dust particles at the planet Saturn, within and between the rings, and surrounding its icy satellites. For this purpose the Cassini spacecraft was equipped with a Cosmic Dust Analyzer (CDA). The CDA was expected to make in situ measurements of the charge (10^{-15} to $10^{6.0112}C$), the impact speeds, the mass and composition of these dust particles. The micrometeoroid mass measurement range is $10^{6.0116}$ to $10^{6.016}g$ and the speed measurement range is 1 to 100 km/s. The charge on the particles is measured upon their passage through the two inclined grids at the entrance of the sensor housing. An integrated time of flight impact ionization mass spectrometer (Chemical Analyzer) provides constraints on the particle chemical composition. Particles impacting onto the Rhodium target plate of this instrument and some mass of the target itself get vaporized and partially ionized. The positive ions, mostly singly charged, are accelerated and then collected upon traveling some 25 cm in a CDA. The time of arrival of ions provide mass spectra for each dust particle.

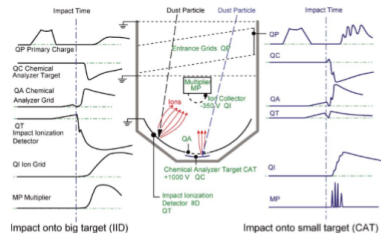


Figure 2.3: Grid Configuration in Cassini Dust Analyzer



Figure 2.4: CDA appearance

2.3.7 NASA Space Debris Sensor

The Space Debris Sensor SDS is a flight demonstration of a novel impact sensor designed to detect and characterize impacts of small debris objects on the International Space Station. It is the first flight demonstration of the Debris Resistive/Acoustic Grid Orbital NASA-Navy Sensor (DRAGONS) developed by the NASA Orbital Debris Program Office.

The system of the Cassini mission has been taken as an example of how the FACIS dust sensor could look like, as it is possible to measure the velocity, trajectory and chemical properties of the particles. The following table sammels the described sensors.

3

CAD Design of the dust sensor

The main objective of the thesis was to achieve a CAD structure that respected the strict size limitations, approaching the solution as much as possible to a final design. To reach a suitable one, there are some factors that were taken into account and form the basis of the decision making, which are explained in the following paragraphs. The design is an iterative process trying to combine all this factors and facing the challenges and problems during the procedure.

1. Particle Sensitivity Range

- **Particle Velocity:** Given the specifications of the FACIS mission, the velocity threshold to be measured is $1 - 20\text{km/s}$. The speed at which the particle goes through the sensor will set the requirements for the electronic components to be able to measure them, such as the time resolution. It will play an important role in the piezo target, to determine the characteristics and material properties for this component.
 - **Particle Size:** As well as the velocity, the size of the particle is crucial for the correct choice/design of a piezo sensor. The mass it is proportional to the induced charge on the grids, which will be a key value to obtain the trajectory of the particle.
2. **Materials:** The right choice of materials will be a key factor in order to minimize weight, and to assure an accurate behaviour of the different components. The isolation of some parts will be necessary and non-conductive materials will be needed into the design.
 3. **Size Limitations:** Probably the most restrictive factor to be fulfilled. Continuous changes are required in this field as a matter of the small size of the whole satellite and its configuration. As a matter of this limitation, the options for the rest of the components are considerably reduced to assure a sufficient field of view, avoiding obstacles on the free path of particles.
 4. **Production:** Even assuring a proper performance of the sensor, it is vital to bare in mind the difficulties that the components could face during their production. Directly connected to the costs, really complex configurations will rise the costs of production considerably. On first place, it is expected that the production will be done in the Workshop of the IRS,

reducing the costs to the price of the material plates. However, different techniques will be required for some components to be produced by other companies.

5. **Assembly:** Sometimes the design of some structures is only focused into the proper behaviour of the components, forgetting about the assembly procedure. Especially in our design, given the size limitations, it is crucial to assure the correct assembly of the different parts conforming the whole sensor.
6. **Costs:** The combination of the previous factors without being aware of the costs will lead into a non feasible project.

As a part of an iterative process, it was agreed to change the way to focus the design into a modular structure for the laboratory model. One of the main reasons to do so was the opportunity to build a flexible model capable of testing different configurations of the different parts. Therefore, another limiting factor was added to the final result: The ease of mounting and demounting some components avoiding damage of the parts in each test.

3.1 Overview of the FACIS Dust Sensor

The main structure of the FACIS dust sensor was initially limited to $10 \times 10 \times 10\text{cm}^3$ as a result of the inner distribution of the components and the design of the primary structure of the satellite. The mass limitation was set to 5 kg.

The challenge of the project was to include all the components required into the small space available to fulfill the tasks of the sensor. The main goals of the sensor are to measure the mass of the incident particles, the speed, the trajectory and their chemical composition. An incident particle will enter the front face of the sensor and will go through a shielding grid, whose function is to avoid interferences from unwanted electrical fields. The use of a bigger number of shielding grids would mean a better isolation from interferences but the space limitations will not allow to include more than one. After that, the particle will go through two tilted grids that will capture the signal due to the induced charge from the incident particles and will allow to calculate the mass of the particle, given the shape of the signal. The reason to tilt the grids is to be able to measure two components of the velocity that will define part of the trajectory. New solutions have to be found to define completely the trajectory of the particles and a piezo sensor will be included in the model to achieve this task. The particle will hit the piezo positioned at the end of the sensor and will measure the energy of the impact. Knowing the mass of the particle from the measurements of the induced charge in the grids, the module of the velocity will be calculated and the three components of the velocity will be defined. As a result, the trajectory of the particle will also be defined. After the impact, the particles will be ionised and the positive ions will be accelerated towards an acceleration grid by applying a Voltage in the target plate to be then focused into an ion detector located at the entrance of the dust sensor, whose performance will be analysed with the aid of the mass spectrometry theory. A good choice of the ion detector and piezo sensor as well as a good design will lead to accurate measurements from the incident particles during the mission duration.

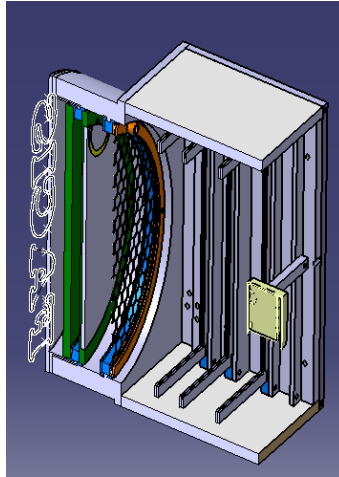


Figure 3.1: Section View of the appearance of the Dust Sensor and its components

3.2 Main Components of the design

In this section the components of the sensor are described as well as the assembly of them. During the chapter, the differences between the first configuration and the last layout is compared and a schematic view of how the CAD model has evolved. There are 2 areas clearly defined in the sensor that will be attached: The first one a cubic structure that includes the ion detector, the shielding grid and two trajectory grids; the second one a cylinder that protects the acceleration grid, the target and the piezo sensor. The reason to do 2 different geometries was focusing on a possible flight model, that optimizes the focusing of the ions to the ion detector. In the chapter 8 an outlook of how the further design iteration could look like it is explained with some detail.

3.2.1 Charge Sensitive Grids

The design of the charge sensitive grids was first thought as an array of wires separated a certain distance from each other in two different planes, attached to a frame of a few millimeters of thickness. Nevertheless, the main disadvantage of this layout is that each wire requires a charge sensitive amplifier, where neither the size limitations either costs are optimized. As a solution, instead of using an array of wires, the use of a one piece grid was established as the best option for the sensor.

As a dust particle enters the sensor, charge remains with it until the impact. The charge, if large enough, reveals the particle's presence by disturbing surface charges on the conductor grid inside the sensor as it passes by. As a result, charges are induced temporarily on the conductors, and these charge signals can be amplified and analyzed as they vary with time. On the one hand, the size of the particles will be in the order of a few micrometres, therefore the spacing between the conductive elements that form the grid should not be too large to assure the measurement of the induced charge. On the other hand, the "transparency" of the grid is also primordial to minimize the probability of encountering obstacles in the path of the particle towards the target plate. A compromise between charge measurement, transmissivity, and structural robustness is the key for a good grid design.

The material used for the grids is an alloy of beryllium Copper (BeCu) because of its out-

standing properties:

- **Electrical and Thermal Conductivity:** Transmits efficiently electricity and it is used for many electronic connectors. The alloy is non-sparking and non-magnetic.
- **Strength:** The great Tensile Strength ranges of BeCu is one of the main reasons to use this material for a structure that will have to withstand loads during the launching phase of the satellite, including acoustic, dynamic and vibrational loads.
- **Corrosion Resistance:** Alloy 172 is commonly used in environments where corrosion plays an important role. To prevent oxidation from atomic oxygen, the solution could be use this alloy.
- **Machinability:** BeCu can be metalworked, formed and machined with ease. Therefore can retain its shape and properties after being heat treated to the desired hardness. However, care must be taken as BeCu dust is poisonous.
- **Hardness versatility:** The alloy can be either softened or hardened as needed by applying different heat treatment processes. Heated one way, it becomes the strongest and hardest of its alloy counterparts. In fact, it achieves a hardness that rivals high-grade alloy steels while retaining the other favorable characteristics of BeCu (like electrical conductivity and corrosion resistance).
- **Cost**

Transmissivity of Grids

The transmissivity factor it is known as the transparency of the grid or in other words, the surface occupied by the grid configuration compared to the front squared area. Some other sensors have used this configuration before¹, and the dimensions are similar to the ones used for other missions like Destiny+. Further design iterations may need to compute the value due to changes in the grids, and it is easily computed by just adapting the hexagonal geometry in the Catia file. Computing the transmissivity factor consists on dividing the free path area into the total area available to insert the grid.

$$\text{Transmissivity Factor}[\%] = \frac{\text{Free Path Area}}{\text{Free Path Area} + \text{Hexagonal Grid Configuration}} \cdot 100 \quad (3.1)$$

In our design we have 3 identical square grids, and one circular acceleration grid. From the drawings we can obtain the factor as a function of the geometrical parameters and the Volume computed with CATIA.

For the squared grid:

$$\begin{aligned} \text{Volume}_{\text{Occupied}} &= \text{Volume}_{\text{CATIA}} - (2 \cdot d1h1th + 2 \cdot d2h2th) \\ \text{Transmissivity Factor} &= \frac{d2 \cdot d1 - \frac{\text{Volume}_{\text{Occupied}}}{th}}{d2 \cdot d1} \end{aligned}$$

For the circular grid:

$$\begin{aligned} \text{Volume}_{\text{Occupied}} &= \text{Volume}_{\text{CATIA}} - \pi \cdot th \cdot ((r_2)^2 - (r_1)^2) \\ \text{Transmissivity Factor} &= \frac{\pi \cdot (r_1)^2 - \frac{\text{Volume}_{\text{Occupied}}}{th}}{\pi \cdot (r_1)^2} \end{aligned}$$

¹The configuration consists on a honey comb layout shown in ??.

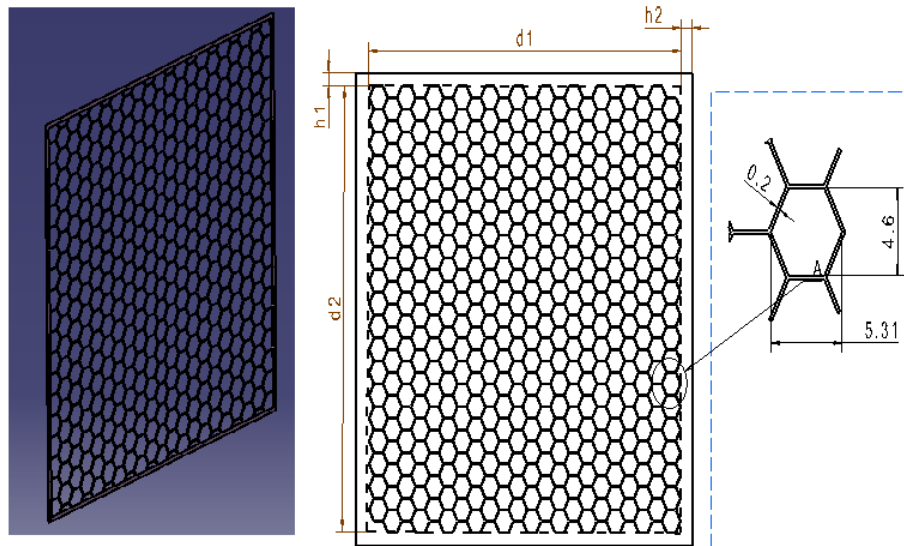


Figure 3.2: Grid Geometry and details of the grid's dimensions

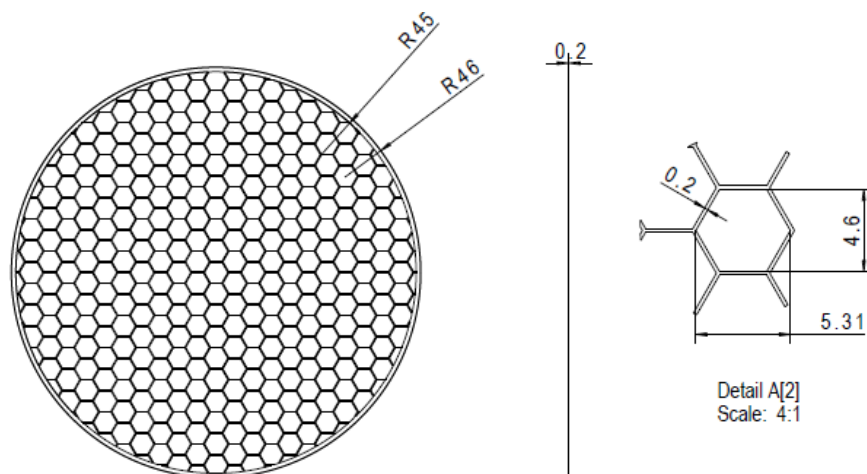


Figure 3.3: Grid Geometry and details of the acceleration grid

The final transmissivity is the result of multiplying the values obtained for each grid. Therefore we have one shielding grid, two trajectory sensors (index 1) and an acceleration grid (index 2).

$$\text{Transmissivity Factor TOTAL} = T_1 \cdot T_1 \cdot T_1 \cdot T_2 \quad (3.4)$$

The value obtained for the current design was given for the following geometrical specifications:

Parameter	Value	Units
d1	86	mm
h1	1	mm
d2	89	mm
h2	1	mm
r1	45	mm
r2	46	mm
Vol CATIA Squared	2.65 E-07	m ³
Vol CATIA Circular	1.62 E-07	m ³
th	0.2	mm
Transm. Factor Squared	83	[%]
Transm. Factor Circular	92	[%]
Transm. TOTAL	52.3	[%]

3.2.2 Frames of Grids

Holding the structure of the grids, two parts of aluminium frames are attached leaving the grid in the middle of both. The design was made so that the grid fits perfectly the dimensions of the frames, leaving a small area for the electrical connection with the electronic components that will amplify the charge signal induced in the grids.

There is no need to screw both components as the isolation PVC structures will not allow the movement of the frames in any directions. The material chosen for these frames was aluminium due to the low density and ease of manufacturing. Besides, the Workshop of the IRS usually works with this material.

However, producing this kind of component as a single piece, was not feasible with the workshop, as they could not assure the accuracy of the final result due to the small dimensions and thickness of the frames. To solve this problem, different ways of production had to be considered, leading to the techniques of laser cutting or 3D printing. Nowadays, the 3D printing in metallic materials is becoming more usual. The advantages of producing the frames with 3D printing is the micrometrical accuracy for small components, as well as avoiding rounding edges that may lead to a bad assembly of the structures. On the other hand, the main disadvantage is the increase of the costs of production.

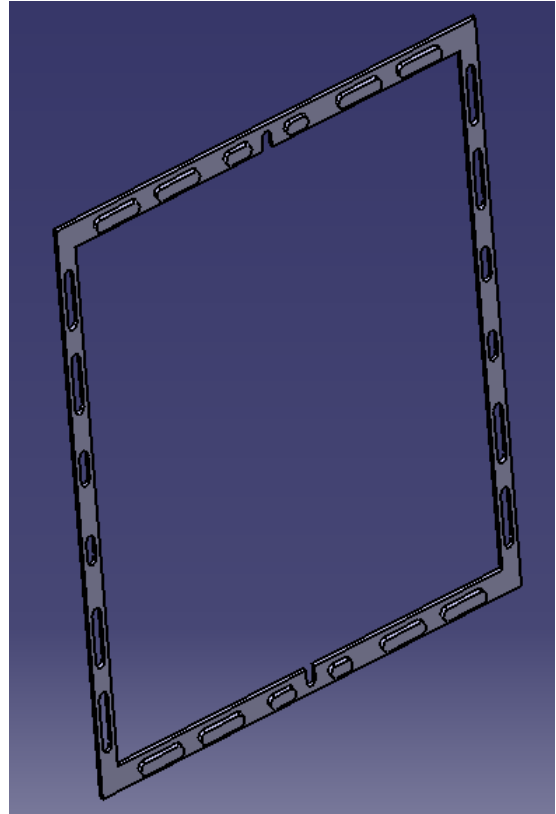


Figure 3.4: Frame CAD design

The current situation led to a reconfiguration of the frame structures to be capable of producing them in the university, and some results that could be feasible were developed, but required widening the thickness of some other components. As a result, the distance between the grids would have to be too small and interferences in the charge induced signals would appear. The picture above shows the solution proposed for the frames production.

3.2.3 PVC Attachments

This component was changed several times due to modifications on the layout of the other parts. We had to incorporate an element capable of isolating the grids from the housing structure to avoid electromagnetic interferences while reading the signals. At least 3 mm were considered as the minimum distance between the grid frames and other surfaces of the sensor to avoid this situation². The first configuration was thought in a way that they would be glued to the housing structure and bonded to the frames with PEEK screws. Using glue was discarded afterwards because it would lead to inaccuracies such as tilting the angle of the grid because of differences on the glue thickness applied in the 4 corners. Besides, in further iterations some structural stud-

²Value proposed by members of the IRS, that needs to be tested.

ies will have to be carried out such as vibrational tests, and this solution may not be the best one.

The final result was a PVC piece that avoided to interfere in the free path of the particles towards the sensor but at the same time holding the frames by screwing them to the support L sections that will be described afterwards. Each frame requires four PVC attachments (for the four corners) and it is useful for the squared grids. Therefore, having 3 squared grids we will need 12 PVC components.

The workshop currently counts with PVC laminates that would reduce the production costs but the terminal of the tool of the milling machine required to make the cavity on this element does not have the length enough to respect the dimensions of the design. The solution proposed was to contact different milling experts companies to get an overview of the possibilities of buying a tool that could produce the components. Some companies were asked such as *FRAIXA SA*, *ABRATOOLS*, *Sandvik*, *GMW MACHINES GMBH* or *BRAUER SYSTEMTECHNIK GMBH* but in all their catalogues the combination of the diameter of the tool and the usable length was not suitable for the manufacturing. However, *Sandvik* [9] offered the possibility of designing a tool with the required specifications. Two options had to be considered: if to buy this tool regarding the costs of its production or to look for the price using 3D impression. When comparing the costs of buying a customized milling tool with the quotation obtained to produce the components with 3D printing, it was concluded that buying the tool would reduce the costs as one single 3D printed component would rise up to 35Euros³ and the price of the milling tool would be worth it after producing more than 4 components.

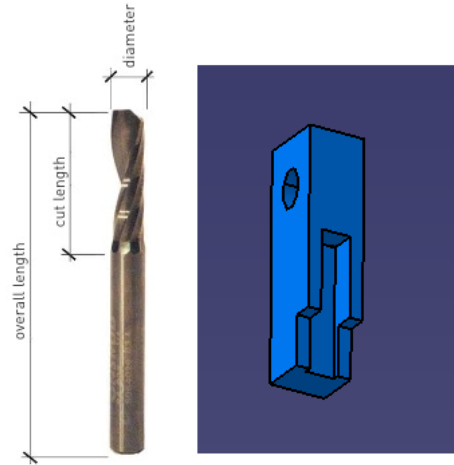


Figure 3.5: On the left a milling tool with the usable length and Diameter of operation. On the right the CAD design for the PVC component.

3.2.4 Support Modular Alluminium Structures

On the first drawings, the support aluminium structures were thought to be designed as one solid piece to be attached to the front side of the housing assembly as shown in the first picture from figure ???. The advantages of this configuration would be that the attachments of the grids and frames could be done out of the housing structure (ergonomy), and the assembly to the housing would be really easy. Some designs were tried to make the bonding width surface with the PVC attachments as low as possible to assure a bigger field of view, but a new limitation was encountered: the screws dimensioning. The minimum diameter for the threading with which the workshop can work for thin structures would be $M = 2.5$. As a result, the width was increased 3mm for each support component and the grids had to be reduced the same amount in both

³In the best case of quotations obtained by the *Solitium Company*

sides, losing 6mm in each direction. Moreover, from the experience of the workshop, the geometry was too difficult to be manufactured and some changes needed to be done to avoid the bending or even the fracture of the components. They suggested building two pieces (U section and L section) and attach them somehow. Some options were contemplated but the required screws would contact the frames and the electrical isolation would be lost.

Finally, a solution was found by dividing the solid piece in two pieces, but in 2 L sections instead of 1 U section and 1 L section. The disadvantage here was that the assembly had to be changed as it could not be screwed to the front side of the housing. However, the change turned into an advantage because no screws were required to attach them to the housing, just a passing element through the holes designed for the housing that constraint the movement in any direction of the L sections. Besides, the modular designed was improved thanks to this solution, and the ease to be able to change the distances between the grids in a few seconds just by adding a small aluminium laminate between the L sections and the housing entrance side.

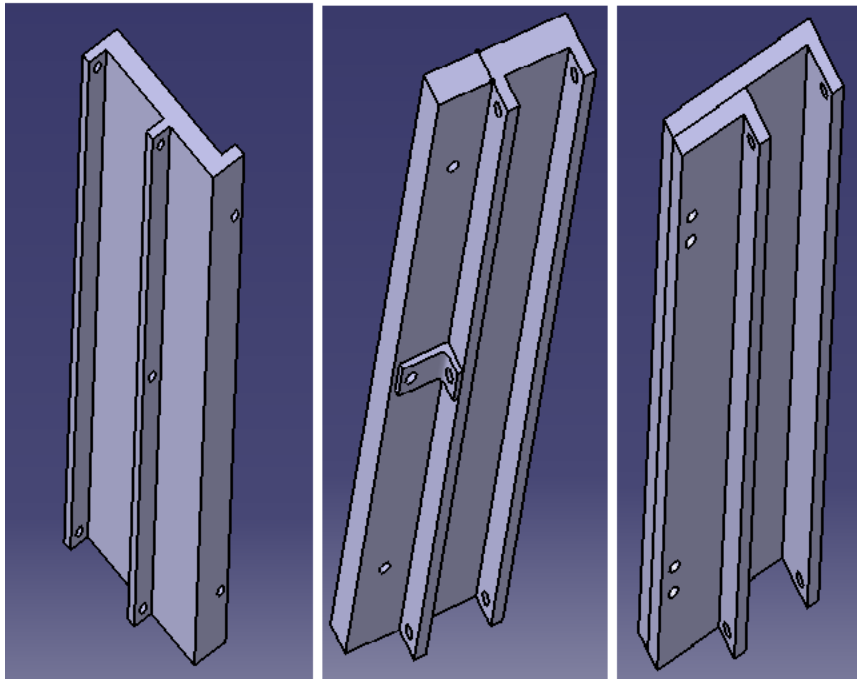


Figure 3.6: On the left first configuration. On the middle workshop suggestion. On the right final L section aluminium supports to be attached to the housing.

In the explanation of the assembly of the whole sensor at the end of this chapter 5.4 it is clear how the attachment is done and how to proceed with further laboratory tests to modify the initial standard configuration.

3.2.5 Housing Structure for the trajectory sensor area

Made of Alluminium, 4 laminates make up the protection and attachment structure. It provides stability and robustness, defining the limits of the sensor. The first two designs (shown in the picture ??) did not allow the modular configuration and after some iterations were discarded. Furthermore, more simple structures were required to make an easier assembly and the possibility to be manufactured at low costs. Two long laminates in vertical position with holes at different levels allow the constriction of movement of the support structures. Screwed perpendicular to them, 2 smaller laminates create the cubic box that form the housing of this first part of the sensor. The small laminates have also holes where to pass the cables to do the wiring with the electronic components.

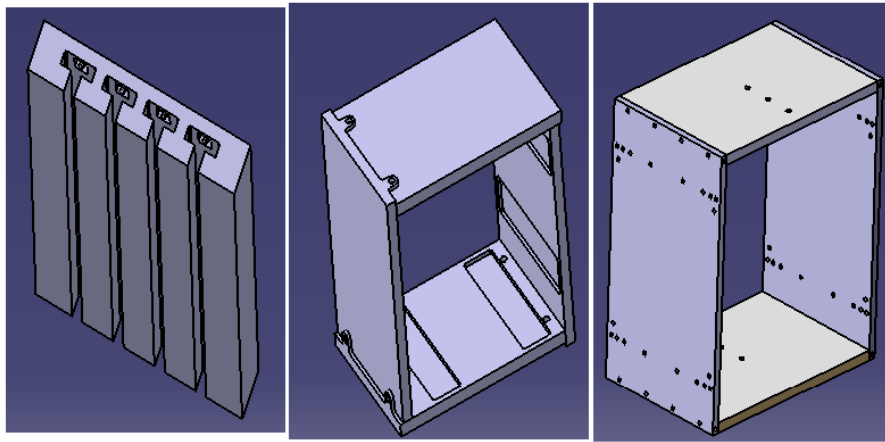


Figure 3.7: On the left and middle, first housing designs. On the right, final laminates conforming the housing.

3.2.6 Ion detector

The detection of the ions resulting from the impact of the particles in the target is one of the challenges of the project. There are plenty of possibilities in this field and taking ideas from other missions was the way to proceed to decide which one could be the best option. The first idea was to include the ion detector in the target plate making a hole in the middle of it and redirecting the ions resulting from the plasma ejected by a reflectron, but it would mean to lose plenty of surface of impact for the incoming particles and also required space to set the reflectron between the trajectory grids and the plate. The idea was then dismissed.

At this point, different options had to be considered that could exploit the available space without affecting the field of view, or at least minimizing this effect. To establish the distance at which the ion detector should be placed, the technique of the time of flight spectrometry (TOF) was studied and how it affected the mass resolution, or in other words, what was the minimum distance required to avoid the overlapping of the incident ions. Accelerating the particles towards the grids was possible by applying a difference of Voltage $E = V \cdot s$ between the target and the grid to the same kinetic energy⁴. It is possible to calculate the velocity of each ion once they

⁴ s is the distance from the plate to the acceleration grid

arrive the acceleration grid.

$$\frac{mv^2}{2} = Eesz \rightarrow v = \left[\frac{2zeEs}{m} \right]^{\frac{1}{2}} \quad (3.5)$$

The ions pass through a drift region (D)⁵ and finally, the time of flight for the different m/z (bigger for heavier ions) can be computed.

$$t = D \cdot \sqrt{\left[\frac{m}{2zeEs} \right]} \quad (3.6)$$

Then the time of flight spectrum can be converted to a mass spectrum knowing the values of the accelerating voltage and drift area. In the laboratory, testing the time of flight for different ions will lead to an empirical equation for the mass spectrum⁶

$$\frac{m}{z} = 2eEs \left(\frac{t}{D} \right)^2 \rightarrow \frac{m}{z} = at^2 + b \quad (3.7)$$

One important parameter to take into account is the mass resolution $m/\Delta m$ so that the signal of the different ions can be clearly distinguished in the measurements. This parameter can be optimized by increasing the time of flight of the particles as the mass resolution can be estimated as:

$$\frac{\Delta m}{m} = \frac{2\Delta t}{t} \quad (3.8)$$

To achieve this result, the solution can be using low accelerating voltages or longer drift areas⁷. Therefore, placing the ion detector as close as the front entrance of the dust sensor would increase the mass resolution of the ion determination.

With the aid of the software Wolfram Mathematica, the time of flight of an ion as a function of its mass to charge ratio was deduced; and the time gap of two ions with a difference of 1 amu⁸ was obtained. This will be helpful to see if the electronics have a sufficient time resolution to extract the results, and to see if they are able to avoid the overlapping of two incoming ions in a reduced time.

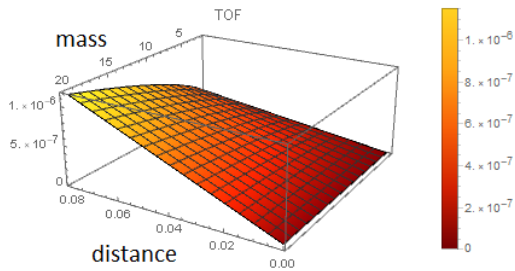


Figure 3.8: Time of Flight of an ion to the ion detector depending on the drift area distance $s = 3mm$

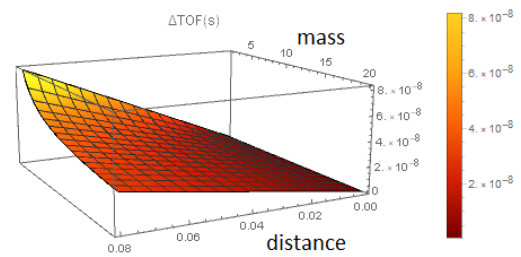


Figure 3.9: Δt between two ions of a $\Delta m/z = 1$

⁵Distance from the acceleration grid to the ion detector

⁶The accuracy of the empirical equation is proportional to the number of tests done

⁷In the presented thesis the accelerating voltage was previously defined

⁸Atomic Mass Unit

From the pictures some conclusions can be extracted. The time of flight for the ions will be within microseconds ($10^{-6}s$) and the overlapping time resolution of the electronic components to be able to measure all the incident ions should be within nanoseconds $10^{-9}s$.

Types of Ion Detectors

During the development of the project the choice of a suitable ion detector became more important as the first designs were made for electron multipliers similar to those used in other dust sensors. However, it is important to describe the different detectors that can accomplish this mission and the characteristics of them.

- **Electron Multiplier:** An electron multiplier is used to detect the presence of ions. The basic physical process that allows an electron multiplier to operate is called secondary electron emission. When a charged particle (ion or electron) strikes a surface it causes secondary electrons to be released from atoms in the surface layer. The number of secondary electrons released depends on the type of incident primary particle, its energy and characteristic of the incident surface. A typical discrete-dynode electron multiplier has between 12 and 24 dynodes and is used with an operating gain of between 10^4 and 10^8 , depending on the application.
- **Micro Channel Plate:** MCP is a plate that amplifies electron signal similar to secondary electron multiplier (SEM). Unlike SEM, MCP has several million independent channels and each channel works as independent electron multiplier. In other words, one can imagine MCP as an assembly of millions of SEMs. MCP consists of a two-dimensional periodic array of very-small diameter glass capillaries (channels) fused together and sliced in a thin plate. A single incident particle (ion, electron, photon etc.) enters a channel and emits an electron from the channel wall. Secondary electrons are accelerated by an electric field developed by a voltage applied across the both ends of the MCP. They travel along their parabolic trajectories until they in turn strike the channel surface, thus producing more secondary electrons. This process is repeated many times along the channel; as a result, this cascade process yields a cloud of several thousand electrons, which emerge from the rear of the plate.

Some considerations must be taken into account when deciding which MCP will have a better performance. First of all, the **channel bias angle**, that is an angle formed by the channel axis and the vertical axis to plate surface, is optimized for values between 5 deg and 15 deg. Channels are tilted to prevent incident particles from passing through the channels. Secondly, the **open area ratio OAR**, that is the ratio of the open area to the total effective area of the MCP and should be over the 50%. The **Diameter to thickness ratio** determine the gain of the MCP, and values over 40 are required for a good performance. The **gain** of the component can be increased by adding a second stage which disadvantage is that degrades the spatial resolution. However, when the gain increases to a certain level, noises caused by ion feedback effects become a problem. This phenomenon occurs when residual gas molecules within the channels are ionized by the multiplied electrons. The resultant ions travel back to the MCP input side along the electric field and produce false signals (dark current), degrading the signal to noise ratio. To minimize the phenomenon, two MCPs are stacked in proximity with their bias angles opposing to each other.

- **Channeltron:** Its working principle is similar to the electron multiplier but with the difference that it does not have multiple dynodes, but a glass tube with horn shape. One

of the main advantage of the Channeltron is that it can be exposed to the atmospheric pressure without problem, allowing it to break the vacuum in the system without further complications. On the contrary, the useful life of channeltrons is more reduced than the other two components analyzed.

3.2.7 Housing of cylindrical part of the sensor

Housing the acceleration grid, the target plate and the impact piezo sensor, a solid aluminium piece was attached to the squared housing. The attachment is done by screwing both with $M2.5$ mm blind screws. The initial configuration of the modular structures mentioned before, required to make a cavity in the cylindrical housing that was really problematic to be manufactured. On the first picture below these cavities in both sides are shown. After changing the design of the modular structures, the configuration of this part was much easier and the cavities were no longer needed. As a result, the production of this component was possible as well.

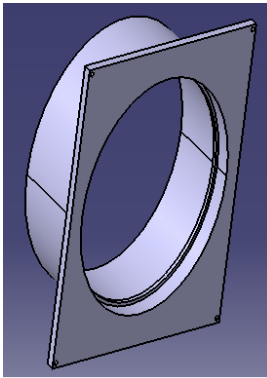


Figure 3.10: Housing before the changes were made

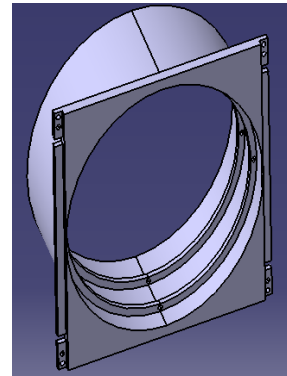


Figure 3.11: Final Cylindrical Housing

3.2.8 Modular aluminium attachment

This piece was included in the last iterations of the design to make an easier cylindrical housing structure, which until this point could become a problem to the workshop. It had to be as thin as possible to avoid the loss of field of view, and be attached somehow to the housing.

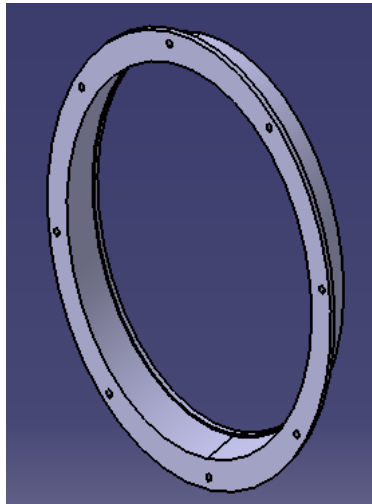
3.2.9 Frames for Acceleration Grid

Two aluminium frames protect the acceleration grid and can be attached to the insulators by screwing them. The way the housing was design make the acceleration grid be always on the same position with respect to the bottom of the sensor. However, the displacement of the target plate can be done and the acceleration distance be modified by adding some anular rings at the bottom surface⁹. The thickness of these rings will determine the increment of distance from the plate.

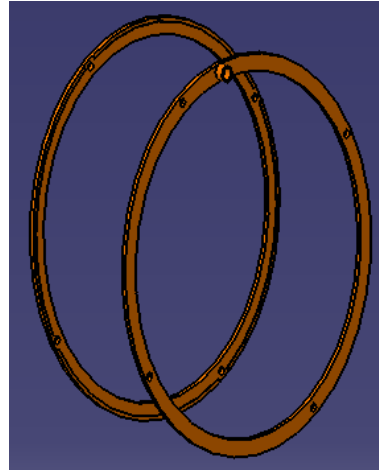
3.2.10 Insulators for the acceleration grid

To avoid the electrical interference between the grid and the housing, assuring a correct acceleration of the ions, two insulators are included in the design lying on the small ring of the

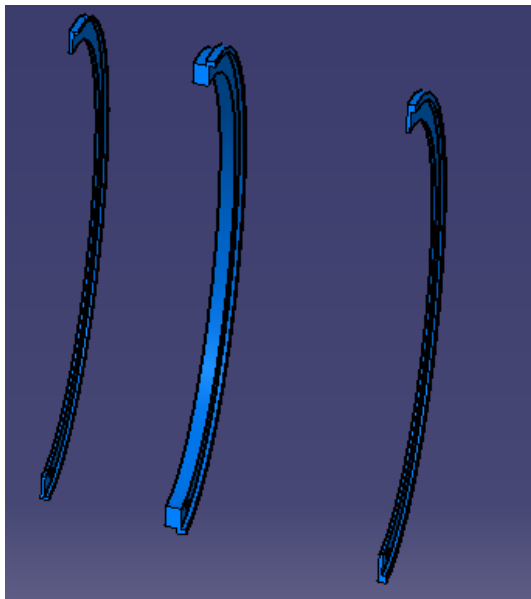
⁹Longer screws would be required if the total thickness of the anular rings is bigger than 5mm.



(a) Modular aluminium attachment



(b) Frames protecting the acceleration grid



(c) Insulators of the acceleration grid

Figure 3.12: Components of the cylindrical structure

inner surface of the housing. Screwing them to the frames will constraint them avoiding any displacement. Besides, we will have to insulate the housing of the piezo and the bottom plate (with a voltage applied to accelerate the ions backwards) needing two more structures.

3.2.11 Target Plate and Piezo Sensor

During the impact process, secondary debris (i.e., solid particulates), neutral and ionized molecules, atoms, electrons, and IR and visible light from the target and the projectile are emitted. While the light might be accessible to an optical spectrometer, the charged particles (positive and negative ions and electrons) can be influenced by electromagnetic fields and hence be analyzed with an ion mass spectrometer. A charge-sensitive preamplifier should be connected to the target to detect signals induced by the charge separation.

In order to obtain the trajectory of the particles, we need to know the three components of velocity. From the geometry of the squared grids and the time frame it is possible to compute the v_y and v_z components, as well as the mass of the particle as a function of the induced charge on the grids. Including a sensor that is capable of measuring the energy of impact would determine the module of the velocity of the particle, and the other component of speed can be deduced. From all this information the final trajectory of the particle in the three dimensions is modeled.

This sensor have to accomplish 2 missions: First of all measure the velocity of impact of the particle and also allow the ionisation of the particles. A piezo sensor was chosen to solve this situation, and in the following paragraphs the working principle, main characteristics, types, assembly possibilities and choice justification are explained.

Piezoelectric Effect

The piezoelectric effect was discovered by Jacques and Pierre Curie in 1880. They found that if certain crystals were subjected to mechanical strain, they became electrically polarized and the degree of polarization was proportional to the applied strain. The piezoelectric effect is exhibited by a number of naturally-occurring crystals, for instance quartz, tourmaline or Rochelle salt, and these have been used for many years as electromechanical transducers. A stress (tensile or compressive) applied to such a crystal will alter the separation between the positive and negative charge sites in each elementary cell leading to a net polarization at the crystal surface. The effect is practically linear, so the polarization varies directly with the applied stress, and direction-dependent, so that compressive and tensile stresses will generate electric fields and hence voltages of opposite polarity.

However this substances had a limited application range because of poor stability and limited degree of freedom in the characteristics of quarz. Here is where the piezoelectric ceramics were introduced such as barium titanate ($BaTiO_3$) and lead zirconate and lead titanate systems ($PbTiO_3$, $PbZrO_3$) which broadened the application range of piezoelectric ceramics. Here are some of the advantages of this elements:

- High electromechanical transformation efficiency
- High machinability
- High stability
- High degree of freedom in characteristics design

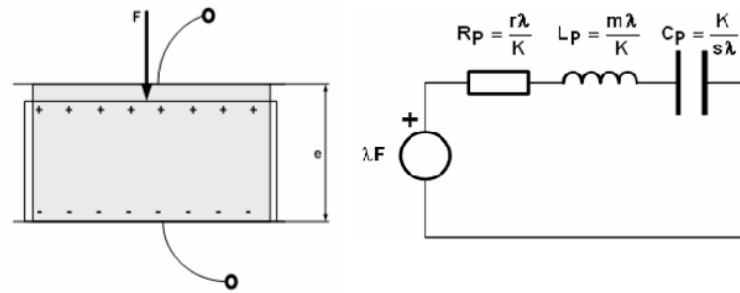


Figure 3.13: Model of the applied force in a piezoelectric sensor and analog circuit

When a signal is applied to the ceramic in a frequency matching the specific elastic frequency of the ceramic, it exhibits resonance, where it has a high electromechanical transforming efficiency. Usually the piezoceramics work close to this resonance frequency. We can model the behaviour of the material given the inertial, elastic and viscous effects that contrarrest the applied force on the electrodes as follows:

$$F = m \cdot \frac{d^2x}{dt^2} + r \cdot \frac{dx}{dt} + s \cdot x \quad (3.9)$$

where m is the mass of the cristal, r the viscosity, and s the elastic coefficient.

$$q = \frac{xk'}{e} \rightarrow i = \frac{dq}{dt} = \frac{dxK}{dt} \rightarrow F = \frac{m}{K} \frac{di}{dt} + \frac{r}{K} i + \frac{s}{K} \int i dt \quad (3.10)$$

A charge results from the strain of the material inversely proportional to the thickness of the piezo (e), and electrical current appears in a closed circuit between the terminals (electrodes). The analog circuit of a piezoelectric sensor is shown in the next picture, and the equation that represents this circuit is the following one:

$$V = \lambda F = \frac{\int i dt}{C_p} + L_p \frac{di}{dt} + iR_p \quad (3.11)$$

The transfer function can be obtained as a function of the frequency [2]

$$V_0 = \frac{Fk\epsilon}{\epsilon A \sqrt{(s - mw^2)^2 + r^2w^2}} \quad (3.12)$$

Polarized piezoelectric materials are characterized by several coefficients and relationships. In simplified form, the basic relationships between the electrical and elastic properties can be represented as follows:

$$\begin{aligned} D &= d \times T + e \times \epsilon^T \\ S &= e \times d + s^e \times T \end{aligned}$$

D = Electric flux density

S = Mechanical Strain



Figure 3.14: Transfer function of the output voltage of the sensor

E = Electric Field

T = Mechanical Stress

ϵ = Permittivity

d = Piezoelectric charge coefficient

Types of Piezo Sensors and Assembly

The piezo sensors can be divided in different types regarding different parameters such as materials (already described before) geometry, electrode configuration... etc. For the current design, the desirable component would be a piezo disc about 2mm thick that occupies the whole impact plate. Besides, there is a limitation that requires the electrodes to be manufactured in gold as the target material must have a high melting point to maximize the number of ions produced in a given dust impact event. Because a portion of the target plate is also ionized when a dust grain impacts, the target plate must be made out of a material with low cosmic abundance to avoid interference with the dust composition. The possibilities here were then reduced to Rhodium and Gold, but the manufacturers could only assure the production of the electrodes in gold, and that was our choice. However, trying to combine all of our requirements was almost impossible for any companies. After contacting *PI ceramics* which offered us a potential solution which increased a little bit the costs but assuring a good functionality of the component.

The maximum size of the piezo disc is 84 mm of diameter with 2 gold electrodes and the final price would depend on the electrode configuration to assure a good assembly of the piezo. The next paragraphs describe the different possibilities and how it could be produced.

- **Solid Pattern:** The solid electrode pattern is the most common or "standard" electrode pattern that is applied to piezoelectric ceramics. The solid electrode pattern is applied using a silk screening process to the positive and negative surfaces of the ceramic. The entire ceramic is then polarized to give it its piezoelectric properties. The solid electrode pattern is the most cost effective pattern to be manufactured and therefore results in a less expensive piezoelectric ceramic for the end customer.
- **Wrap-around:** This pattern is sometimes referred to as "WFB" or "with feedback". The wrap-around electrode pattern is typically applied to "thinner" piezo ceramics, where the

thickness is 2.00 mm or less. The un-electroded band on the electrode pattern must be as wide as the part is thick making this pattern impractical for use on very thick parts of parts with a very small electrode surface area. It is typically used to connect the electrical leads to the same surface of the ceramic. For example when it is needed to bond the opposite surface of the ceramic against a flat surface.

- **Side Tab:** The side tab electrode pattern can be used if the thickness of a ceramic is too great, relative to the electrode surface area, for the wrap-around electrode pattern. The side tap electrode pattern allows for an alternate connection to the front face of the piezoelectric ceramic when a wrap-around electrode pattern cannot be applied.
- **Insulation Band:** The insulation band electrode pattern is designed to have a reduced electrode with electrical insulation. The isolation band electrode pattern is used to isolate an electrical input from a casing or housing. The pattern can be applied to both the positive and negative surfaces of a ceramic. The isolation band electrode pattern can also be used to change the capacitance of a piezoelectric ceramic.
- **Bull's-eye:** With the bull's-eye electrode pattern, the bottom surface, the sides, and a portion of the top surface are electroded. The top surface of the ceramic has a reduced electrode pattern with an insulation band separating the positive and negative electrodes. The insulation band on the bull's-eye needs to be as thick as the ceramic. The bull's-eye pattern is typically used in nebulizer and knock sensor applications.

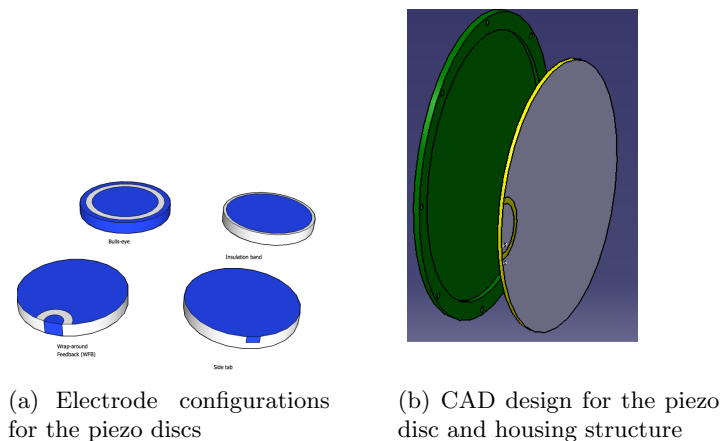


Figure 3.15: Piezo disc configurations and CAD design with its housing

The difficulty lied on how to assembly this piezo to our structure and that depended on how big the element could be manufactured, because if not too big, then an array configuration of different piezo would have to be attached to cover the whole surface. It would mean combining rectangular and circular piezos that would make loose almost a 10%¹⁰ of available impact area, increasing the wiring and number of amplifiers needed. In a nutshell, it would increase the costs and reduce the probability of detection. The configuration was then desestimated and a housing plate was designed considering a wrap-around piezo disc with a slot to include the connections. The bottom of the piezo would be sticked to the housing of the piezo with an adhesive material and then screwed to the insulators and cylindrical housing. As a first idea, the material chosen for this housing was

¹⁰Due to the housing required for each piezo

thought to be gold in case the particles did not hit the piezo but still would be ionized to be chemically analyzed. However, for the calibration in the laboratory, this requirement did not have to be fulfilled and finally the material chosen was aluminium.

for the laboratory model was aluminium in order to reduce costs, although gold to avoid interference with the dust composition.

3.3 Assembly of the Dust Sensor

In this section it is described step by step the assembly of the dust sensor for the initial configuration and how changes should be made in the laboratory to test the sensitivity and performance of the sensor.

First of all, the assembly of the housing structure is carried out, which will remain in the same position no matter what changes need to be done in further studies. As shown in the picture ??, just by screwing the long laminates to the small ones will result into a cubic structure that will not move.

The next steps will be to mount the rest of the components that will be inserted inside the housing. The main task is to place the squared grids into the frames and stick the PVC attachments in the four corners of the frames to avoid the movement of them. It will be easier to do it in a horizontal position. After that, it is required to screw the PVC components to the two long L supports as shown in the picture. The procedure is repeated with the two small L supports and the result will be the first module of the sensor.

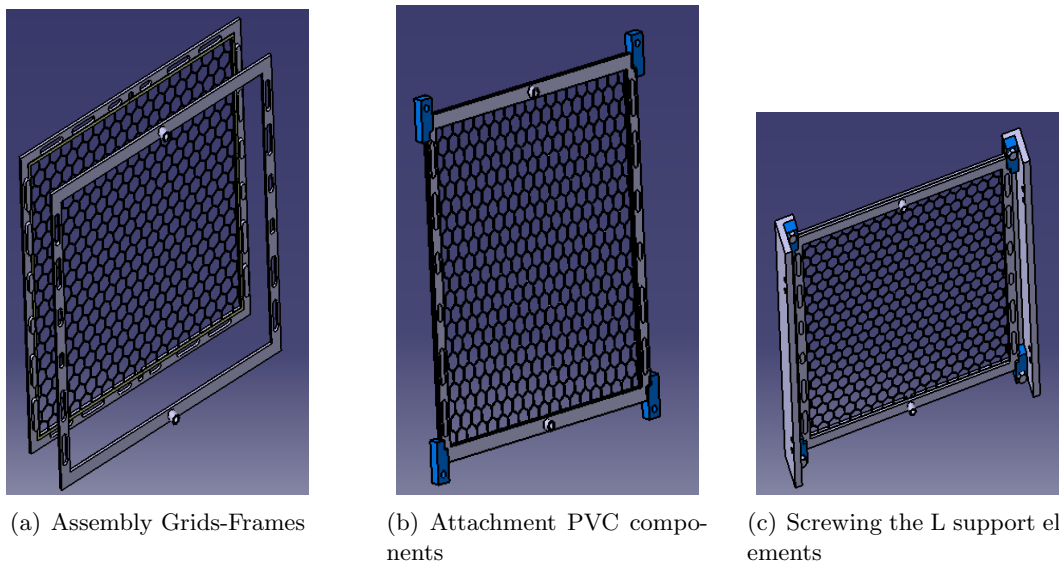


Figure 3.16: Assembly of the frames and attachments

With the second module it is equally proceeded just taking into account that the ion detector needs to be attached in the short L support and the shielding grid in the long L support. To attach the ion detector, two auxiliary aluminium bars were designed to connect the housing of the detector with the housing of the whole sensor, to be placed in the middle of the front inlet area¹¹.

Now the modular structures are pushed towards the housing, until the distance where the wholes of both housing and L support match. Then, the 2mm sticks are inserted into the wholes to avoid the movement of the module. There are different wholes in the housing and the following image shows in which ones should the sticks be introduced for the initial configuration¹²

¹¹The flight model would need at least 4 bars to be attached to the housing as a security measure, in case one bar is broken.

¹²The decision to use sticks instead of screws was made in case some changes in the configuration were needed

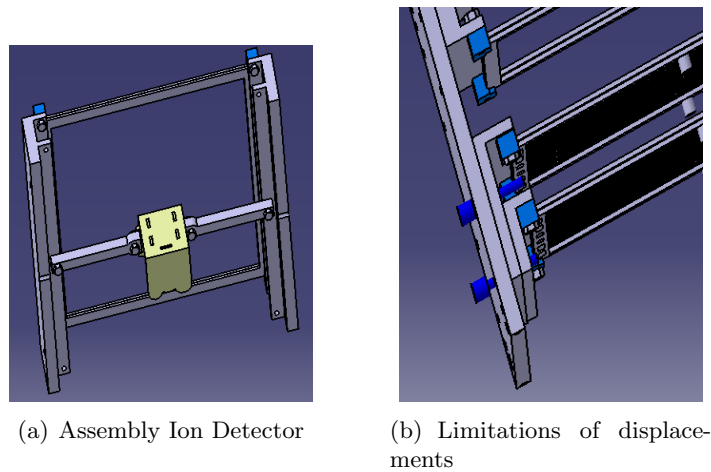


Figure 3.17: Assembly of the Ion Detector and Sticks

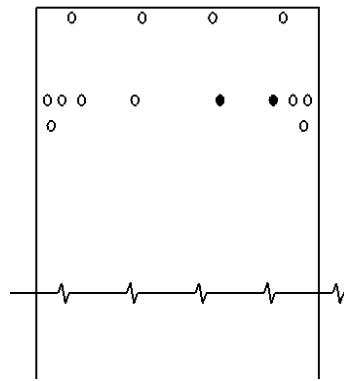


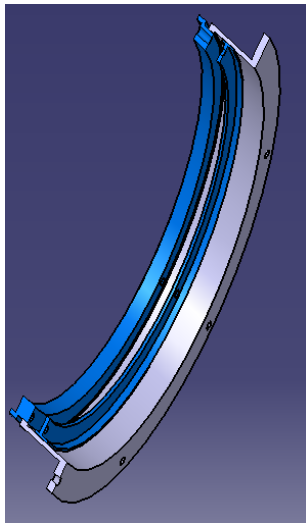
Figure 3.18: Side View of the housing. The black hole resembles the place where to stick the alluminium element to the initial configuration.

For the cylindrical structure, an strict order of assembly needs to be followed. Firstly, mount the modular structure of the target plate separated from the housing, introduce the bottom insulator for the acceleration grid into the housing, attach the modular structure by screwing it to the bottom and finally attaching the acceleration grid. The acceleration grid will be installed in one part of the insulator and both will be introduced from the front area.¹³The following pictures illustrate the assembly of these components.

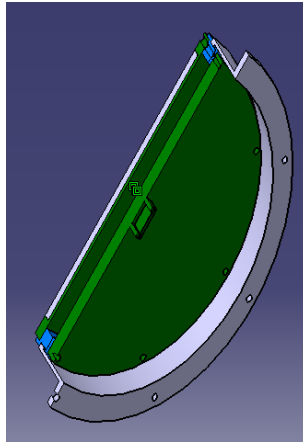
Finally, the cylindrical structure will be screwed to the squared housing and the setup will be ready to be tested. With the default configuration, the callibration of the charge induced in the grounded grids will be done, obtaining the output voltage due to the impact of the particles in the piezo sensor and after that, the chemical composition of the particles with the ion detector will be analysed. One of the crucial points will be to validate the configuration proposed to obtain the trajectory of the particles, the performance of the components with the different configurations that minimize the errors of the measurements. The next section shows how to change the assembly to achieve this study.

to avoid widening the threads after changing the layout several times. The constraint will be anyway achieved.

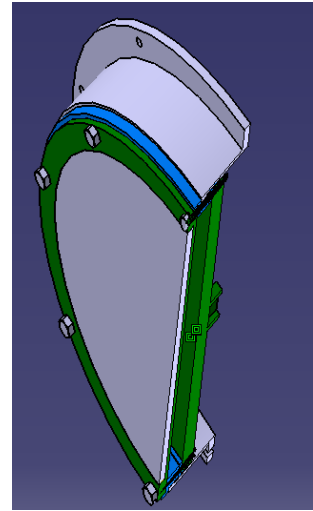
¹³We will use PEEK screws in the acceleration grid.



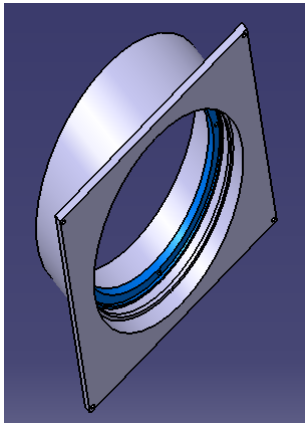
(a) 1. Assembly the insulators For Plate and Piezo



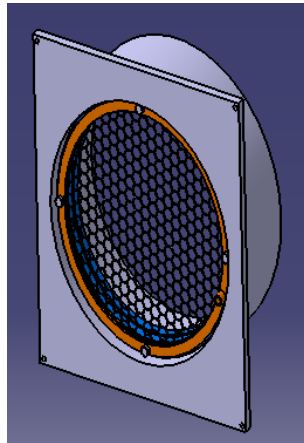
(b) 2. Assembly Piezo in its Housing



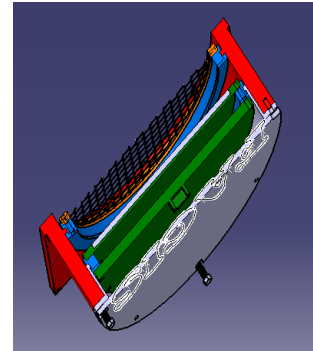
(c) 3. Attach the module with PEEK screws



(d) 4. Introduce the bottom insulator of acceleration grid

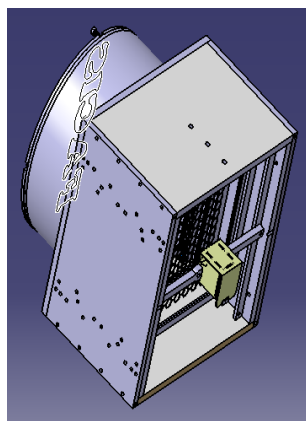


(e) 5. Assembly of the acceleration grid

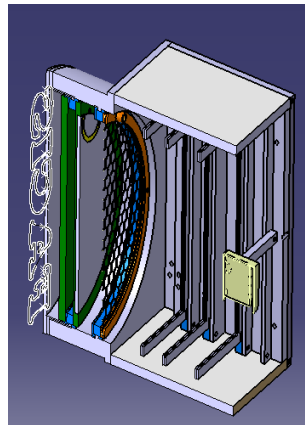


(f) 6. Assembly of Bottom Plate

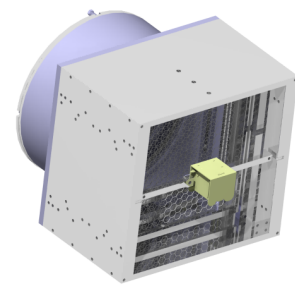
Figure 3.19: Assembly of the Modular Components



(a) Final Assembly of the Sensor



(b) Section View of the Sensor

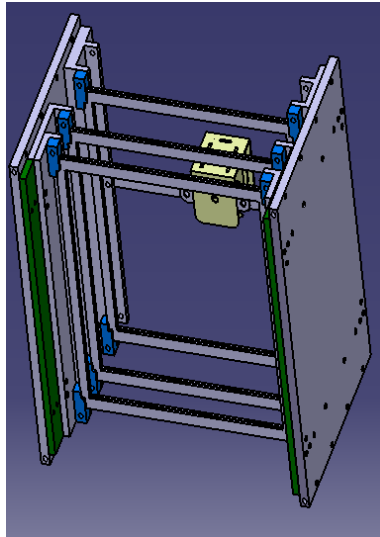


(c) Rendering of the Dust Sensor

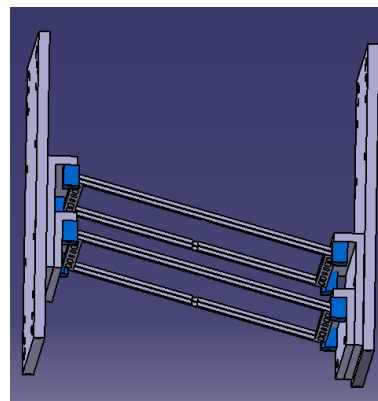
Figure 3.20: Final Assembly of the sensor and rendered model

3.3.1 Changes on assembly: Tilting Grids and Increase Separation

To test how the separation between the grids affect the measurements we have to include a laminate (green laminate in the picture) and the smaller L support will be able to be translated to a bigger separation distance. The distances chosen to be tested are 15mm¹⁴, 20mm, 23mm. There is also a possibility to attach the first grid to the other side of the L support to analyse a bigger distance, but that would require to demount the structure to screw the PVC attachments again.



(a) Laminates included to test the separation of the grids.



(b) Tilting the grids to measure the trajectory of the particles.

Figure 3.21: Configurations to be made on the laboratory for testing the components

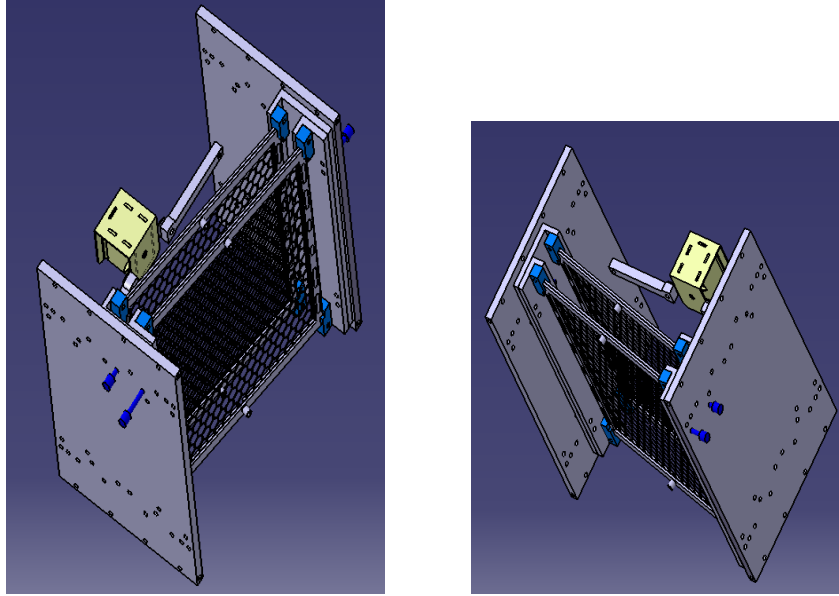
It is necessary to tilt the grids in order to assure the measurement of the trajectory of the particles. To do so, it is necessary to include different PVC attachments as the current frames are to be kept without any modification to reduce costs. There is a need of compromise between the available space, the distance between the grids, the angular resolution and the transmissivity of the grids. Increasing the tilting angle, leads to a better angular resolution, but that will mean to lower the distance between the grids and reduce the transmissivity of them.

A compromise was found for a tilting angle of 10 deg. The PCV attachments had to be widened 1mm to be able to produce them and enlarged to fit the distance between the housing laminates. If bigger angles are required, then the electron multiplier will have to be discarded as the width would be too big meaning that its structure will be out of the housing of the sensor. Besides, to keep the biggest field of view, the size of the grid and frames will have to be enlarged for the flight version of the sensor, which means more weight. The transmissivity of the grid will be reduced a 1% due to the tilting of 10 deg but bigger angles would mean lower transmissivity values.

Care must be taken when attaching the sticks to set the correct assembly for the tilted grids. The following images illustrate how it must be carried out, paying attention in the

¹⁴default

differences between both sides of the sensor.



(a) Sticking the limiters for the tilted configuration in the right side of the housing ¹⁶

(b) Sticking the limiters for the tilted configuration in the left side of the housing

Figure 3.22: Limitation elements required for the study of the tilted angle.

3.3.2 Calculation of Velocity and Trajectory of the Particles

From the layout of the sensor, the instants where the particle induces a charge in the grids, and the instant when the particle hits the piezo are obtained by the output signal. Known these instants and the geometry of the sensor, the velocity in two planes (v_y and v_z) can be obtained [4]. The charge induced by the particle in the grids is also obtained from the shape of the signal and the mass of the particle can be deduced from it. With the piezo sensor it is possible to calibrate the voltage output due to the Energy of impact and finally compute the module of the velocity of the particle. The third component of the velocity will be obtained and the trajectory can be also deduced from the velocities and time frames. The following formulation shows how to proceed with this calculation:

The speed components of the entering dust particles are:¹⁷

$$v_z = \frac{d_0 + d_1 + d_2}{t_3 - t_0}$$

$$v_y = \frac{d_1}{t_2 - t_1} - v_z$$

$$v_x = \sqrt{v^2 - (v_z)^2 - (v_y)^2}$$

and the distance at which the particle enters the detector is:

$$y_0 = \cot(\text{tilt}) \cdot \left(\frac{t_1 - t_0}{t_2 - t_1} \cdot d_1 - d_0 \right) - \frac{t_1 - t_0}{t_3 - t_1} \quad (3.15)$$

¹⁷ v_x From the calibration of the piezo

Therefore, the angle of incidence of the particle will be:

$$\tan(\alpha) = \cot(\text{tilt}) \cdot \left(\frac{1}{v_z} \cdot \frac{d_1}{d} - 1 \right)$$

$$\tan(\beta) = \frac{v_x}{v_z}$$

For the calculation of the trajectory, the incidence of the particle in the piezo sensor has the following coordinates:

$$z_3 = d_0 + d_1 + d_2$$

$$y_3 = y_0 + v_y \cdot (t_3 - t_0)$$

$$x_3 = x_0 + v_x \cdot (t_3 - t_0)$$

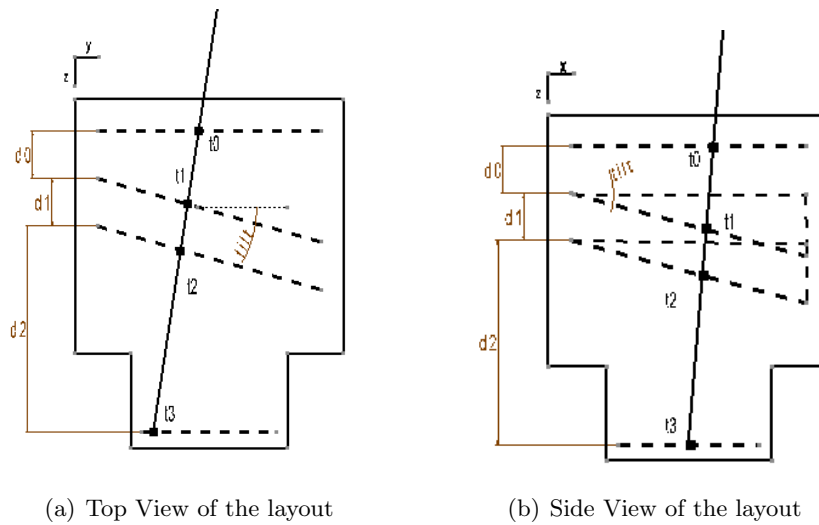


Figure 3.23: Particles going through the sensor with angles of incidence

From the formulation the trajectory of the incident particles can be deduced. The accuracy of the measurements depends highly on the sensitivity of the piezo sensor and on the dispersion of the measurements on the laboratory. Testing different angles of incidence will be the way to proceed to validate this procedure. In case the method does not give precise results, the complete trajectory cannot be totally defined but limitations for the module of the velocity and x coordinate at the entrance will determine the trajectory. Those limitations are defined by the following formulation:

$$-\frac{D}{2} \leq x_0 \leq \frac{D}{2}$$

$$\sqrt{(v_y)^2 + (v_z)^2} \leq |v| \leq \sqrt{(v_y)^2 + (v_z)^2 + \frac{(x_3 + 0.5 \cdot D)^2}{(t_3 - t_0)^2}}$$

4

Field of View

The determination of the most suitable ion detector for the current design depends on different parameters as said before. There is a need for compromise between all of them, but the importance of the field of view is primordial in this component. So as to compare different items and configurations, some assumptions are being made to simplify the study, but at the same time having accurate results. The input for the calculation will be the angle of incidence of the particles and we can see the configuration in the following images:

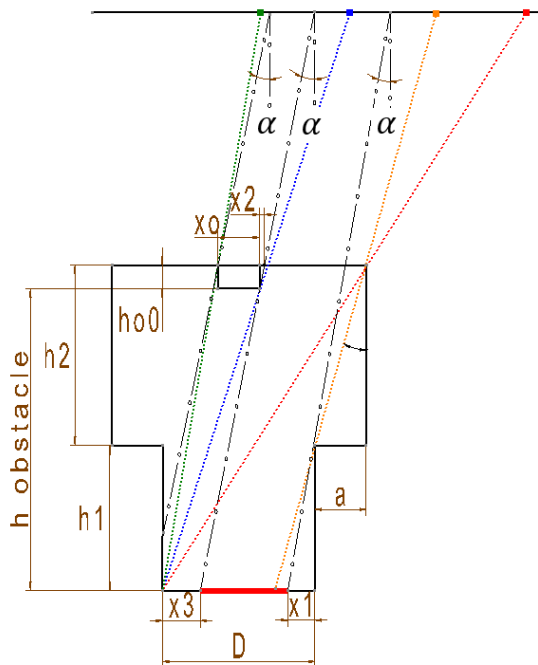


Figure 4.1: Top View of the incoming particles with a certain α

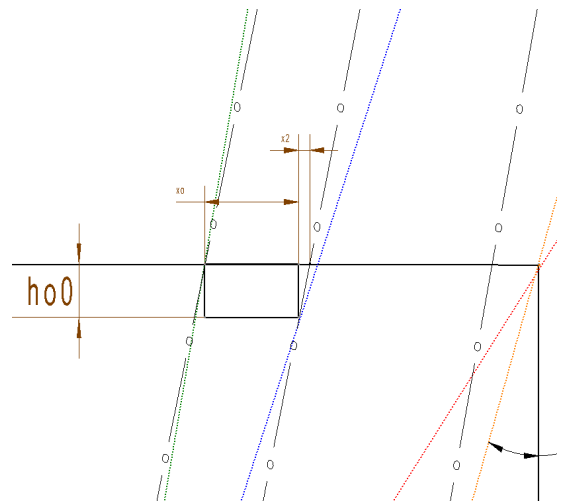


Figure 4.2: Detail of the distance x_2

Where the lines with colours represent those angles that can be calculated with the geometry of the structure.

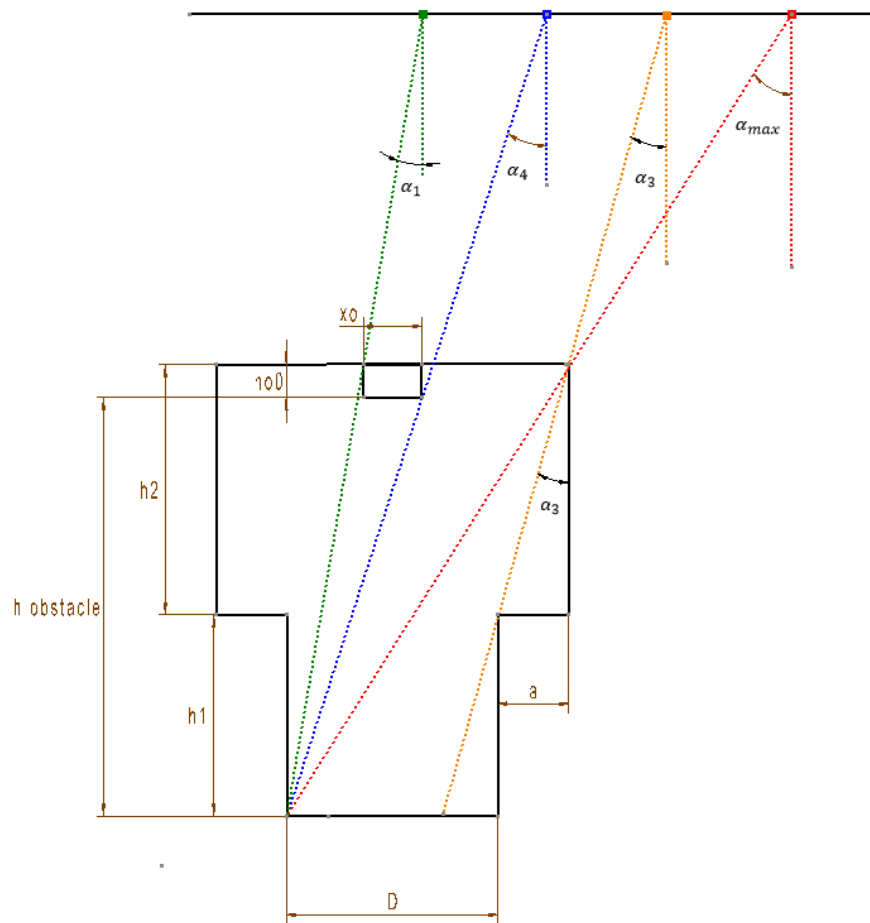


Figure 4.3: Angles obtained from geometry

The parameters that remain constant due to the layout are shown in the following table:

Include table with data

The solution of the calculation or output parameter will be the Area of the plate available for the different angles of incidence. Due to the fixed position of the dust sensor inside the satellite, it is not possible to change its orientation to measure a bigger amount of particles. Therefore, the distribution of the incoming particles is completely random and the weight of the solution for each angle of incidence is the same. The solution is divided in two:

- **x1**: Interference of the housing of the design
- **x3**: Interference of the ion detector

From the drawing of the top view of the sensor, there are some ranges of angles of importance for the incoming particles (taking into account that in this example the plate has a circular shape, and the frontal section of the ion detector is squared):

- 0° Refers to the non incidence incoming particles, where the particle "sees" the whole

plate except the section of the ion detector. In the following image the front view of the sensor and the sensitive area are shown

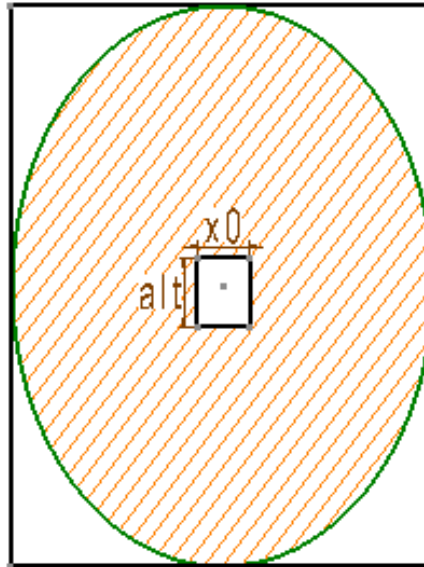


Figure 4.4: Front View of a particle with 0° incidence.

- $< \alpha_1$: The calculation of the sensitive area results from the interference of the whole shadow of the ion detector on the plate and the interference are of the housing of the sensor. This angle shows one-side ion detector interference to the free path of the particle.
- α_3 : This angle refers to the tangency line between the inlet housing of the trajectory sensor and the inlet housing of the spectrometer.
- α_4 : This angle refers to the second-side ion detector interference. For bigger angles of incidence, the ion detector it is not an obstacle for the particles to hit the plate.

In this study it is important to make some assumptions to have an accurate result of the available area of the plate for each angle of incidence. From 0° to angles lower than α_4 the front view of the sensor changes in a way that the shadow of the ion detector "moves" with respect to the circular plate, and the circular plate "moves" with respect with the squared section of the housing at the bottom of the sensor. The relative "movements" of both shadows have opposite directions, and the rate of movement can be calculated as the slope of a linear function (see the following pictures):

The solution has been computed as a parametric study, depending on the dimensions of all the parts. Only changing this parameters, we will be able to compute the total area available for any components. Therefore, the automation of the field of view is completed and will be useful

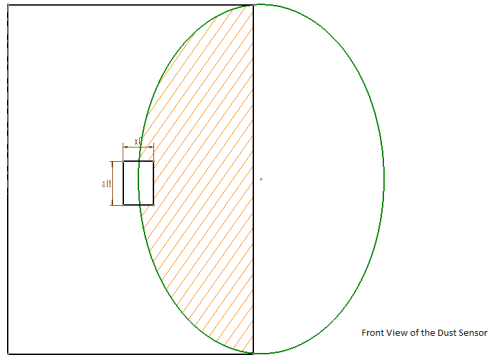


Figure 4.5: Front View of a particle with an angle of incidence lower than α_1° .

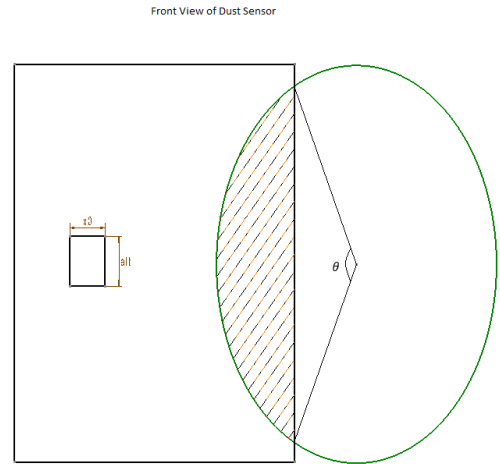


Figure 4.6: Front View of a particle with an angle of incidence equal to α_4° .

to compare different options. The formulas to compute these sections are described below.

$$\begin{aligned}
 x1 &= \begin{cases} \tan(\alpha) \cdot h_1 & \alpha < \alpha_3 \\ \tan(\alpha) \cdot h_{TOT} - a & \alpha > \alpha_3 \end{cases} \\
 x2 &= \tan(\alpha) \cdot h_{obst} \\
 x3 &= \begin{cases} x2 + x_{obst} & \alpha < \alpha_1 \\ x_{obst} + \frac{(\alpha - \alpha_1)x_{obst}}{\alpha_4 - \alpha_1} & \alpha_1 < \alpha < \alpha_4 \\ 0 & \alpha > \alpha_4 \end{cases}
 \end{aligned} \tag{4.1}$$

Once the distances x_1 and x_3 are calculated, the goal is to compute the areas of the shadows. Here, the shape of the ion detector plays an important role. The first image shows the example of a squared section ion detector. Once the procedure is defined, the total effective area for each angle of incidence is calculated, and the sum for all the available angles of incidence gives an estimation of which component has a bigger probability of measuring the incoming particles. In the following image the effective area for a component with the same height and thickness as the R8811 electron multiplier but with half of the width is shown as an example of the sensitivity given one angle of incidence. The results will not be discussed as further improvements of the method are done in the next section 4.1.

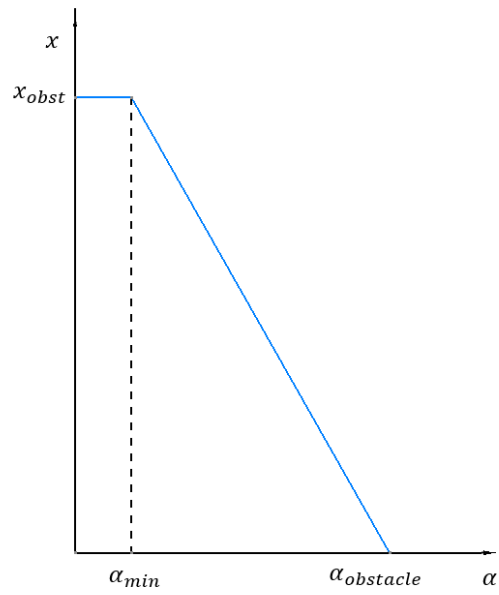


Figure 4.7: Calculation of the distance x_3 depending on the angle of incidence.

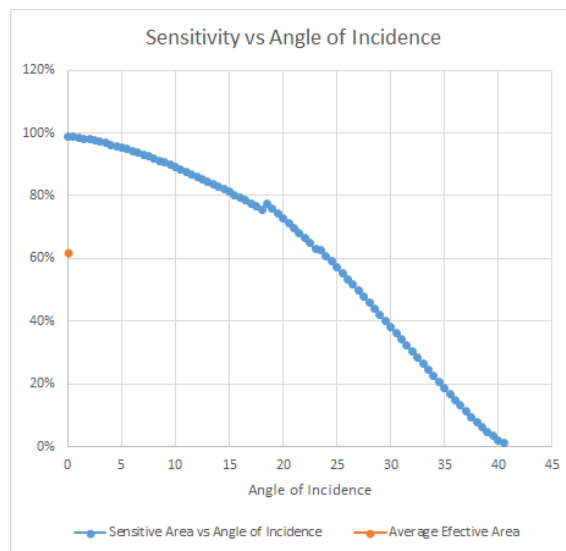


Figure 4.8: Example of the probability of detection for different angles of incidence in one plane.

4.1 Field of View in 3D

The previous study was focused on an angle of incidence α in the xy plane and no deviation in the yz plane. However, the incidence of the particles is completely random and all the cases must be taken into account. Therefore, the angle of incidence in the xz plane has also been studied, β , and the combination of both can also be computed.

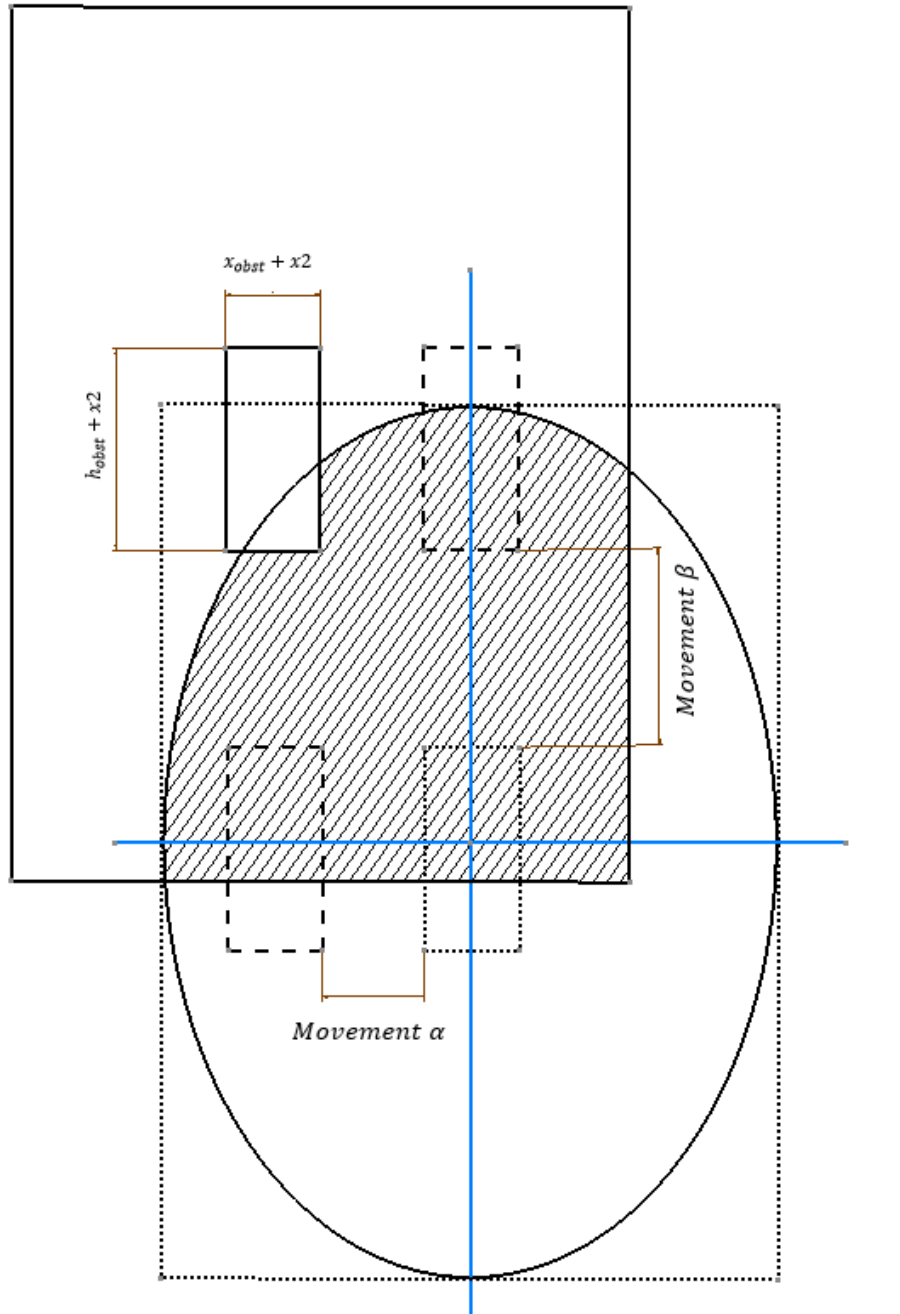


Figure 4.9: Superposition of angles of incidence that results into a shadow in the plate

The given image shows the superposition of both angles, and the procedure to compute the

solution is explained in this section.

The expressions for the calculation of the distances in the plate are similar to the ones explained before, changing the dimension "x" for "alt". Working with an ion detector of rectangular shape, the lines that form this rectangle are modeled. They are named with numbers (1,2,3,4) and the following distances, that depend on the angles of incidence, can be obtained.

$$\begin{aligned} x_{side4} &= \frac{\alpha \left(\frac{1}{2} (x_{obst} + x_{2\alpha}) + r \right)}{\alpha_4} - \frac{1}{2} (x_{obst} + x_{2\alpha}) \\ y_{side1} &= \frac{\beta \left(\frac{1}{2} (alt_{obst} + x_{2\beta}) + r \right)}{\beta_4} - \frac{1}{2} (alt_{obst} + x_{2\beta}) \end{aligned} \quad (4.2)$$

Therefore, the following expressions will define the lines (called bars in the software).

$$\left. \begin{aligned} x_{bar4} &= x_{side4} \\ x_{bar2} &= x_{obst} + x_{2\alpha} + x_{side4} \\ y_{bar1} &= y_{side1} \\ y_{bar3} &= alt_{obst} + x_{2\beta} + y_{side1} \end{aligned} \right\} \text{Equations that define the geometry of the ion detector}$$

Given the equation of a circle (that will be our target plate), the intersection of it with the different bars will resemble the appearance of the shadow in the plate. Each bar that defines the detector has a counter that is activated when the bar is intersected by the plate.

$$x^2 + y^2 = r^2$$

In the following image, the possible intersections are shown as well as how the counters are activated. Once the points are calculated, obtaining the area is a matter of geometry.

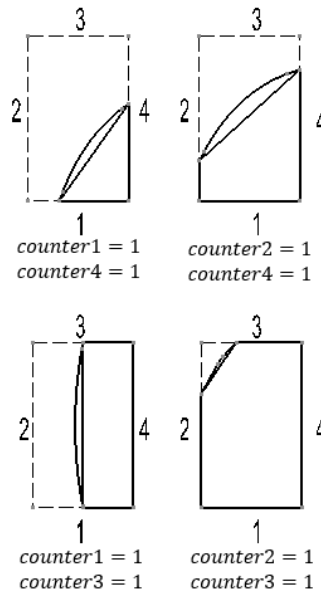


Figure 4.10: Activation of counters depending on the angles of incidence

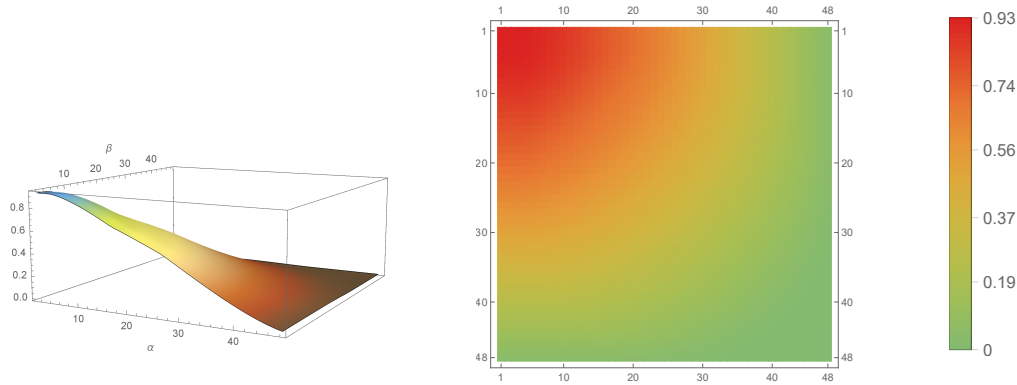


Figure 4.11: Visualization of the Field of View of R8811 Hamamatsu Electron Multiplier and 2D Representation

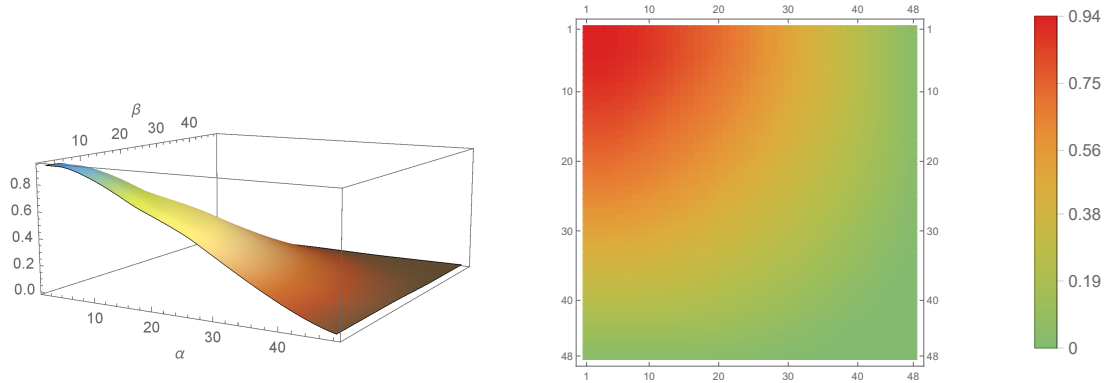


Figure 4.12: Visualization of the Field of View of Disc Micro Channel Plate and 2D representation

Automating the procedure to obtain all the possible solutions, will mean to be able to compute the total effective area for all the incoming particles. Studying this value with variations on the geometry of the components, will be helpful to optimize the structure of the sensor in further iterations.

$$\begin{aligned}
 x_{1\beta} &= x_{1\alpha} \\
 x_{2\beta} &= x_{2\alpha} \\
 x_{3\beta} &= \begin{cases} \text{alt}_{\text{obst}} + x_{2\beta} & \beta < \beta_1 \\ \text{alt}_{\text{obst}} + \frac{(\beta - \beta_1)\text{alt}_{\text{obst}}}{\beta_4 - \beta_1} & \beta_1 < \beta < \beta_4 \\ 0 & \beta > \beta_4 \end{cases} \quad (4.3)
 \end{aligned}$$

With the aid of the software *Wolfram Mathematica* the solution for different components can be computed and afterwards compare them. Visually, it is easier to plot the values from the matrix than observing the matrix itself. It is visually easier to identify which angles of incidence are those that maximize the field of view, and how the structure could be modified in order to obtain a better probability of detection with different geometries. Besides, it can become a helpful tool in the laboratory to determine if some events are likely to be measured or not.

From the results it is difficult to notice big changes in the Field of View as the dimensions are small compared to the size of the sensor. Computing the average value we observe that the

MPC has almost a 2% more of probability of letting the particles hit the piezo sensor. Therefore, regarding the geometry, the MCP disk is more efficient.

The next step was to develop an interface that gives an overview of the incoming particle if the angles of incidence to be tested are set. It can be used to see if the incoming particle hit the plate or the measurement was due to some noise or interference. In the following pictures we can see how the interface looks like for two different geometries. If further obstacles are included in the model (note desired) then they will have to be modeled to be included in the study.

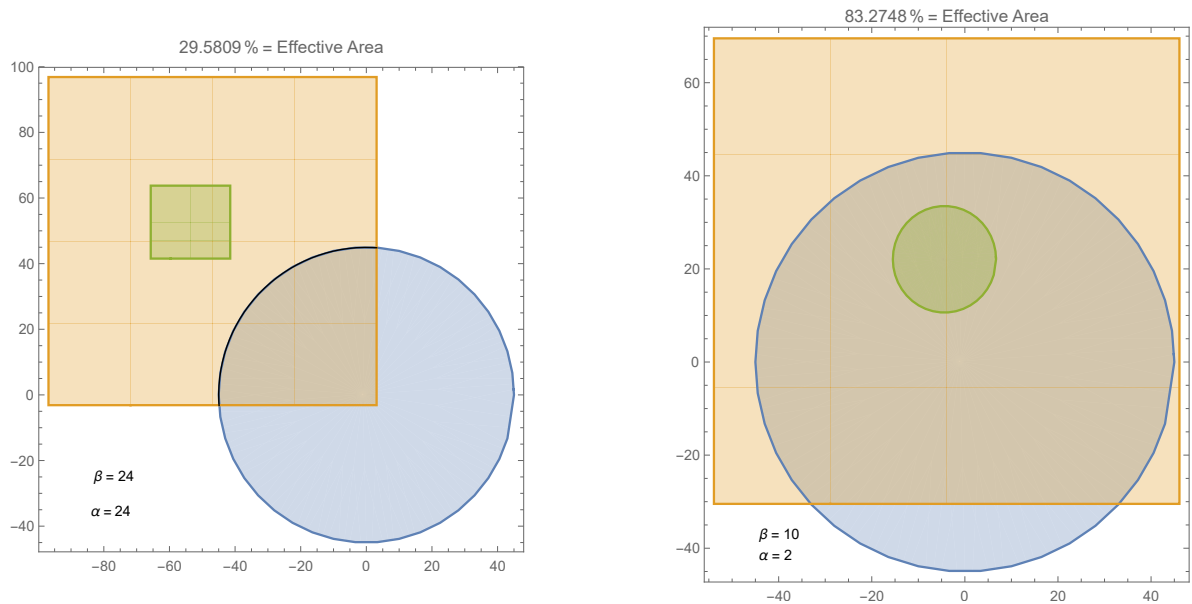


Figure 4.13: Visualization of the Field of View of two ion detectors. On the left, the R8811 electromultiplier from Hamamatsu. On the right, a circular MCP from Hamamatsu.

5

Study of Sensitivity

The sensitivity of a component is understood as the capability that it has to calculate accurately the measurements, given a wide range of inputs. In this case, the study of the sensitivity will be focused on the piezo sensor in order to decide in further studies the choice of the suitable electronics (amplifiers and converters).

The **sensitivity** reflects the Voltage that the electronics should be able to recognize in order to amplify the signal. The **inputs** for the study are the velocity and the size of the incoming particles¹. Modelling the applied Force in the piezo as an impulse due to the hypervelocity impact, the following formula allows to obtain the impact force:

$$\text{Impulse} = \int_{t_1}^{t_2} \text{Force} \cdot dt = \text{Mass} \cdot \Delta \text{Velocity}$$

The Force will depend then on the mass, the velocity and the rise time of the impact. The calculation of the rise time is also dependent on the velocity and can be estimated as:

$$\Delta t = \frac{2 \cdot \text{diameter}}{v}$$

Once the Force is established, the charge induced in the piezoceramic element will be dependent on the material properties and the output voltage on both material properties and on its geometry.

In this section the response of different piezo sensors is being studied for different density values of the particles. First of all, a comparison between two piezo with similar geometry but different electro-mechanical properties will be carried out. After this comparison, the effect of the geometry is being also analysed. A further step is to observe the influence of the density of the particles on the sensitivity of the piezo sensor. One consideration must be taken into account: the measuring electronic components will make an effect on the final sensitivity as they will increase the total capacitance of the circuit. Therefore, this shift should be minimized.

¹Considering the particles as spheres with a certain density and diameter, and the velocity applied in a perpendicular plane to the plate surface.

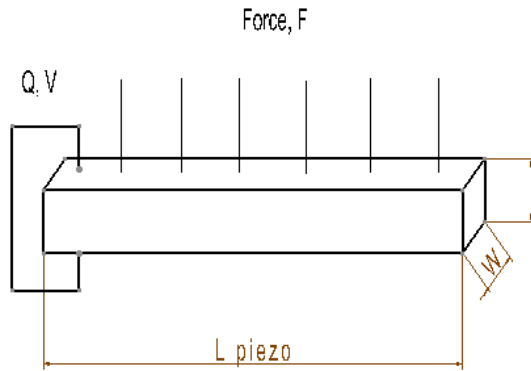


Figure 5.1: Force applied on the piezo sensor. Charge induced and output voltage.

$$\Delta Sensitivity = f(\Delta Capacitance^{-1}) \tag{5.1}$$

5.1 Sensitivity vs Material Properties

For this study, two piezo sensors PZT have been selected, that can be found in the Appendix C8: PIC155 and PIC300.

The sensitivity obtained for both components is summarised in the following graphics. It is clearly seen a better sensitivity in the Piezo PIC155. Some studies implemented for another piezo sensors show that the influence of the parameter g_{33} has a greater influence on the voltage output than the parameter d_{33} . For this reason, the bigger the value of the parameter g_{33} , the better would be the senssitivity. In the following images the comparison between the two piezos is shown.

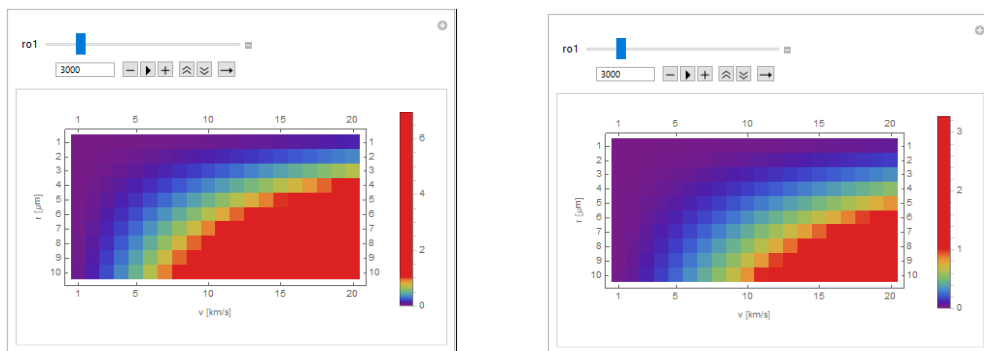


Figure 5.2: Sensitivity depending on the piezoelectric voltage coefficient. On the left $g_{33} = 53 \cdot 10^{-3}Vm/N$. On the right $g_{33} = 25 \cdot 10^{-3}Vm/N$

5.2 Sensitivity vs Sensor Size

For the design, the size of the sensor is important to determine, as well as how the sensitivity changes if the dimensions are modified. On the images, a change in the diameter of the piezo sensor was made, while the thickness is dependent on the diameter of the piezo sensor.

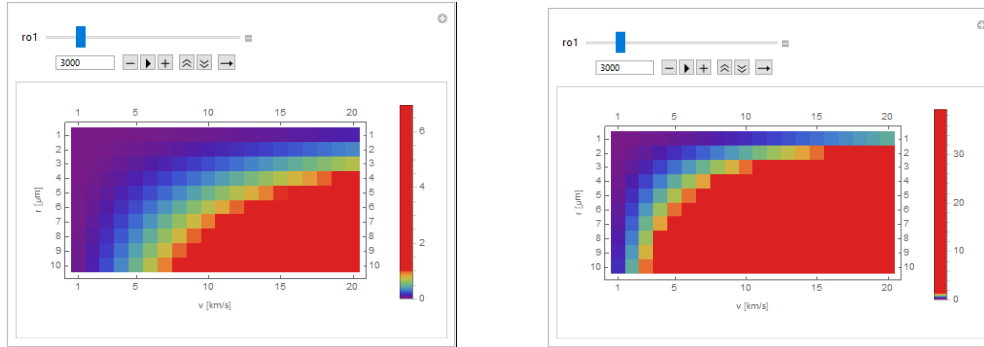


Figure 5.3: Sensitivity depending on the diameter of the piezo. On the left $D = 80mm$. On the right $D = 22mm$ ²

The conclusion here is that both thickness and diameter have an influence on the sensitivity, which increases with a lower thickness and a smaller diameter. However, combining the size with suitable material properties could lead into a good design, and a sufficient sensitivity for satisfy the requirements. Moreover, the desired piezo sensor would be a disc with the dimensions of the target plate ($D = 90mm$) in order to define the 3 components of the velocity of the incoming particles. Avoiding many piezo sensors in an array configuration is desirable as less electronic components will be needed and the wiring will not interfere with the impact of the particles. Besides, the total cost of the piezo configuration is reduced while using less piezo sensors.

5.3 Sensitivity vs Density of Particles

In the first chapter the environment in the LEO was described and what kind of particles were more likely to be found. All the studies done in this chapter were taking into account a density of $8 g/cm^3$ but if an average density of the particles of $3 g/cm^3$ is set, this sensitivity is clearly reduced, as the mass of the particles will be also reduced considerably.

For this reason, there is a combination of size and velocity of the particles that the piezo will not be able to measure. Here is where the electronic components play the most important role. The current requirement is that the minimum output voltage of the piezo is in the order of miliVolts, which afterwards will be amplified and converted to obtain the signal of the impact. Improving the design of the electronics could lead into lower restrictions for the piezo sensor, but there is still a compromise between costs, time and minimum sensitivity required.

In the market it is difficult to find one that fulfills all the requirements and suits the current design, and at the same time does not exceed the costs of production. Appart from the mechanical behaviour of the sensor, after the impact it is required that the particles are ionised. In previous missions, the target plates were made of tungsten or gold, but incorporating a piezo sensor in the surface of the plate could make that the particles are not ionised.

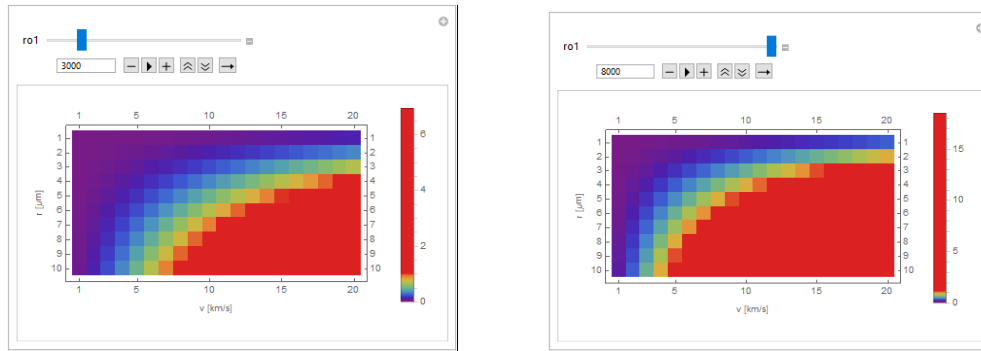


Figure 5.4: Sensitivity depending on the density of the particles. On the left $\rho = 3g/cm^3$. On the right $\rho = 8g/cm^3$

After thinking about different configurations and asking some companies which work with this kind of sensors, there is a possibility of making the electrodes of gold. That would mean that the particles that impact the piezo will give a voltage output value related to their mass and velocity, and at the same time will be ionised to be accelerated towards the acceleration grid and arriving to the TOF ion detector. The disadvantage is the big increase of the cost of the component, and the loss of sensitivity due to the changes in the material³.

5.4 Superposition of Signals

The study and interpretation of the signal of the output Voltage versus the time is the main goal to assure a good design or choice of the component and it is important to know the limitations of this signal. Avoiding the superposition of signals due to two consecutive particle impacts is crucial and minimizing the time of establishment of the signal will minimize this superposition effect.

In the chapter 3.2.11 the piezoelectric properties have been explained and here the frequency of resonance plays an important role. The establishment time of the signal is approximately one third of the resonant frequency of the piezo sensor [7]. For this reason, to avoid the overlapping a value not too big for this parameter it is required. In the current status of the thesis, the manufacturer is yet to determine the shift of this value due to the use of gold electrodes and the customized design proposed. Taking into account all the studies, the definition of the possible treshold to be measured can be limited as shown in the following picture.

The choice has to take into account the temperature influence on the piezo sensor, and how its sensitivity is modified with bigger or lower temperatures. For the study done in this chapter, the sensitivity of the PIC 155 was much better than the one of the PIC 300 but looking to the temperature stability coefficient, the PIC 155 is more likely to face a loss of sensitivity with the increase of the temperatures. However, a big increase in temperatures is not expected in the dust sensor, taking into account the first approximation done by the thermal analysis of the sensor⁴. Therefore, the PZT PIC 155 was chosen as a potential Piezo sensor for the dust sensor.

³Regarding information from engineers in PI Ceramic

⁴Study started on November of 2018

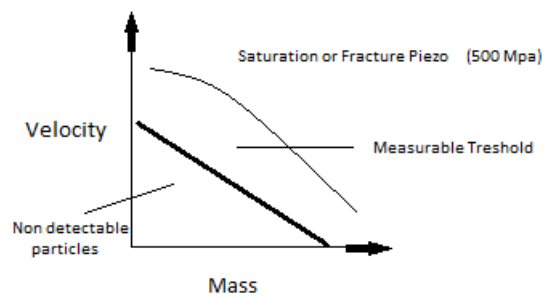


Figure 5.5: Mass and Velocity tresholds to be measured by the sensor.

6

Total Costs and Selection Criteria

One of the main interests in space missions is to reduce the weight of the components as much as possible and therefore the costs. During the development of the project, the materials and dimensions were chosen trying to accomplish this optimization but respecting the requirements. Although the present work focuses on a laboratory model, the requirements of weight and size were considered and the following table summarizes the total costs of its production and the weight of the whole sensor.¹

The "decision making" criteria to choose the different components is based on various factors as mentioned in previous chapters. Some companies gave their quotations after some changes that needed to be made in certain components. Producing the majority of the components in the Workshop of the University will allow to save up to a 20% in manufacturing these components³, with the quotation given by the *Gemmel Metalle Company*. In the first steps of the decision making, the efforts were focused especially on searching properties and designs of the components to assure the good performance of the ion detector. In the table, the potential components to be chosen are summarized. However, after some iterations, changes on the assembly of the components needed to be made, or new ion detectors had to be considered.

In the following table, some features of different MCPs, electron multipliers and channeltrons are analysed to be able to decide which one could fit better the design.

The flexibility that *Hamamatsu* offered on changing their assembly to the dimension's requirements of the structure was the key point to choose one of its components, as continuous changes were required doing the development of the thesis. Another potential component to be included in the sensor was the *Channeltron* from *Photonis Company* but a custom design for the assembly would increase considerably the costs and this option was then dismissed.

At this point, the *Hamamatsu Company* offered electron multipliers and micro channel plates. Comparing the features of some MCPs and Electronmultipliers, it was observed that the average

¹Taking into account that the minimum order of PVC is a plate of $2m \times 1m$

³Although the biggest expense comes from the ion detector.

Table 6.1: Table of prices and weight of the components of the project.

Components	Estimated Price	Number	Total Price (Euros)	Weight (Kg)
Housing Laminates	4.76	4	19.04	0.38
L Section Modular (Short)	2.23	4	8.93	0.06
L Section Modular (Long)	2.23	4	8.93	0.16
Supports (Study Separation)	4.46	2	8.93	0.016
Grid Frames (Squared)	70	6	420	0.024
Acceleration Grid Frames	70	2	140	0.012
PVC Attachments (0°)	*	12	*	0.0032
PVC Attachments (10°)	*	12	*	0.0034
Attachment Ion Detector	*	2	*	0.004
Electron Multiplier (R8811)	780	1	780	0.036
MCP	**	1	**	0.025
Cylindrical Housing	30.95	1	30.95	0.287
Modular Structure	18.39	1	18.39	0.025
Insulators	*	4	*	0.032
Housing Piezo	4.76	1	4.76	0.027
Piezo Sensor	120	1	120	0.081
Target Plate	4.76	1	4.76	0.075
Squared Grids	-	3	-	0.006
Acceleration Grid	-	1	-	0.002
Screws		48		0.009
TOTAL SUM			979.5 ²	1.092/1.103

Table 6.2: Potential Ion detectors and characteristics(1).

Name/Part Number	Company	Mountin Size H/W/T (mm)	Active Area (mm)	OAR(%)	Bias Angle (°)
F4655	Hamamatsu	D = 35	D = 18	60	12
F1551-21s	Hamamatsu	D = 27	D = 14.5	60	12
MCP 3410	Greyhawk Optics	D = 34	D = 30	62	5
MCP-MA 25/2	Greyhawk Optics	34/34/2	D = 25	62	6
Dual MCP C-701/25	JORDAN	D = 25	D = 18	80	5
R8811 E.Multiplier	Hamamtsu	22/20/20	D = 5	-	-
MCP 32516PS	Photonis	D = 40	D = 20	65	8

Table 6.3: Potential Ion detectors and characteristics(1).

Name/Part Number	Gain	Dark Current (pA/cm ²)	Operating Voltage (kV)	Operatig Pressure (Torr)	Price (Euros)
F4655	10 ⁴	0.5	2.5	10 ⁻⁶	2455
F1551-21s	10 ⁴	0.5	2	10 ⁻⁶	3040
MCP 3410	10 ³	0.05	1	10 ⁻⁶	2500
MCP-MA 25/2	10 ³	-	1	10 ⁻⁷	3230
Dual MCP C-701/25	10 ³	-	1	10 ⁻⁶	4000
R8811 E.Multiplier	10 ⁵	-	1.5	10 ⁻⁶	770
MCP 32516PS	10 ³ -10 ⁴	-	2.4	10 ⁻⁵	3800

field of view for the incident particles was between a 2% and 3%⁴ better for the MCP fruit of its small thickness; besides the detection area was 15 mm bigger than the one of the Electron Multiplier. However, the price of the MCP was 5 times bigger and that would increase the costs too much. Further companies had to be analysed to try to find better prices but either the prices were even bigger or the size limitations were not enough.

One possible solution to minimize the cost of the MCP would be to buy a base MCP without the housing assembly and design the assembly structure. However, two problems appeared. The first one was that due to the size of the component, the workshop would not be able to manufacture this pieces and the costs would not change too much. The second one, from the experience of the Hamamatsu Company, the sensitivity of the component can be lowered if some considerations are not taken into account while designing this kind of housing. Therefore, the options available at that point were reduced to the electron multiplier R8811, the MCP F4655 and the MCP F1551-21S.

Comparing both MCPs, the F4655 is cheaper than the F155-21S and the advantage lies on the possibility to demount the component in case the base MCP is damaged and just by buying a base MCP and replacing it, the component will remain functional. Besides, the F1151-21S version has some leads that occupy 30 mm and that would mean having to reduce the time of flight distance, or in other words, reduce the mass resolution. For this reason, the F1551-21S was discarded. Now the decision lied on choosing the electron multiplier or the MCP. Another parameter was taken into account: the minimum operation pressured required. In the Low Earth Orbit (LEO) the atmospheric pressure is about $7.5 \cdot 10^{-11} Torr$ ⁵, while the minimum operating pressure for both components is 10^{-6} Torr, and the performance of them regarding this parameter will be satisfied. Nevertheless, in the laboratory, this conditions must be achieved. The more strict the pressure conditions are, the more complex and expensive the vacuum system becomes. As both components operate at the same pressure, this factor is not decisive while deciding between these two components.⁶

Finally, the CAD design was made for the electron multiplier R8811 as the cost compared to the

⁴While comparing the smallest designs

⁵ $10^{-8} Pa$. Value obtained from Wikipedia

⁶In case there is a need to develop the vacuum system, the use of the channeltron should be considered.

MCPs was 4 time lower. The data sheet specified by Hamamatsu can be found in the Appendix of this document.

Speaking about the piezo sensor, *PI Ceramics* offers the production of the component with a minimum order of 500*Euros*. However, it is the best option to fit the current design. The tests to be done in the laboratory will determine if the configuration designed will give an accurate value of the trajectory of the particles. The following steps will be trying to manufacture a parabolic acceleration grid as the one in the Cassini Mission, as well as a parabolic piezo sensor with gold electrodes to assure that the positive ions are focused into the ion detector.

All in all, with the choice of the R8811 electron multiplier from Hamamatsu, the total costs of the laboratory model would be reduced to:

TOTAL PRICE: 980 *Euros*

7

Conclusions

During the development of this project a deep understanding in the performance of a dust sensor and its components was accomplished. With research on the topic, some examples used in sounded missions were analyzed and some ideas were extracted for the FACIS model. After some iterations, a possible modular design was achieved to satisfy the requirements of the starting point. I learned to cope with a software like CATIA and its different modules by creating all the required components and assembly all together.

As the project was progressing new challenges were faced and problems to solve were encountered, from wich the following conclusions can be extracted:

- The average number of impacts during the FACISS mission is expected to be reduced. Therefore, parameters such as the transmissivity of the grids or the field of view should be optimized, especially regarding the small dimensions of the sensor.
- From the CAD design, it is not only important to assure the theoretical functioning of the different components, but also the production and further assembly of them. Being able to produce the different components in the University Workshop will reduce the costs more than a 20%¹
- From the research of the Piezo sensor, including gold electrodes in the design could be the solution to keep a sufficient sensitivity of the piezo and at the same time assure the ionisation of the particles. Having limited possibilities regarding companies that work with this kind of components, the best option was found with *PI ceramics* as a compromise between costs and size limitations. The main disadvantage is the minimum order of 500*Euros*, although taking into account that part of the surface will be affected after the impact, about 4 piezo sensors will be required to run all the laboratory tests and assure the accurate callibration.
- From the study of sensitivity, given the different options analysed, the most sensitive piezo would be the PIC155. This sensitivity would set the frame of impact velocities

¹Comparing with the quotation given by different companies.

and sizes that can be detected by the sensor. As a first estimation, for an average density of $\rho = 3g/cm^3$ and given the current electronic components status, the threshold of velocities and masses to be measured can be deduced.

- From the study of the field of view, the maximum angle of incidence of the particles is computed, as well as the probability of detection given a random distribution of them. For the current design, the maximum angle is 41 deg in both directions. A 3D spacial analysis of the probability of detection was developed depending on the size and geometry of the obstacles interfering with the free path towards the plate. It was a useful tool to compare different ion detectors and can be used in new iterations by just changing the values of the geometry of the sensor.

It helped to desestimate some ion detectors with this tool, although other considerations had to be taken into account to choose this element, such as the efficiency of detection area, which was bigger for chaneltrons and microchannel plates than for electron multipliers. Finally, the compromise between thickness of the R8811 Multiplier from Hamamatsu and costs were the decisive factors to choose this component.

- From the incorporation of the piezo sensor, the whole trajectory of the particle could be obtained by measuring the energy of impact and obtaining the module of the velocity. The tilted grids will measure two components of the velocity and the mass of the particle analysing the induced charge. With a correct callibration of the measurements, a proximate result can be obtained tightening the limits from previous dust sensors.
- The final design is a modular structure that includes 21 different components and weights 1.2 kg². The advantages from the design are the ease of assembly and demounting the structure to do tests in the laboratory. The drawback from the design is the difficulty of focusing the ions into the ion detector, as a conved piezo sensor would be required.

On the other side, due to the iterative process that results from designing this kind of components, the objective of manufacturing the dust sensor model has not been acomplished. The final design was finally obtained in the last month of the thesis, and the time delivery for some components is expected to last a couple of months.

A FEM analysis was proposed at the begining of the thesis as a potential task, but with the decision of focusing in a laboratory model, this study was left to further developments as no loads are going to be applied in the laboratory measurements.

The size dimensions make more difficult to find potential solutions for the sensor. However, minimizing the costs of those components that can be manufactured in the University makes up for the price increase of the rest of the components.

²Without the electronic components

8

Future Lines of Investigation

The current status of the thesis leaves open possibilities to keep studying the development of the dust sensor. Futures lines of investigation are mentioned in this section that could be useful to take into account in further research projects. As a suggestion, the following ones are described:

- Study of the **electronic components**: Analyse which amplifiers could suit our model or design new ones that assure the functioning of the sensor is crucial to follow with next steps. Additional wires will modify the capacitance of the components leading to worse sensitivities. Therefore, a compromise must be found.
- **Assembly and calibration** of the components in the particle accelerator of the University with low dispersion of the measurements. Establish a sufficient distance between the grids, to compute the mass of the particles accurately to have a good sensitivity of the trajectory and velocity of the particles. Test the impact of the particles on the piezo sensor and check its limitations. Analyse the particle composition delving into the mass spectrometry theory.
- Placement of the **electronic box**: Further designs will depend on the placement of this structure, that will also have an effect on the thermal analysis of the whole sensor. Currently, a thermal modeling is being done by another student and as a first simulation the maximum temperatures for the worst case scenario will not rise the 50. That means that the sensitivity of the chosen components will not perish significantly, but big changes in this value will have to be considered.
- Go through new **design iterations** and find companies that are capable of **manufacturing** the components optimizing the costs and time delivery if required. As an example, the next picture shows how further iterations could be run: Including bending target plates and acceleration grids, spherical piezo sensors to focus the ions into the ion detector to optimize the effectiveness of detection. On the other hand, the use of ceramics instead of PVC to isolate the components could withstand better the thermal loads. Defining a frame of ceramic insulators for each grid will avoid the deposition of the particle in the piezo sensor as a result of impacts in the inner side of the piezo, and leaving this component free from these events would keep its sensitivity.

- Analyse the **attachment** of the sensor to the satellite
- Finally a **structural analysis** is required by a FEM simulation to check if the components withstand the loads during launching (critical case) and find a suitable solution.

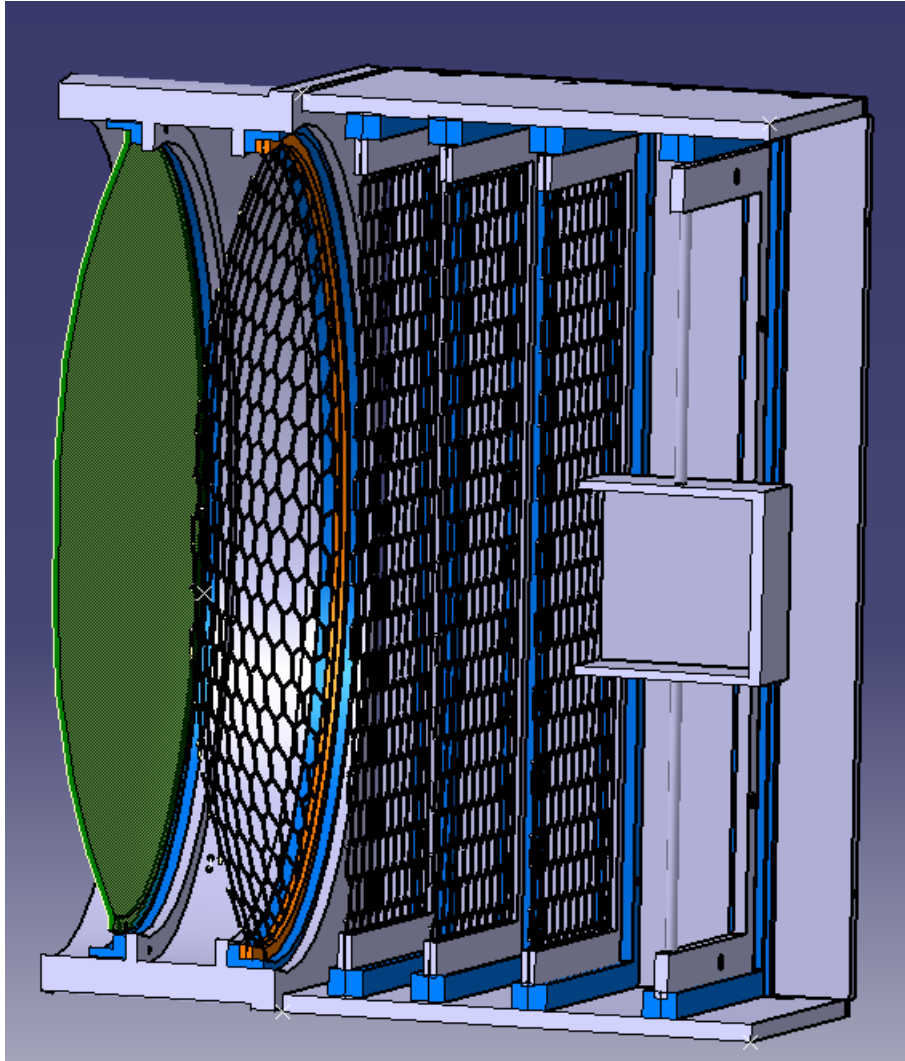


Figure 8.1: Future Possible iteration of the CAD design

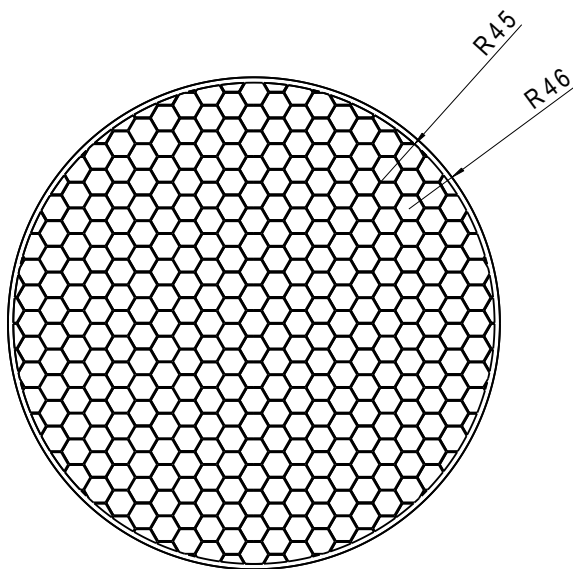
The whole design consists on an iterative process that requires continuous changes that may affect the studies made so far. These lines of investigation could set the starting point for student's thesis to help develop the satellite and get to know more about such an interesting field.

Bibliography

- [1] PIEZOTITE. *Piezoelectric Ceramic Sensors*, catalog no.p19e-6 edition.
- [2] Daniel Monje Centeno. Conceptos electronicos en la medida de la aceleracion y la vibracion. Master's thesis, Universidad Politecnica de Sevilla, 09/09/2010.
- [3] Physical basis. the piezoelectric effect in ceramic materials.
- [4] AMara Graps Sascha Kempf, Ralf Srama. The cosmic dust analyser data handbook, jul 2012.
- [5] A. de Rooij. Corrosion in space.
- [6] Uns c17200 beryllium copper alloys.
- [7] Pi piezo technology.
- [8] About ion feedback of micro channel plates (mcp).
- [9] Universidad de Alicante. Espectrometria de masas.
- [10] Grupo solitium repro 3d.
- [11] Ben Martinsen Jimmy Schmoke Mike Cook Jorge Carmona Reyes Truell Hyde Frank Odom III, Grant Richter. Piezo dust detector. *Casper Revu*, aug 2014.
- [12] Inderjit Chopra Jayant Sirohi. Fundamental understanding of piezoelectric strain sensors. *JOURNAL OF INTELLIGENT MATERIALSYSTEMS AND STRUCTURES*, 11:246–257, apr 200.
- [13] G.Jyoti J.L Beauchamp Thomas J. Ahrens, Satish C. Gupta. Mass spectrometer calibration of cosmic dust analyzer, jgr plantes. *AGU100 Advancing Earth and Space Science*, 108, feb 2003. <https://agupubs.onlinelibrary.wiley.com/doi/full/10.1029/2002JE001912>.
- [14] Daniel E. Austin. Impact ionization mass spectrometry of cosmic dust. Master's thesis, California Institute of Technology, 2003.
- [15] Harley H.Cudney NASA Daniel J Inman. Structural and machine design using piezo-ceramic materials.
- [16] William G. Dunn Reginald Farr Bruce N. Laprade, Lenny Erickson. The development of miniature electron multipliers for use in portable mass spectrometers. Paper 10400-2100, Burle Electro-Optics, mar 2004. <https://www.photonis.com/uploads/literature/library/MiniatureElectronMultipliers-Pittcon2004.pdf>.
- [17] Del Mar Photonics. Micro channel plates.
- [18] Miyachi T. Hattori M. Kobayashi, M. Dust detector using pieszoelectric lead zirconate titanate with current-to-voltage converting amplifier for functional advancement. *Earth, Planets and Science*, mar 2003. <https://link.springer.com/article/10.5047>
- [19] Website sandvik milling tools.

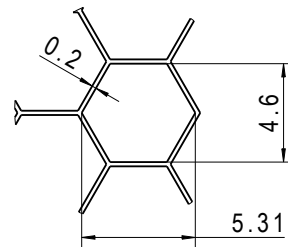
- [20] Hamamatsu Company. Mcp (microchannel plate) and mcp assembly.
- [21] Gemmel Metalle Company. Website.
- [22] AlcoTec Company. Understanding the alloys of aluminium.
- [23] Continental Steel and Tube Company. Aluminium in the aerospace industry.
- [24] R.Srama S.Kempf R.Auer S. Auer, E.Gr \tilde{A} $\frac{1}{4}$ n. The charge and velocity detector of the cosmic dust analyzer on cassini. *Planetary and Space Science*, apr 2002.
- [25] Anton Kearsley Mark J. Burchell, Giles Graham. Cosmic dust collection in aerogel. *Annual Reviews of Earth and Planetary Sciences*, 34:385–418, may 2006.
- [26] S. Auer. Cosmic dust and impact ionization mass spectrometry, dec 2003.

APPENDIX A. CAD PLANS



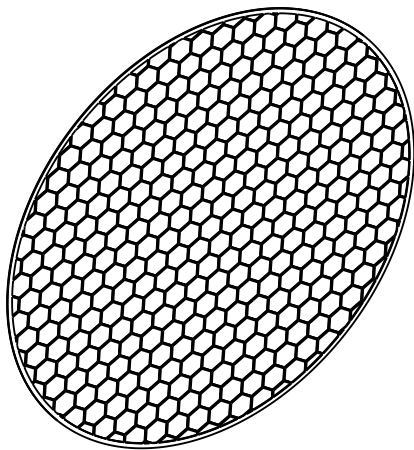
Front view
Scale: 1:1

0.2



Detail A[2]
Scale: 4:1

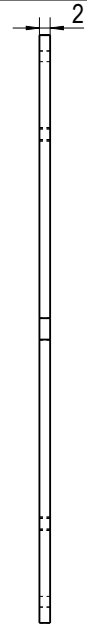
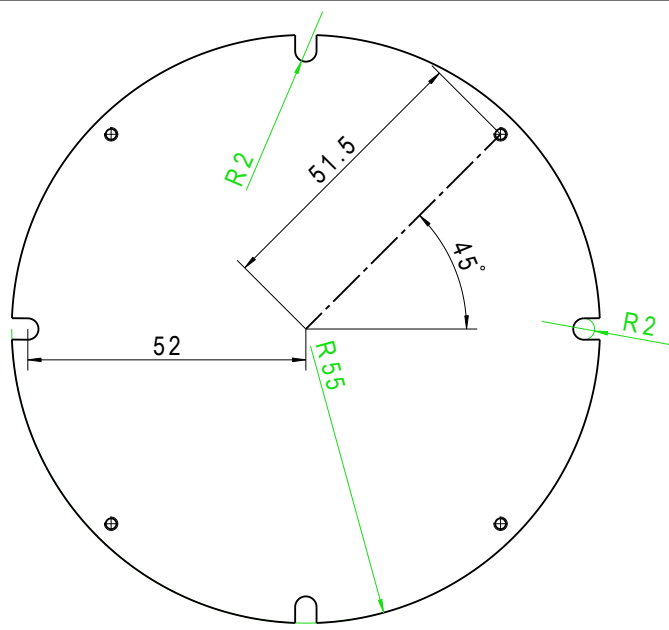
Left view
Scale: 1:1



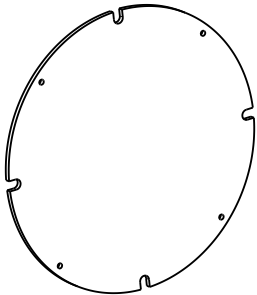
Isometric view

		 DIN 6784	Allgemeintoleranz nach ISO 2768-mK	Format A4	Maßstab 1:1	Masse xx kg
			Datum 11.10.2018	Name Francisco Mansilla	<h2>Acceleration Grid</h2>	
			Bearb.	Gepr.		
			Berechn.	Norm		
Zust.	Änderung	Datum	Name	Norm		
Betreuer: Tel.(Betreuer): Tel.(Zeichner):		Jona Petri Heiko Stack ZZ-ZZ ZZ-ZZ		Institut für Raumfahrtssysteme		
Zeichnungsnummer: XXX-ZZ-MMSSS-BBB-DD-RR					Blatt	
Zeichnungsdatei: Spectrometer_Option_2.CATDrawing					Bl.	
Ers. für:						

Front view
Scale: 1:1

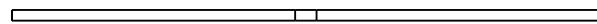


Left view
Scale: 1:1



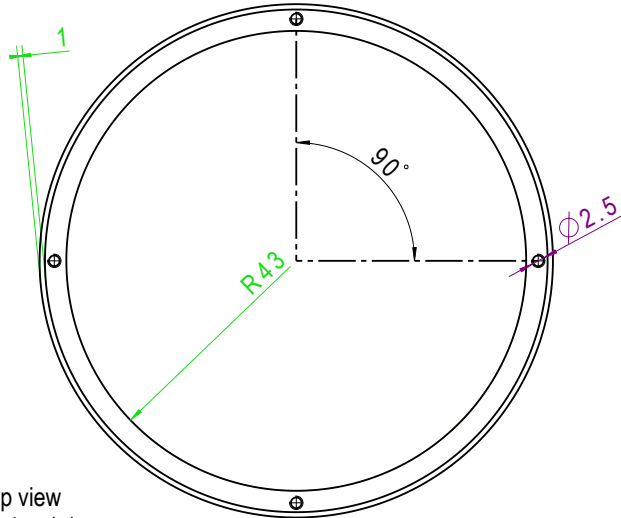
Isometric view
Scale: 1:2

Top view
Scale: 1:1

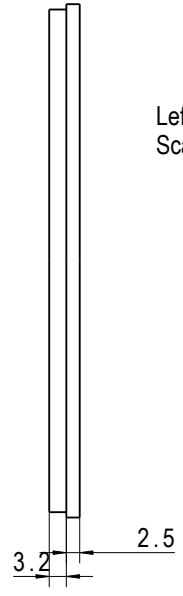


		$\begin{matrix} +0.3 & -0.2 \\ +0.1 & -0.4 \end{matrix}$ DIN 6784	Allgemeintoleranz nach ISO 2768-mK	Format A4	Maßstab 1:1	Masse xx kg	
			Datum 11.10.2018	Name Francisco Mansilla	<h2>Bottom Structure</h2>		
			Bearb.	Gepr.			
			Berechn.	Norm			
Zust.	Änderung	Datum	Name	Norm			
Betreuer: Jona Petri Heiko Stack		Institut für Raumfahrtssysteme				Zeichnungsnummer: XXX-ZZ-MMSSS-BBB-DD-RR	Blatt
Tel.(Betreuer): ZZ-ZZ				Zeichnungsdatei: Spectrometer_Option_2.CATDrawing		Bl.	
Tel.(Zeichner): ZZ-ZZ				Ers. für:			

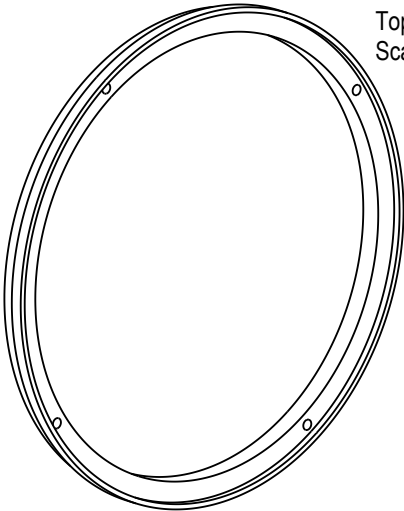
Front view
Scale: 1:1



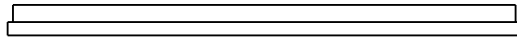
Left view
Scale: 1:1



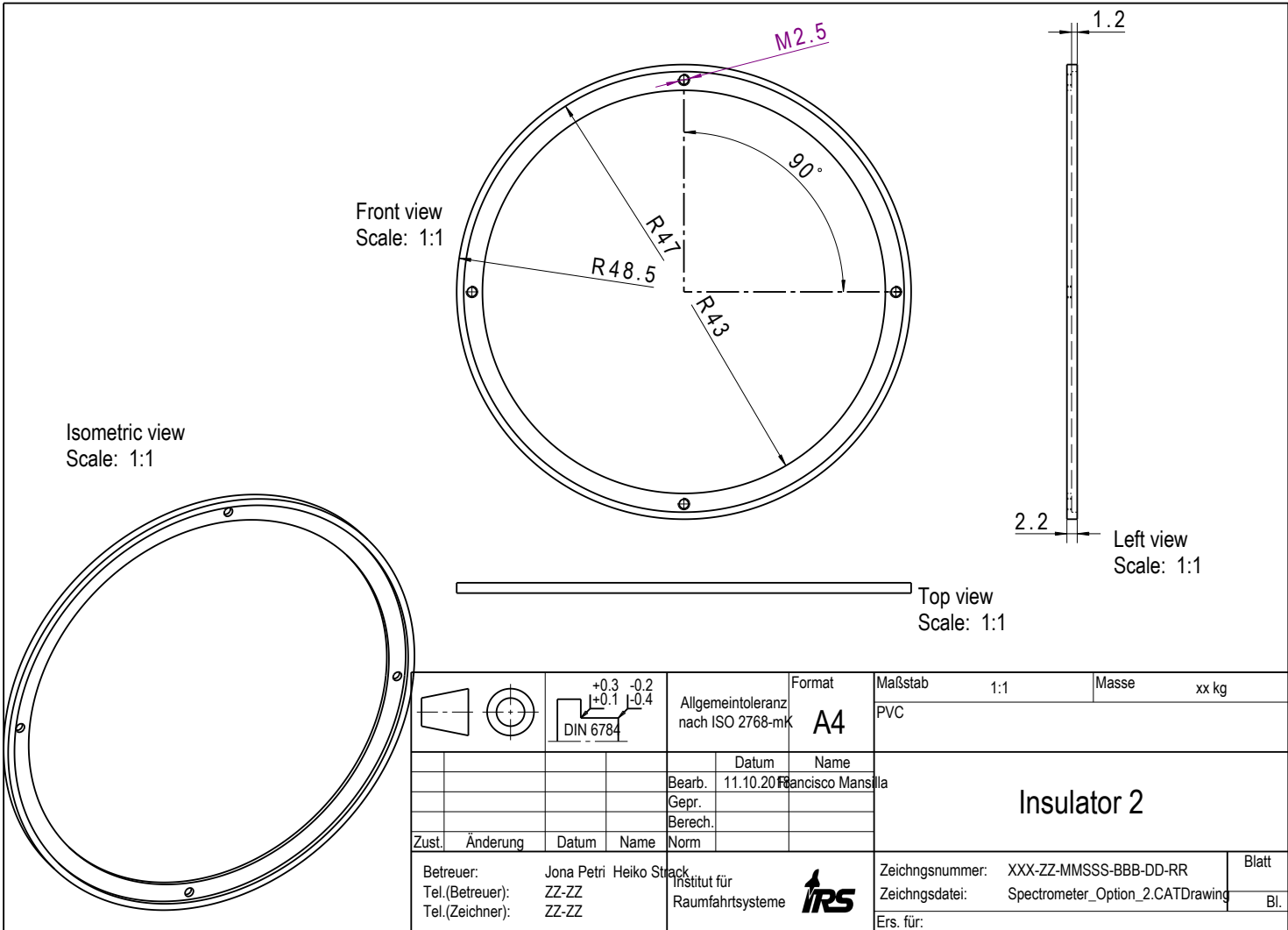
Isometric view
Scale: 1:1



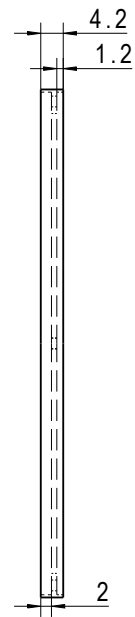
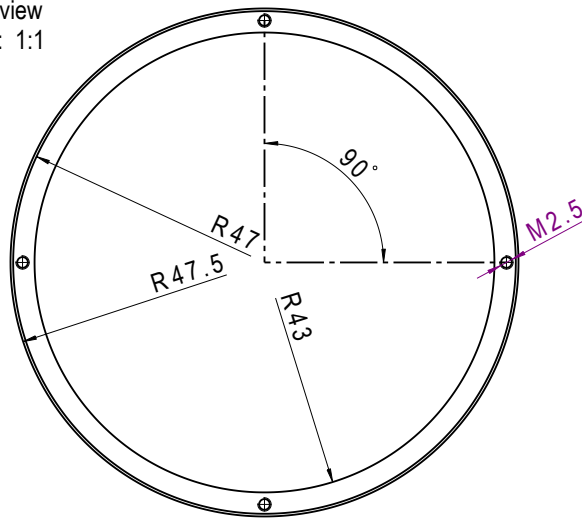
Top view
Scale: 1:1



		$\begin{matrix} +0.3 & -0.2 \\ +0.1 & -0.4 \end{matrix}$ DIN 6784	Allgmeintoleranz nach ISO 2768-mK	Format A4	Maßstab 1:1	Masse xx kg
			Datum 11.10.2018	Name Francisco Mansilla	<h1>Insulator 1</h1>	
			Bearb. Gepr. Berechn.			
Zust.	Änderung	Datum	Name	Norm		
Betreuer: Tel.(Betreuer): Tel.(Zeichner):		Jona Petri Heiko Stack Institut für Raumfahrtssysteme				
						Blatt Bl.

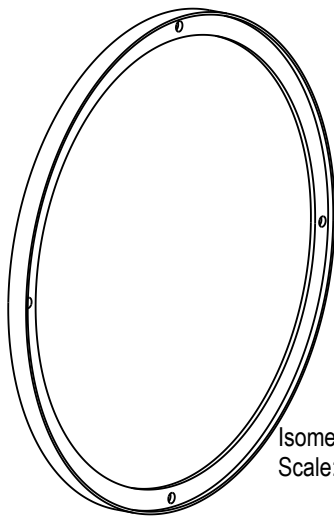
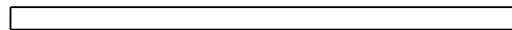


Front view
Scale: 1:1



Left view
Scale: 1:1

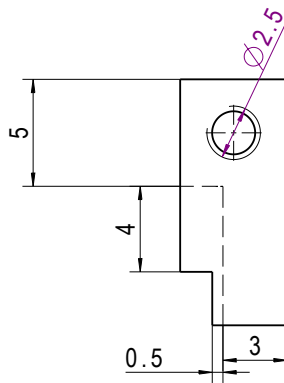
Top view
Scale: 1:1



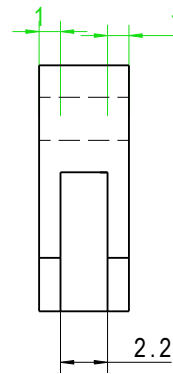
Isometric view
Scale: 1:1

		 DIN 6784	Allgmeintoleranz nach ISO 2768-mK	Format A4	Maßstab 1:1	Masse xx kg
				Datum 11.10.2018	Insulator 3	
				Name Francisco Mansilla		
				Bearb.		
				Gepr.		
				Berechn.		
				Norm		
Zust.	Änderung	Datum	Name			Blatt
Betreuer: Jona Petri Heiko Stack			Institut für Raumfahrtssysteme		Zeichnungsnummer: XXX-ZZ-MMSSS-BBB-DD-RR	Blatt
Tel.(Betreuer): ZZ-ZZ					Zeichnungsdatei: Spectrometer_Option_2.CATDrawing	Bl.
Tel.(Zeichner): ZZ-ZZ					Ers. für:	

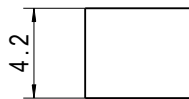
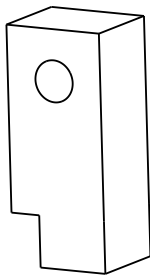
Front view
Scale: 4:1



Left view
Scale: 4:1



Isometric view
Scale: 4:1

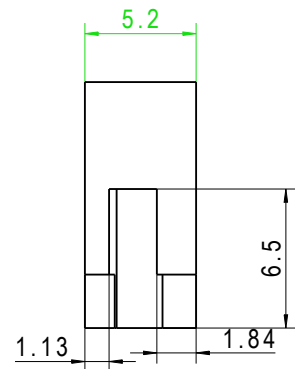
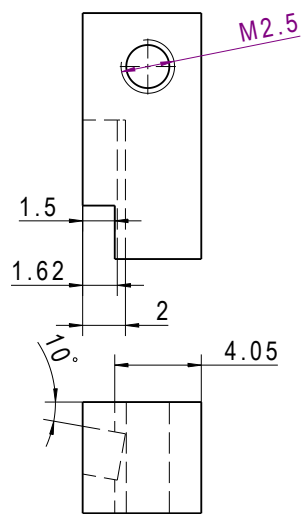


Top view
Scale: 4:1

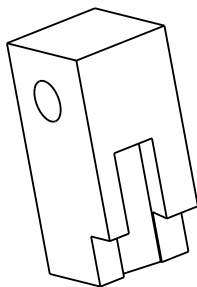
		$+0.3$ $+0.1$ -0.2 -0.4 DIN 6784	Allgemeintoleranz nach ISO 2768-mK	Format A4	Maßstab 1:1	Masse xx kg
			Datum 12.12.2018	Name F.Mansilla	<h2>PVC Attachments</h2>	
			Bearb.	Gepr.		
			Berechn.	Norm		
Zust.	Änderung	Datum	Name	Norm		
Betreuer: XXXXX Tel.(Betreuer): ZZ-ZZ Tel.(Zeichner): ZZ-ZZ			Institut für Raumfahrtssysteme		Zeichnungsnummer: XXX-ZZ-MMSSS-BBB-DD-RR Zeichungsdatei: Drawing2.CATDrawing	Blatt Bl.
Ers. für:						

Front view
Scale: 4:1

Left view
Scale: 4:1



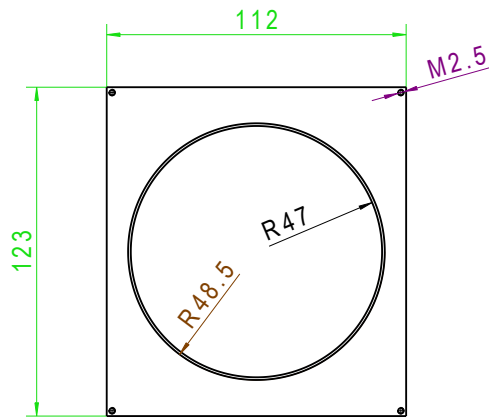
Isometric view
Scale: 4:1



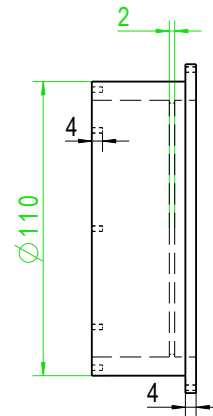
Top view
Scale: 4:1

		$\begin{matrix} +0.3 & -0.2 \\ +0.1 & -0.4 \end{matrix}$ DIN 6784	Allgemeintoleranz nach ISO 2768-mK	Format A4	Maßstab 1:1 Masse xx kg
			Datum 12.12.2018	Name F.Mansilla	<h2>PVC Attachments 10°</h2>
			Bearb.	Gepr.	
			Berechn.	Norm	
Zust.	Änderung	Datum	Name	Norm	
Betreuer: XXXXX Tel.(Betreuer): ZZ-ZZ Tel.(Zeichner): ZZ-ZZ		Institut für Raumfahrtssysteme		Zeichnungsnummer: XXX-ZZ-MMSSS-BBB-DD-RR Zeichungsdatei: Drawing2.CATDrawing	Blatt Bl.
Ers. für:					

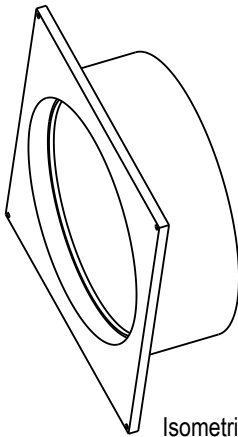
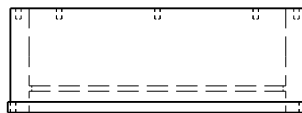
Front view
Scale: 1:2



Left view
Scale: 1:2



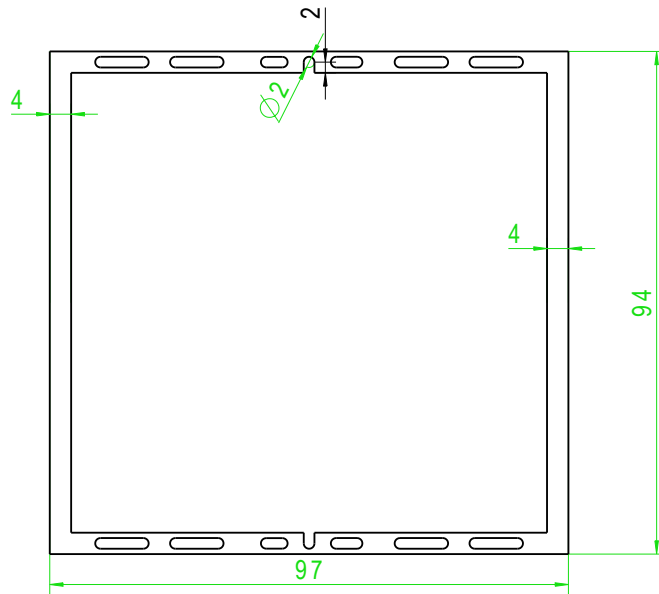
Top view
Scale: 1:2



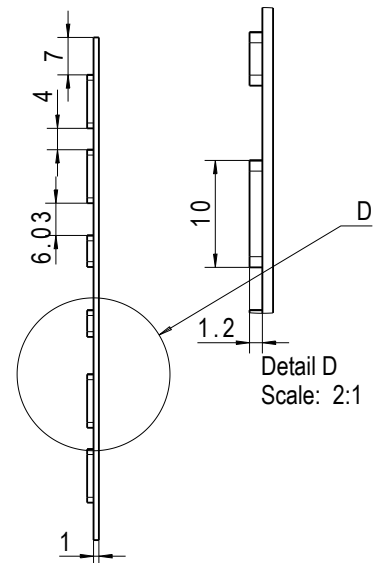
Isometric view
Scale: 1:2

		 $+0.3$ -0.2 $+0.1$ -0.4 DIN 6784	Allgmeintoleranz nach ISO 2768-mK	Format A4	Maßstab 1:1	Masse xx kg
					Aluminium 7075	
				Datum 11.10.2018	Name Francisco Mansilla	<h2>Cylindrical Housing</h2>
				Bearb. Gepr.		
				Berechn. Norm		
Zust.	Änderung	Datum	Name	Norm		
Betreuer: Tel.(Betreuer): Tel.(Zeichner):		Jona Petri Heiko Stack ZZ-ZZ ZZ-ZZ		Institut für Raumfahrtssysteme		Zeichnungsnummer: XXX-ZZ-MMSSS-BBB-DD-RR Zeichnungsdatei: Spectrometer_Option_2.CATDrawing Ers. für:
						Blatt Bl.

Front view
Scale: 1:1

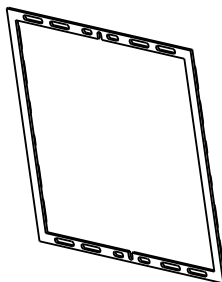


Top view
Scale: 1:1



Left view
Scale: 1:1

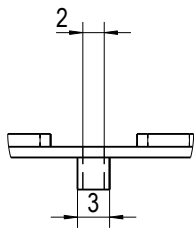
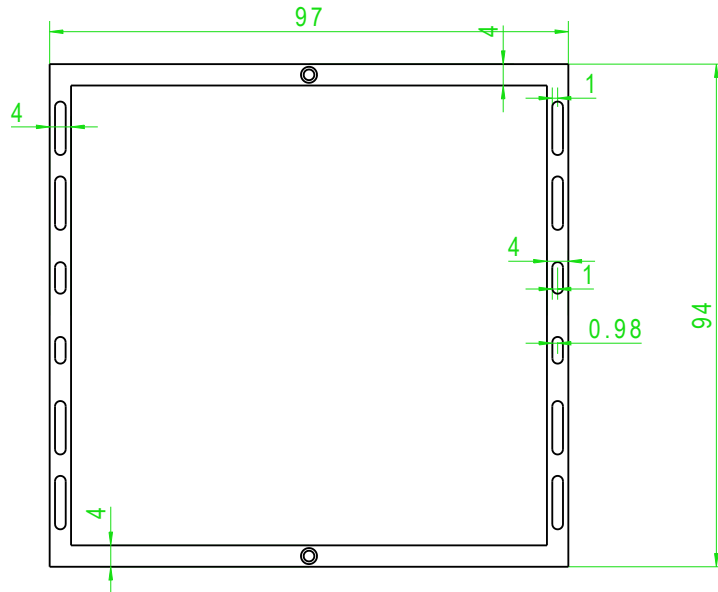
Detail D
Scale: 2:1



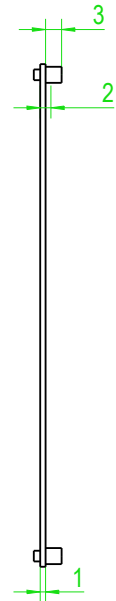
Isometric view
Scale: 1:2

		$\begin{matrix} +0.3 & -0.2 \\ +0.1 & -0.4 \end{matrix}$ DIN 6784	Allgmeintoleranz nach ISO 2768-mK	Format A4	Maßstab 1:1	Masse xx kg
			Datum 12.10.2018	Name F.Mansilla	Frame Structure for grids	
			Bearb.	Gepr.		
			Berechn.	Norm		
Zust.	Änderung	Datum	Name			Zeichnungsnummer: XXX-ZZ-MMSSS-BBB-DD-RR
Betreuer: XXXXX Tel.(Betreuer): ZZ-ZZ Tel.(Zeichner): ZZ-ZZ			Institut für Raumfahrtssysteme		Zeichnungsdatei: Drawing2.CATDrawing	Blatt Bl.
Ers. für:						

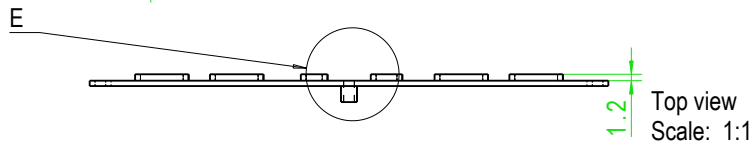
Front view
Scale: 1:1



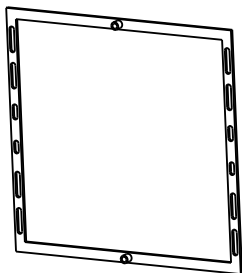
Detail E
Scale: 2:1



Left view
Scale: 1:1



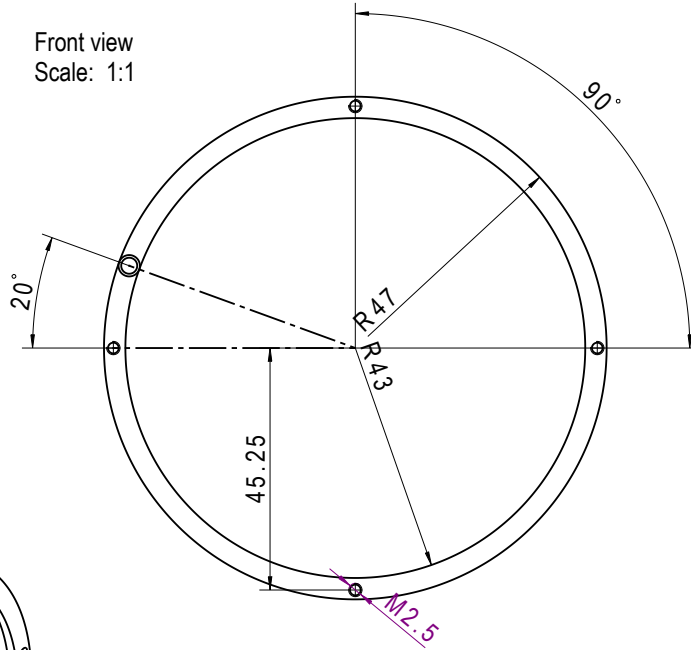
Top view
Scale: 1:1



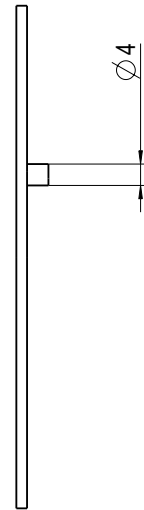
Isometric view
Scale: 1:2

	$\begin{matrix} +0.3 & -0.2 \\ +0.1 & -0.4 \end{matrix}$ DIN 6784	Allgemeintoleranz nach ISO 2768-mK	Format A4	Maßstab 1:1	Masse xx kg
				Aluminium 7075	
			Datum 12.10.2018	Name F.Mansilla	
			Gepr.	<h2 style="text-align: center;">Frame Structure for grids 2</h2>	
			Berechn.		
Zust.	Änderung	Datum	Name	Zeichnungsnummer: XXX-ZZ-MMSSS-BBB-DD-RR	
Betreuer: XXXXX Tel.(Betreuer): ZZ-ZZ Tel.(Zeichner): ZZ-ZZ			Institut für Raumfahrtssysteme	Zeichnungsdatei: Drawing2.CATDrawing	
				Ers. für:	Blatt Bl.

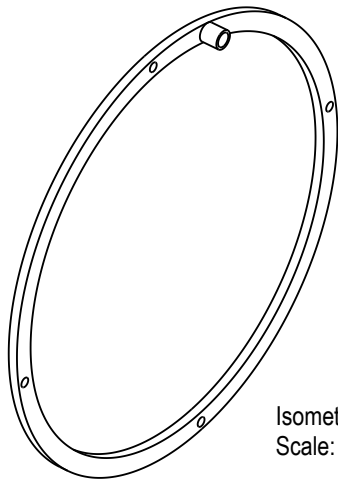
Front view
Scale: 1:1



Left view
Scale: 1:1



Top view
Scale: 1:1

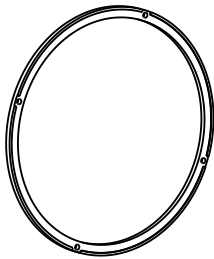
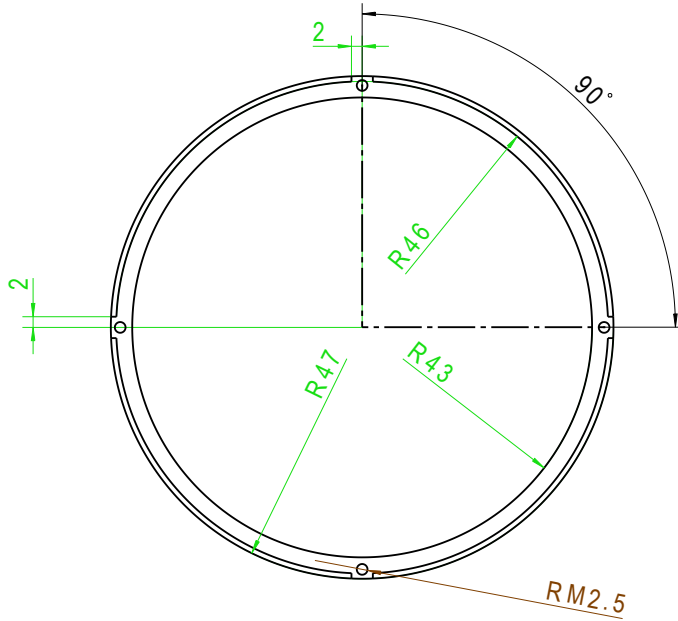


Isometric view
Scale: 1:1

		$\begin{matrix} +0.3 & -0.2 \\ +0.1 & -0.4 \end{matrix}$ DIN 6784	Allgemeintoleranz nach ISO 2768-mK	Format A4	Maßstab 1:1	Masse xx kg
			Datum 12.10.2018	Name F.Mansilla	<h2>Frame Structure for grids 2</h2>	
			Bearb.	Gepr.		
			Berechn.	Norm		
Zust.	Änderung	Datum	Name	Norm		
Betreuer: XXXXX Tel.(Betreuer): ZZ-ZZ Tel.(Zeichner): ZZ-ZZ		Institut für Raumfahrtssysteme		Zeichnungsnummer: XXX-ZZ-MMSSS-BBB-DD-RR Zeichnungsdatei: Drawing2.CATDrawing	Blatt Bl.	
Ers. für:						

Front view
Scale: 1:1

Left view
Scale: 1:1

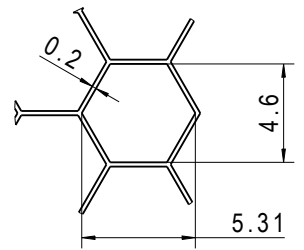
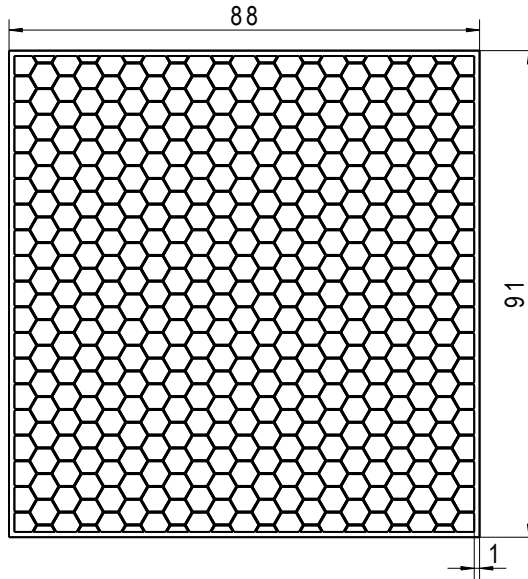


Isometric view
Scale: 1:2

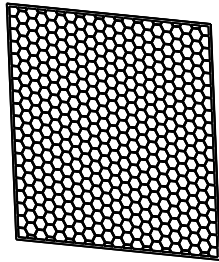
Top view
Scale: 1:1

			Allgemeintoleranz nach ISO 2768-mK	Format A4	Maßstab 1:1	Masse xx kg
			Datum 12.10.2018	Name F.Mansilla	<h2>Frame Structure for grids 2</h2>	
			Bearb.	Gepr.		
			Berechn.	Norm		
Zust.	Änderung	Datum	Name	Norm		
Betreuer: XXXXX Tel.(Betreuer): ZZ-ZZ Tel.(Zeichner): ZZ-ZZ		Institut für Raumfahrtssysteme			Zeichnungsnummer: XXX-ZZ-MMSSS-BBB-DD-RR Zeichnungsdatei: Drawing2.CATDrawing	Blatt Bl.
Ers. für:						

Front view
Scale: 1:1



Detail A
Scale: 4:1

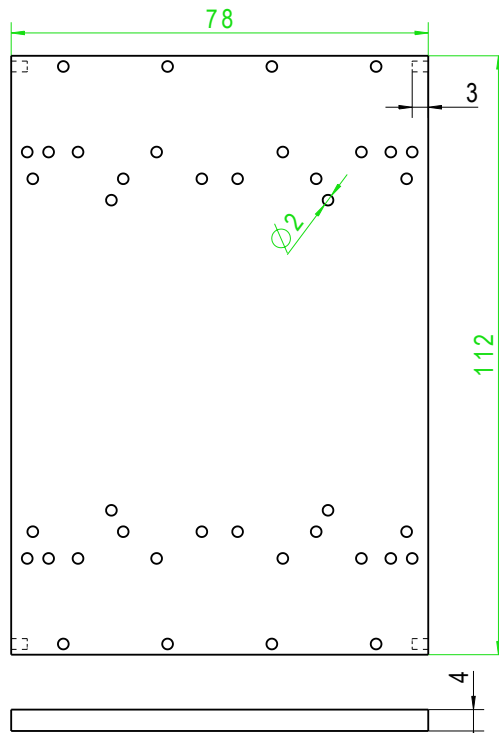


Isometric view
Scale: 1:2

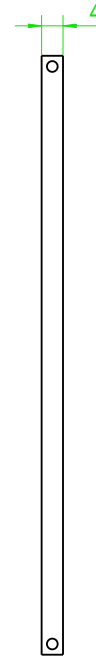
Top view
Scale: 1:1

				DIN 6784	Allgemeintoleranz nach ISO 2768-mK	Format A4	Maßstab 1:1	Masse xx kg
					Datum 12.10.2018	Name F.Mansilla	<h2>Squared Grid</h2>	
					Bearb.			
					Gepr.			
					Berechn.			
Zust.	Änderung	Datum	Name	Norm				
Betreuer: XXXXX Tel.(Betreuer): ZZ-ZZ Tel.(Zeichner): ZZ-ZZ			Institut für Raumfahrtssysteme				Zeichnungsnummer: XXX-ZZ-MMSSS-BBB-DD-RR	Blatt
							Zeichnungsdatei: Drawing2.CATDrawing	Bl.
Ers. für:								

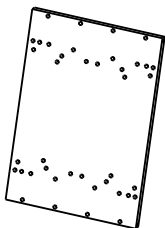
Front view
Scale: 1:1



Top view
Scale: 1:1



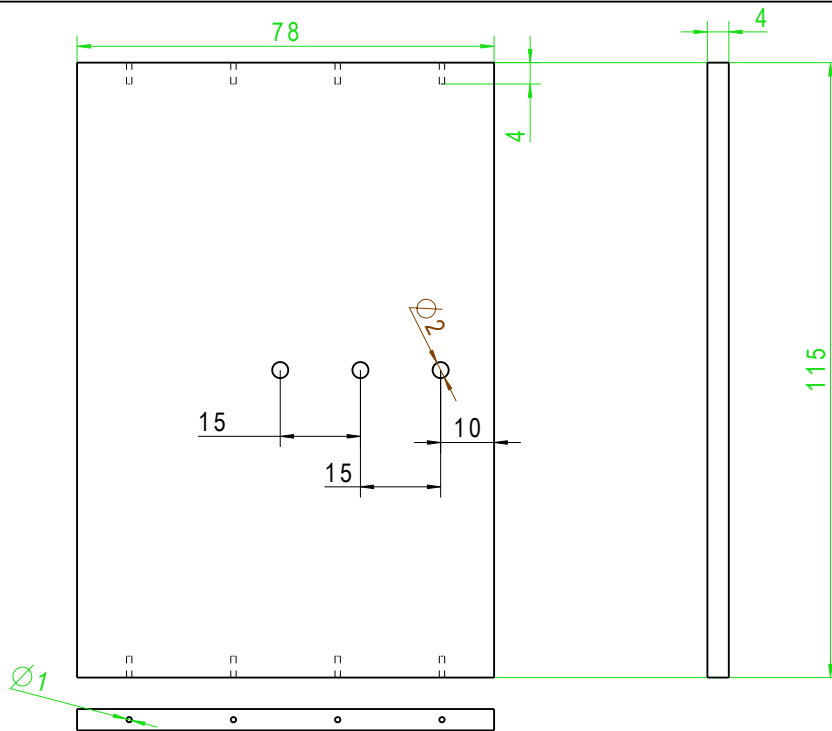
Left view
Scale: 1:1



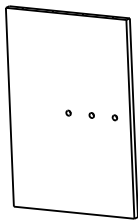
Isometric view
Scale: 1:3

		$\begin{matrix} +0.3 & -0.2 \\ +0.1 & -0.4 \end{matrix}$ DIN 6784	Allgemeintoleranz nach ISO 2768-mK	Format A4	Maßstab 1:1	Masse xx kg
				Datum 12.10.2018	Name F.Mansilla	<h2>Housing Laminate Long</h2>
				Bearb. 12.10.2018	Name F.Mansilla	
				Gepr.		
				Berechn.		
Zust.	Änderung	Datum	Name	Norm		
Betreuer: XXXXX Tel.(Betreuer): ZZ-ZZ Tel.(Zeichner): ZZ-ZZ			Institut für Raumfahrtssysteme		Zeichnungsnummer: XXX-ZZ-MMSSS-BBB-DD-RR	Blatt
					Zeichnungsdatei: Drawing2.CATDrawing	Bl.
Ers. für:						

Front view
Scale: 1:1

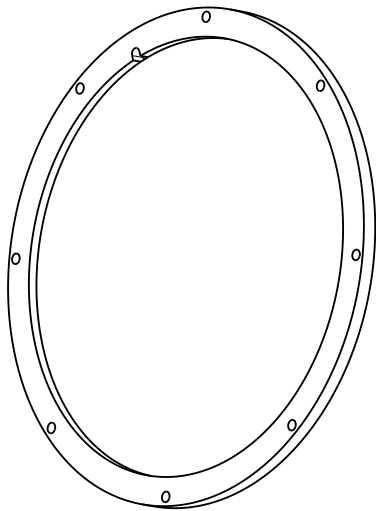


Left view
Scale: 1:1

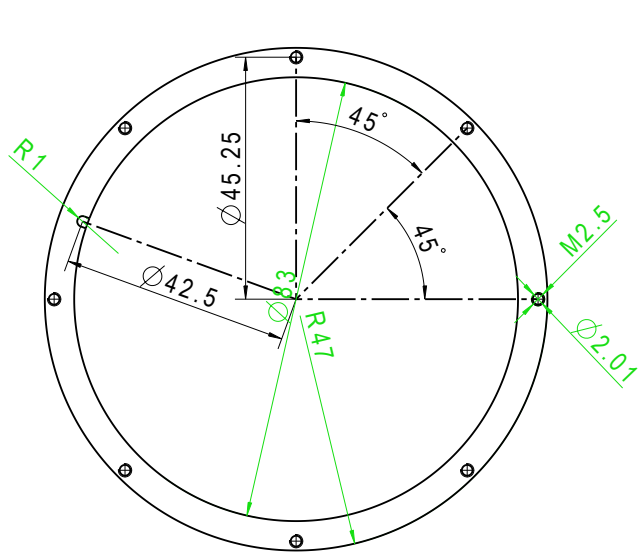


Isometric view
Scale: 1:3

 Top view Scale: 1:1 DIN 6784		0.3 -0.2 1+0.1 -0.4	Format A4	Maßstab 1:1	Masse xx kg
Allgemeintoleranz nach ISO 2768-mK			Aluminium 7075	<h2>Housing Laminate Short</h2>	
		Datum 12.10.2018	Name F.Mansilla		
		Gepr.	Berechn.		
Zust.	Änderung	Datum	Name		
Betreuer: XXXXX Tel.(Betreuer): ZZ-ZZ Tel.(Zeichner): ZZ-ZZ		Institut für Raumfahrtssysteme 		Zeichnungsnummer: XXX-ZZ-MMSSS-BBB-DD-RR Zeichungsdatei: Drawing2.CATDrawing	Blatt Bl.
Ers. für:					

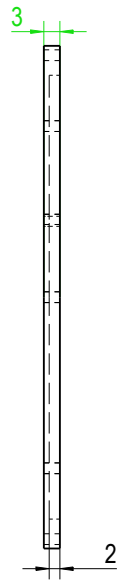


Isometric view
Scale: 1:1



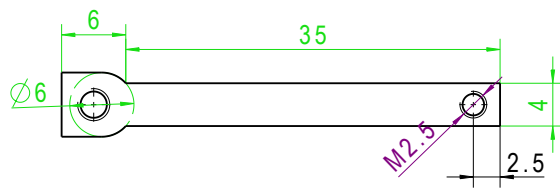
Top view

Scale: 1:1

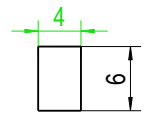


Left view
Scale: 1:1

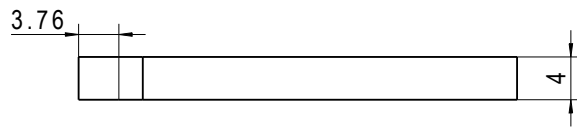
		 DIN 6784	Allgemeintoleranz nach ISO 2768-mK	Format A4	Maßstab 1:1	Masse xx kg
			Datum 11.10.2018	Name Francisco Mansilla	<h2>Piezo Housing</h2>	
			Bearb. Gepr.	Berechnung		
			Zust. Änderung	Datum Name		
			Datum Name	Norm		
Betreuer: Tel.(Betreuer): Tel.(Zeichner):		Jona Petri Heiko Stack ZZ-ZZ ZZ-ZZ		Institut für Raumfahrtssysteme		Zeichnungsnummer: XXX-ZZ-MMSSS-BBB-DD-RR Zeichnungsdatei: Spectrometer_Option_2.CATDrawing Ers. für:
						Blatt Bl.



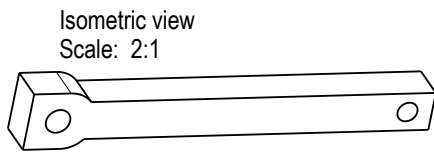
Front view
Scale: 2:1



Left view
Scale: 2:1



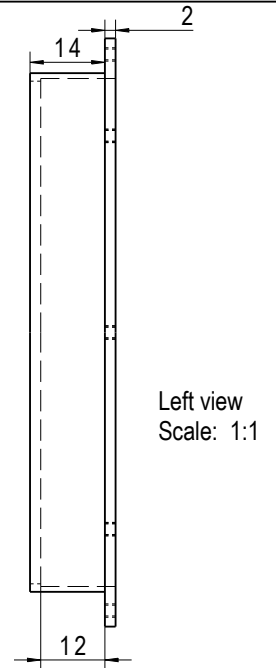
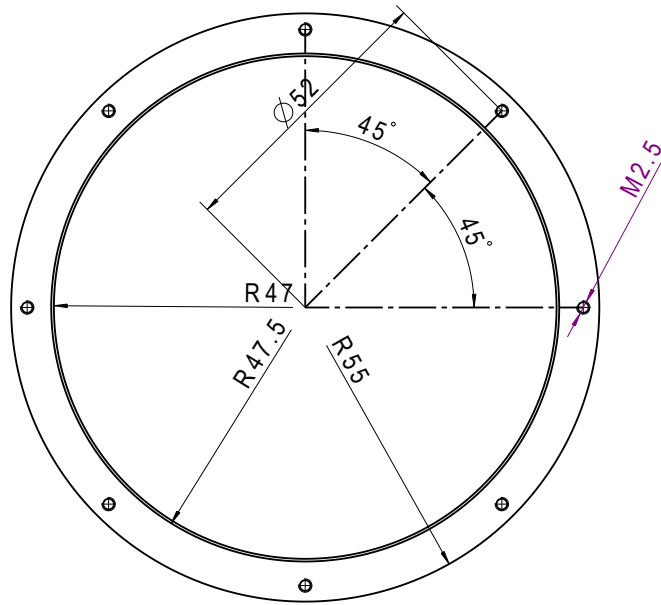
Top view
Scale: 2:1



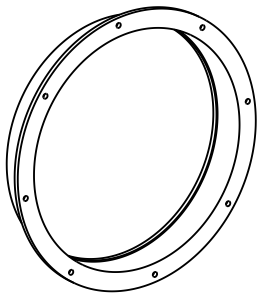
Isometric view
Scale: 2:1

		Allgemeintoleranz nach ISO 2768-mK Format A4		Maßstab 1:1	Masse xx kg
DIN 6784		Datum 12.12.2018 Name F.Mansilla		<h2>Attachment Ion Detector</h2>	
Zust. Änderung Datum Name		Bearb. 12.12.2018 Gepr. Berech.			
Norm		Zeichnungsnummer: XXX-ZZ-MMSSS-BBB-DD-RR Zeichungsdatei: Drawing2.CATDrawing			
Betreuer: XXXXX Tel.(Betreuer): ZZ-ZZ Tel.(Zeichner): ZZ-ZZ		Institut für Raumfahrtssysteme		Blatt Bl.	
Ers. für:					

Front view
Scale: 1:1

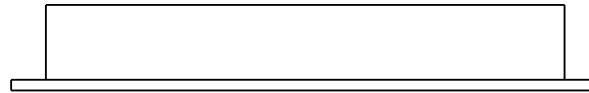


Left view
Scale: 1:1

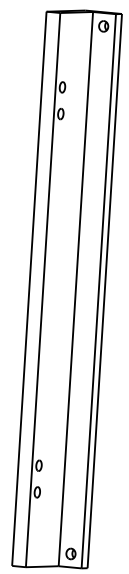
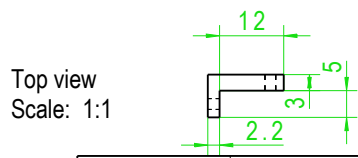
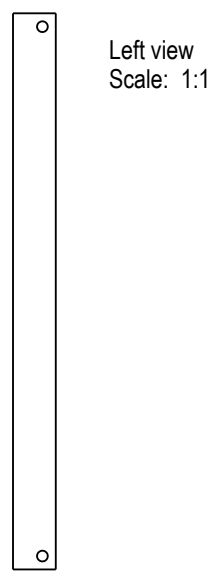
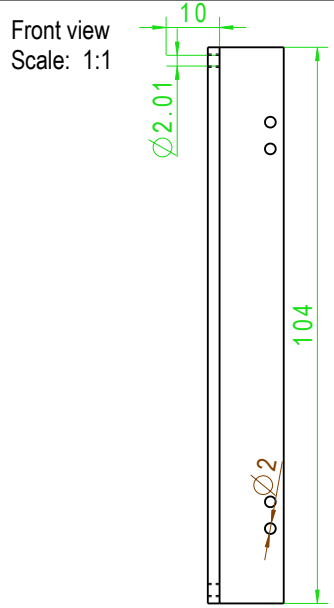


Isometric view
Scale: 1:2

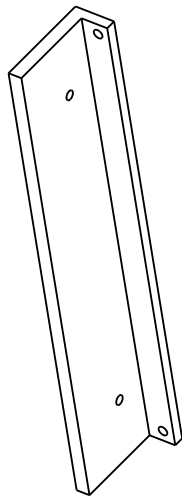
Top view
Scale: 1:1



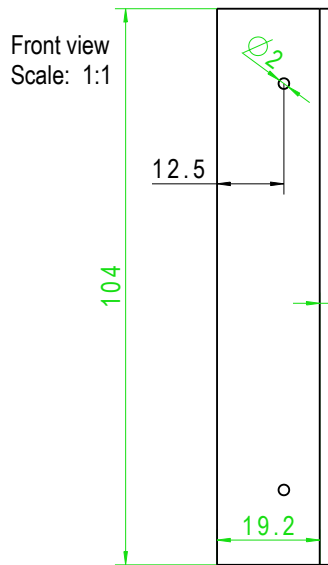
	 $+0.3$ -0.2 $+0.1$ -0.4 DIN 6784	Allgemeintoleranz nach ISO 2768-mK	Format A4	Maßstab 1:1	Masse xx kg
				Aluminium	
			Datum 11.10.2018	<h2>Modular Support</h2>	
			Name Francisco Mansilla		
			Gepr.		
			Berechnung		
Zust. Änderung Datum Name Norm					
Betreuer: Jona Petri Heiko Stack Tel.(Betreuer): ZZ-ZZ Tel.(Zeichner): ZZ-ZZ	Institut für Raumfahrtssysteme		Zeichnungsnummer: XXX-ZZ-MMSSS-BBB-DD-RR Zeichnungsdatei: Spectrometer_Option_2.CATDrawing	Blatt Bl.	
Ers. für:					



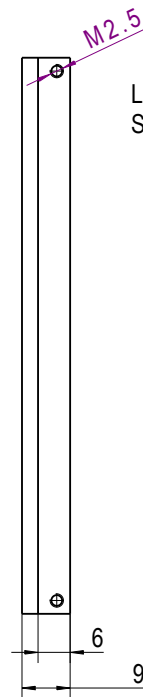
		$\begin{matrix} +0.3 & -0.2 \\ +0.1 & -0.4 \end{matrix}$ DIN 6784	Allgmeintoleranz nach ISO 2768-mK	Format A4	Maßstab 1:1	Masse xx kg
			Datum 12.10.2018	Name F.Mansilla	<h2>Modular L Section</h2>	
			Bearb.	Gepr.		
			Berechn.	Norm		
Zust.	Änderung	Datum	Name			Blatt
Betreuer: XXXXX Tel.(Betreuer): ZZ-ZZ Tel.(Zeichner): ZZ-ZZ			Institut für Raumfahrtssysteme		Zeichnungsnummer: XXX-ZZ-MMSSS-BBB-DD-RR Zeichungsdatei: Drawing2.CATDrawing	Bl.
Ers. für:						



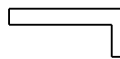
Isometric view
Scale: 1:1



Front view
Scale: 1:1



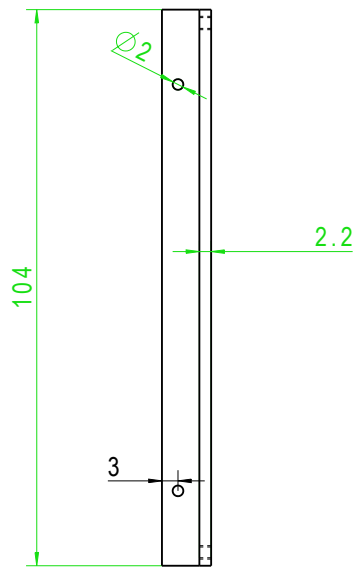
Left view
Scale: 1:1



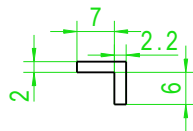
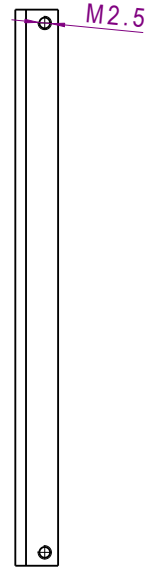
Top view
Scale: 1:1

		$\begin{matrix} +0.3 & -0.2 \\ +0.1 & -0.4 \end{matrix}$ DIN 6784	Allgemeintoleranz nach ISO 2768-mK	Format A4	Maßstab 1:1 Aluminium	Masse xx kg	
				Datum	Name	ModularL3	
			Bearb.	11.10.2018	Francisco Mansilla		
			Gepr.				
			Berech.				
Zust.	Änderung	Datum	Name	Norm			
Betreuer: Jona Petri Heiko Stack Tel.(Betreuer): ZZ-ZZ Tel.(Zeichner): ZZ-ZZ		Institut für Raumfahrtssysteme				Zeichnungsnummer: XXX-ZZ-MMSSS-BBB-DD-RR Zeichnungsdatei: Spectrometer_Option_2.CATDrawing	Blatt Bl.
Ers. für:							

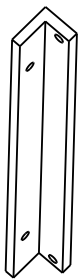
Front view
Scale: 1:1



Left view
Scale: 1:1



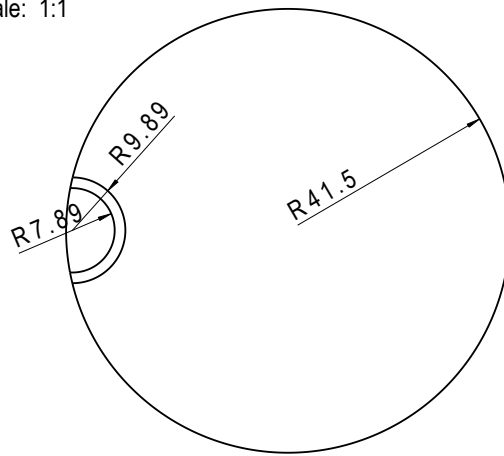
Top view



Isometric view
Scale: 1:1

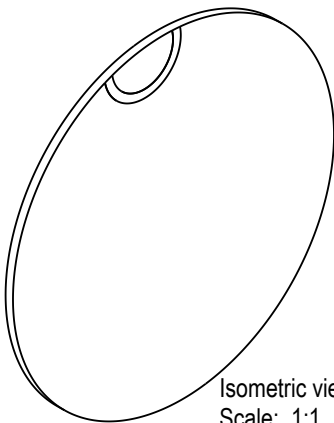
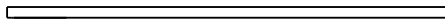
		Scale: 1:1 +0.1 -0.4 DIN 6784	1:1 Allgemeintoleranz nach ISO 2768-mK	Format A4	Maßstab 1:1 Masse xx kg
Aluminium					<h1>ModularL4</h1>
			Datum	Name	
			Bearb.	11.10.2018 Francisco Mansilla	
			Gepr.		
			Berech.		
Zust.	Änderung	Datum	Name	Norm	
Betreuer: Jona Petri Heiko Stack Tel.(Betreuer): ZZ-ZZ Tel.(Zeichner): ZZ-ZZ		Institut für Raumfahrtssysteme			Zeichnungsnummer: XXX-ZZ-MMSSS-BBB-DD-RR Zeichnungsdatei: Spectrometer_Option_2.CATDrawing
Ers. für:					Blatt Bl.

Front view
Scale: 1:1



Left view
Scale: 1:1

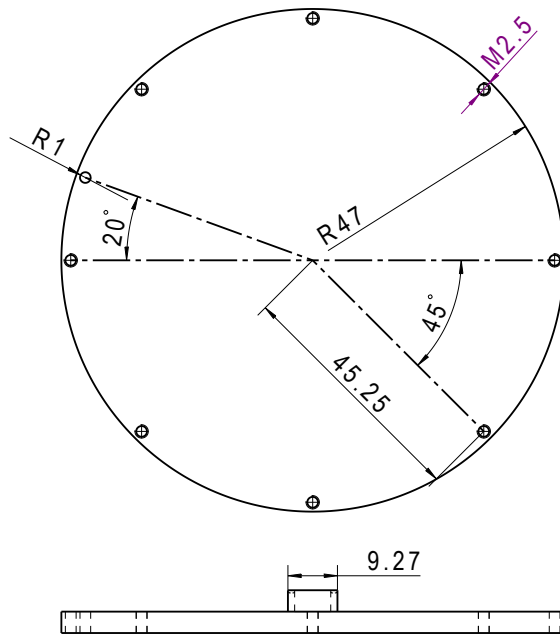
Top view
Scale: 1:1



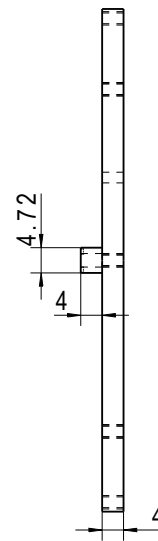
Isometric view
Scale: 1:1

		 DIN 6784	Allgmeintoleranz nach ISO 2768-mK	Format A4	Maßstab 1:1	Masse xx kg
			Datum 11.10.2018	Name Francisco Mansilla	<h1>Piezo Sensor</h1>	
			Bearb.	Gepr.		
			Berechn.	Norm		
Zust.	Änderung	Datum	Name	Norm		
Betreuer: Tel.(Betreuer): Tel.(Zeichner):		Jona Petri Heiko Stack ZZ-ZZ ZZ-ZZ		Institut für Raumfahrtssysteme	Zeichnungsnummer: XXX-ZZ-MMSSS-BBB-DD-RR Zeichnungsdatei: Spectrometer_Option_2.CATDrawing	Blatt Bl.
Ers. für:						

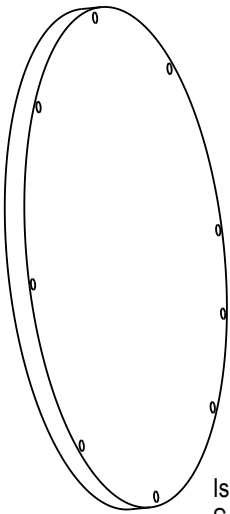
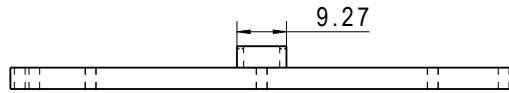
Front view
Scale: 1:1



Left view
Scale: 1:1



Top view
Scale: 1:1



Isometric view
Scale: 1:1

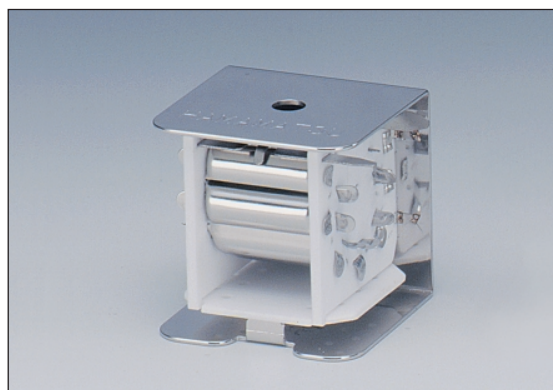
		$\begin{matrix} +0.3 & -0.2 \\ +0.1 & -0.4 \end{matrix}$ DIN 6784	Allgemeintoleranz nach ISO 2768-mK	Format A4	Maßstab 1:1 Aluminium	Masse xx kg
			Datum 11.10.2018	Name Francisco Mansilla	<h1>Target</h1>	
			Bearb. Gepr.	Berechn.		
			Zust.	Änderung		
			Datum	Name		
Betreuer: Jona Petri Heiko Stack Tel.(Betreuer): ZZ-ZZ Tel.(Zeichner): ZZ-ZZ		Institut für Raumfahrtssysteme			Zeichnungsnummer: XXX-ZZ-MMSSS-BBB-DD-RR Zeichnungsdatei: Spectrometer_Option_2.CATDrawing	Blatt Bl.
Ers. für:						

APPENDIX B. R8811 Ion Detector

For Compact Mass Spectrometers

OVERVIEW

Quadrupole mass spectrometers used for residual gas analyzers have been downsized to solve problems of limited installation space. A trend of the downsizing would be an ever-greater degree in the future. However, it cannot be achieved just by reducing the ion source and Quadrupole electrode sizes. Small ion detector is also required essentially. To meet the requirement, Hamamatsu has developed a compact ion detector. The unique ion detector breaks the performance barriers on conventional electron multipliers and will prove the ideal result for your needs.



SPECIFICATIONS

GENERAL

Parameter	Description / Value	Unit
Input Aperture Diameter	φ3	mm
Dynode Structure	Circular cage	—
Number of Dynode Stages	13	—
First Dynode Material	Al ₂ O ₃	—
Total Built-in Resistance	13	MΩ
Operating Ambient Temperature	-30 to +50	°C
Storage Temperature	-80 to +50	°C
Polarity of Detected Ions	Positive	—

MAXIMUM RATINGS

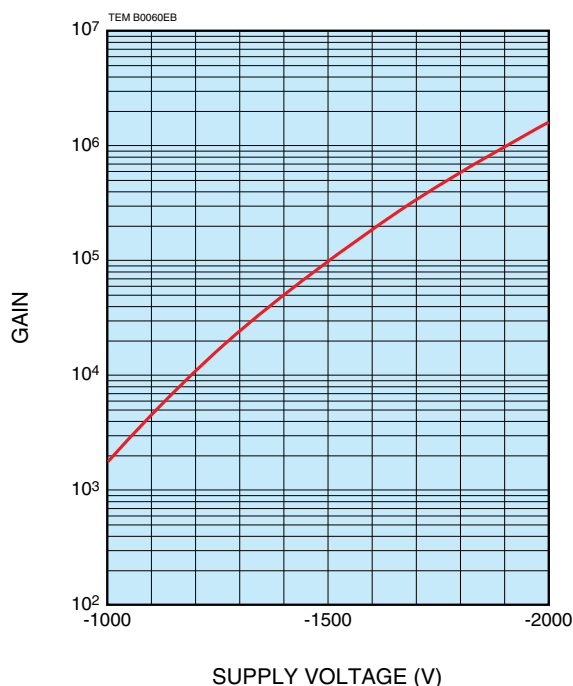
Parameter	Value	Unit
Anode to First Dynode Voltage	-2000	V
Anode to Last Dynode Voltage	200	V
Faraday Cup Voltage	200	V
Operating Vacuum Level	1 × 10 ⁻²	Pa
Bake-Out Temperature (at 5 × 10 ⁻³ Pa)	350	°C
Average Anode Current ^(A)	10	μA
Operating Gain	1 × 10 ⁷	—

CHARACTERISTICS

Parameter	Value	Unit
Recommended Supply Voltage	-1500	V
Gain (Typ.)	1 × 10 ⁵	—
DC Linearity (Typ.)	5	μA
Dark Current (Max.)	1	pA
Rise Time (Typ.)	1.6	ns
Anode to All Other Electrode Capacitance	0.75	pF

NOTE: (A) Averaged over any interval of 30 seconds maximum.

Figure 1: Typical Gain

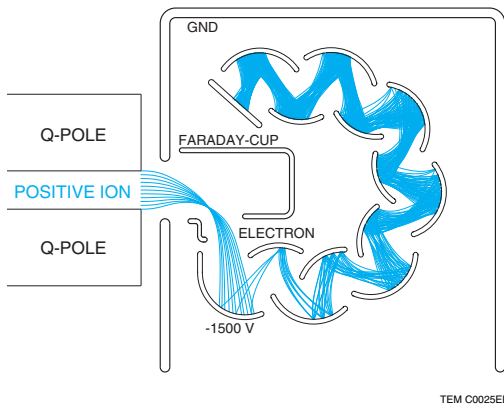


Subject to local technical requirements and regulations, availability of products included in this promotional material may vary. Please consult with our sales office. Information furnished by HAMAMATSU is believed to be reliable. However, no responsibility is assumed for possible inaccuracies or omissions. Specifications are subject to change without notice. No patent rights are granted to any of the circuits described herein. ©2014 Hamamatsu Photonics K.K.

ELECTRON MULTIPLIER R8811

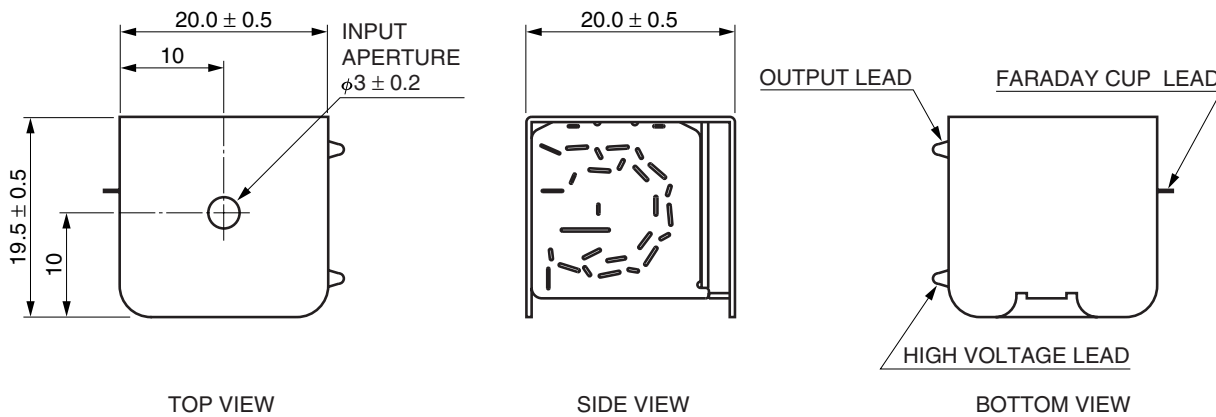
STRUCTURE

This electron multiplier has an off-axis structure and a Faraday cup needed for ion detection in Quadrupole mass spectrometers which are capable of making precise measurements over a wide dynamic range with a high S/N. The structure also incorporates a voltage divider, which is essential for discrete type electron multipliers. By simply wiring the high voltage, the signal and the Faraday cup, reliable operation can be achieved without adding any other parts.



Ions emitted from Quadrupole are multiplied while being deflected and focused by the electron lens created by the combination of the Faraday cup, the ion deflection electrodes and the electron multiplier electrodes. The layout of the Faraday cup, the ion deflection electrodes and the electron multiplier electrodes are designed by special 3D simulation of ion and electron trajectories. This layout allows detecting the input ions with high efficiency.

DIMENSIONAL OUTLINE (Unit: mm)



HAMAMATSU PHOTONICS K.K. www.hamamatsu.com

HAMAMATSU PHOTONICS K.K., Electron Tube Division

314-5, Shimokanzo, Iwata City, Shizuoka Pref., 438-0193, Japan, Telephone: (81)539/62-5248, Fax: (81)539/62-2205

U.S.A.: Hamamatsu Corporation: 360 Foothill Road, Bridgewater, N.J. 08807-0910, U.S.A., Telephone: (1)908-231-0960, Fax: (1)908-231-1218 E-mail: usa@hamamatsu.com

Germany: Hamamatsu Photonics Deutschland GmbH: Arzbergerstr. 10, D-82211 Herrsching am Ammersee, Germany, Telephone: (49)8152-375-0, Fax: (49)8152-2658 E-mail: info@hamamatsu.de

France: Hamamatsu Photonics France S.A.R.L.: 19, Rue du Saule Trapu, Parc du Moulin de Massy, 91882 Massy Cedex, France, Telephone: (33)1 69 53 71 00, Fax: (33)1 69 53 71 10 E-mail: infos@hamamatsu.fr

United Kingdom: Hamamatsu Photonics UK Limited: 2 Howard Court, 10 Tewin Road, Welwyn Garden City, Hertfordshire AL7 1BW, United Kingdom, Telephone: (44)1707-294888, Fax: (44)1707-325777 E-mail: info@hamamatsu.co.uk

North Europe: Hamamatsu Photonics Norden AB: Torshamnsgatan 35 SE-164 40 Kista, Sweden, Telephone: (46)8-509-031-00, Fax: (46)8-509-031-01 E-mail: info@hamamatsu.se

Italy: Hamamatsu Photonics Italia S.r.l.: Strada della Moia, 1 int. 6, 20020 Arese (Milano), Italy, Telephone: (39)02-93581733, Fax: (39)02-93581741 E-mail: info@hamamatsu.it

China: Hamamatsu Photonics (China) Co., Ltd.: B1201 Jiaming Center, No.27 Dongsanhuan Bellu, Chaoyang District, Beijing 100020, China, Telephone: (86)10-6586-6006, Fax: (86)10-6586-2866 E-mail: hpc@hamamatsu.com.cn

TPMH1340E02
AUG. 2014 IP

APPENDIX C. PZT from PI

Ceramics

PI TECHNOLOGY CATALOGUE PZT

			Soft PZT materials					Hard PZT materials					Lead-free materials	
		Unit	PIC151	PIC255/ PIC252 ¹⁾	PIC155	PIC153	PIC152	PIC181	PIC184 ²⁾	PIC144 ²⁾	PIC241	PIC300	PIC110	PIC700 ³⁾
Physical and dielectric properties														
Density	ρ	g/cm ³	7.80	7.80	7.80	7.60	7.70	7.80	7.75	7.95	7.80	7.80	5.50	5.6
Curie temperature	T_c	°C	250	350	345	185	340	330	295	320	270	370	150	200 ³⁾
Relative permittivity	in the polarization direction ⊥ to polarity	$\epsilon_{33}^T/\epsilon_0$	2400	1750	1450	4200	1350	1200	1015	1250	1650	1050	950	700
		$\epsilon_{11}^T/\epsilon_0$	1980	1650	1400			1500	1250	1500	1550	950		
Dielectric loss factor	$\tan \delta$	10 ⁻³	20	20	20	30	15	3	5	4	5	3	15	30
Electromechanical properties														
Coupling factor	k_p		0.62	0.62	0.62	0.62	0.48	0.56	0.55	0.60	0.50	0.48	0.30	0.15
	k_t		0.53	0.47	0.48			0.46	0.44	0.48	0.46	0.43	0.42	0.40
	k_{31}		0.38	0.35	0.35			0.32	0.30	0.30	0.32	0.25	0.18	
	k_{32}		0.69	0.69	0.69		0.58	0.66	0.62	0.66	0.64	0.46		
	k_{15}			0.66				0.63	0.65		0.63	0.32		
Piezoelectric charge coefficient	d_{31}		-210	-180	-165			-120	-100	-110	-130	-80	-50	
	d_{32}	10 ⁻¹² C/N	500	400	360	600	300	265	219	265	290	155	120	120
	d_{15}			550				475	418		265	155		
Piezoelectric voltage coefficient	g_{31}		-11.5	-11.3	-12.9			-11.2	-11.1	-10.1	-9.8	-9.5		
	g_{32}	10 ⁻³ Vm/N	22	25	27	16	25	25	24.4	25	21	16	-11.9	
Acousto-mechanical properties														
Frequency coefficients	N_p		1950	2000	1960	1960	2250	2270	2195	2180	2190	2350	3150	
	N_t		1500	1420	1500				1640	1590	1590	1700	2300	
	N_s	Hz·m	1750		1780				2010	1930		1550	1700	2500
	N_f		1950	2000	1990	1960	1920	2110	2035	2020	2140	2100		
Elastic compliance coefficient	S_{11}^E	10 ⁻¹² m ² /N	15.0	16.1	15.6			11.8	12.7	12.4	12.6	11.1		
	S_{22}^E		19.0	20.7	19.7			14.2	14.0	15.5	14.3	11.8		
Elastic stiffness coefficient	C_{33}^D	10 ¹⁰ N/m ²	10.0		11.1			16.6	14.8	15.2	13.8	16.4		
Mechanical quality factor	Q_m		100	80	80	50	100	2000	400	1000	400	1400	250	
Temperature stability														
Temperature coefficient of ϵ_{33}^T (in the range -20 °C to +125 °C)	$TK \epsilon_{33}$	10 ⁻² /K	6	4	6	5	2	3	5			2		
Time stability (relative change of the parameter per decade of time in %)														
Relative permittivity	C_ϵ			-1.0	-2.0				-4.0				-5.0	
Coupling factor	C_K			-1.0	-2.0				-2.0				-8.0	